NOVEL APPLICATIONS OF NANOTECHNOLOGY IN MEDICINE AND GREEN ENERGY

A Thesis
Presented to
The Academic Faculty

by

Steven C. Hayden

In Partial Fulfillment
of the Requirements for the Degree
Doctor of Philosophy in the
School of Chemistry and Biochemistry

Georgia Institute of Technology
May 2013

NOVEL APPLICATIONS OF NANOTECHNOLOGY IN MEDICINE AND GREEN ENERGY

Approved by:

Professor Uwe H. F. Bunz,
Committee Chair
School of Chemistry and Biochemistry
Georgia Institute of Technology

Professor Ingeborg Schmidt-Krey
School of Biology
Georgia Institute of Technology

Professor Mostafa A. El-Sayed,
Advisor
School of Chemistry and Biochemistry
Georgia Institute of Technology

Professor Laren Tolbert
School of Chemistry and Biochemistry
Georgia Institute of Technology

Professor Christine K. Payne
School of Chemistry and Biochemistry
Georgia Institute of Technology

Date Approved: 11 December 2012

To my parents,

Rick and Lisa Hayden,

whose support has been relentless.

ACKNOWLEDGEMENTS

The work represented in this thesis has involved a staggering number of collaborators, mentors, and supportors. First, I must thank Drs. Mostafa El-Sayed and Uwe Bunz for support, guidance, and funding during my five years at Georgia Tech. I would also like to thank my committee members Drs. Ingeborg Schmidt-Krey, Christine Payne, and Laren Tolbert for their help guiding me through this work and helping me to grow as a scientist. I have had the honor to collaborate with many other scientists around the globe, all of whom have contributed to my body of knowledge and to this thesis. Thank you to Dr. Ingeborg Schmidt-Krey, Dr. Vincent Rotello, Dr. Nageh Allam, Dr. Chun-Wan Yen, Dr. Ronnie Phillips, Dr. Genxiang Zhao, Dr. Ron Hunter, Dr. Oscar Miranda, Dr. Paul Szymanski, Dr. Anne Riederer, Dr. P. Barry Ryan, Dr. Erik Dreaden, Dr. Dana Barr, Dr. Anna Eremenko, Rachel Near, Meg Mackey, Lauren Austin, and Krishnendu Saha.

The two groups I have had the honor of working with consist of some of the finest people I have known. In particular, Chun-Wan Yen and Ronnie Phillips have been the best self-appointed mentors that anyone could ever hope to have. Brian Snyder and Adam Poncheri were anchors when I would have floated off into scientific obscurity. Paul Szymanski has been an integral part of everything successful that I have completed since his arrival at Tech, and he has taught me much. Rachel Near has been invaluable on many levels - colleague, friend, resolver. She has been intrinsic to the construction of this thesis. There is a long list of people at Georgia Tech who have contributed to this thesis in some way. Thank you to Meg Mackey, Justin Bordley, Evan Davey, Michael Rood, Raquel Lieberman, Justin Bordley, Evan Davey, Nichole Marotta, Anthony Appleton, Daniel O'Niel, Nic Haase, Erik Dreaden,

Li Chu, Christopher Boyle, Christopher Tabor, Bahareh Azizi, and Michael Johnson.

My minions, Nicholas Pasquariello, Vanessa Nguyen, Daniel Thackston, CJ Daly, and Ewelina Prockow are each gems in their own special way. Thank you for helping me learn to manage people and projects, and thank you for always pretending to be as excited about science as I am.

Many children boast that they have superior parents and family; mine eclipse theirs. Rick C. and Lisa C. Hayden are untouchable as life-guides, shields, and friends. Thank you for always helping me to get back up, and thank you for being ever-supportive of my non-traditional career path. To my brothers, Alex C., Curt C., and Zach C., thank you for always rising halfway out of your proverbial chair at the slightest hint of a threat to me. We will always protect each other as a unit. My grandmother, Charlotte Crawford Cowart, taught me to read and write and love doing so at an impossibly early age; neither this thesis nor the degrees that predecessed it would exist without her. My grandfather, Kenneth Crawford, is finally getting his requested primate.

A healthy personal life is an intrinsic part of career success. I have encountered some incredibly special people who have each helped build the person I am today. Dr. Anna Weaver showed me how large the world is. Dr. Dale Moore helped me find a unique path to walk. Dr. Mary Anne Drake and Sue Roberts helped me find peace. Thank you to Joey Schultz for being an incredible asset scientifically, for helping me handle crises, and for talking science with me even in public. Thank you to Melissa McDonald and Clay Crutchfield; they are the primary reasons I survived my first two years in graduate school. There are several others who would be listed as friends and thanked for their support roles, but who, together, form an extensive second family for me. We have been scattered to the winds, but a family we remain. Thank you Jerome Evans, Sean Britts, Nathan Hendricks, Troy Wood, Alice Tang, Ron Hunter, Colin Gillens, Fred Smith, Ronnie Phillips, Cecil McKraken, Ronnie

Jefferson, Brian Snyder, Danny Tate Phillips, Jason Triplett, James Matthew Bass, Ryan Vauhn, Kevin Hayes, Joey Schultz, Will Ramseur, Naomi Latini, Carl Latini, Lauren McSwain, Zach Broome, Chris Whittemore, Kristin Levesque, Derritt Mason, Eddy Acthergal, and Jean-Baptiste Leduq. Also, thank you to the Friday Face crew, Dacia Morgan, Meg Ryan, Shawni Reynolds, Tina Newman, Ryan Scheuller, and Michael Jenkins for keeping me going, and to Amanda Foess, David Hemple, and Archana and Roland Gagnier.

TABLE OF CONTENTS

LIST OF TABLES

LIST OF FIGURES

Table 1: List of Symbols and Abbreviations.

Abbreviation	Meaning
AgNC	Silver Nanocube
AgNPr	Silver Nanoprism
AgNR	Silver Nanorod
AgNS	Silver Nanosphere
AuNF	Gold Nanoframe
AuNR	Gold Nanorod
AuNS	Gold Nanosphere
bR	bacteriorhodopsin
CBD	chemical bath deposition
DDT	dodecanethiol
HOMO	Highest Occupied Molecular Orbital
ITO	Indium Tin Oxide
LSPR	Localized Surface Plasmon
LUMO	Lowest Unoccupied Molecular Orbital
MW	Molecular Weight
NIR	Near Infrared
NP(s)	Nanoparticle(s)
NT(s)	Nanotube(s)
PM	Purple Membrane
PS	Photosensitizer
PVP	Polyvinylpyrrolidone
QD(s)	Quantum Dot(s)
SEM	Scanning Electron Microscopy
SPR	Surface Plasmon Resonance
TEM	Transmission Electron Microscopy
TOPO	Trioctyl phosphine Oxide
UV-Vis	Ultraviolet-Visible
WT	Wild Type

SUMMARY

The development of techniques for colloidal nanoparticle synthesis has allowed scientists to fabricate materials that can manipulate light on a scale that is small even compared to the wavelength of the light itself. This ability has led to the development of myriad and diverse applications of nanostructures in wide-ranging fields. This thesis focuses on the investigation and exploitation of nanoscale material properties in the fields of medicine and energy.

The unique optical properties of nanoparticles arise from their size and their high surface area to volume ratios compared to bulk materials. As a result of this relationship, the surface characteristics of nanoparticles generally dominate their properties, whereas in bulk materials the surface atoms have very little bearing on the properties of the composite. **Chapter 1** gives an introduction to nanoparticles and their optical properties, including a discussion of the plasmon resonance and the properties imbued upon nanoparticles possesing such a resonance as well as the applicability of these properties that will be explored in the subsequent chapters.

Chapter 2 presents a study of the interaction of cationic, hydrophobic gold nanoparticles as probes to elucidate specific regions of interest on cell surfaces. The high imaging contrast of gold nanoparticles in electron microscopy allows for visual, macroscopic observation of the aggregation patterns formed by these nanoparticles on cell surfaces. Plasmon resonant coupling between proximal nanoparticles is exploited in order to monitor nanoprobe binding and localization over time with the use of extinction spectroscopy. The role of surface proteins in the nanoparticle-cell surface interaction is elucidated, generating composite data with relevance in pharmaceutical

development and pharmacokinetics. Additionally, bacteria strain-dependent toxicity is observed and subsequently investigated for smaller gold nanoparticle probes, demonstrating a potential use for nanoparticles as strain-specific antibiotics.

The development of affordable, effective antibiotic technology is one of the major scientific challenges of our time; infections from pathogen-infested drinking water alone account for millions of deaths each year worldwide. In **Chapter 3**, we investigate the use of titanium dioxide as an inexpensive method to harness solar energy to split water into reactive species and thereby decontamitate solutions of *E. coli*. Though titanium dioxide is an excellent catalyst for water splitting, it requires UV irradiation, which is fairly lacking in the solar emission spectrum. Further, recuperation of titanium dioxide nanoparticles from solution is non-trivial, and its immobilization into a film greatly limits its surface area and charge carrier efficiency, thereby limiting its activity. We treat both the poor visible light absorption capability as well as the surface area limitation in this study. CdS semiconductor nanocrystals are used to extend the absorption edge of TiO_2 further into the visible light region of the spectrum by providing for lower-energy photon absorption and charge injection into titanium dioxide. TiO_2 is also electrochemically anodized to generate TiO_2 nanotube arrays, which have greatly increased surface area as well as more efficient charge transfer properties compared to thin films of TiO_2 nanoparticles.

The utility of nanoparticles in increasing the light absorption of other systems continues as a theme in the work presented in the next two chapters. **Chapter 4** examines the plasmonic enhancement of the solar energy conversion in a biomimetic system. In this endeavor, we enhance the photocurrent generated by a light-transducing, proton-pumping protein, bacteriorhodopsin, in a 3-dimensional wet electrochemical cell. First, we increase the overall charge carrier separation with the use of a proton-selective membrane in order to minimize ionic depolarization in the cell. We then use

plasmonic nanoparticles to exploit an irregularity in the bacteriorhodopsin photocycle known as the blue light effect. This effect shortens the timescale of the photocyle by more than 99% via blue photon absorption, but it has a very low natural occurance. Plasmonic nanoparticles tuned to the blue wavelength region increase the flux of blue photons on a local level and thereby increase the overall photocurrent generation. We first examine the importance of nanoparticle field strength to photocurrent enhancement using silver nanospheres with different capping shell thicknesses. We then consider the trade-off between (1) using a nanoparticle with a plasmon resonance tuned perfectly to the blue wavelength region and (2) using a nanoparticle with a stronger field intensity but weaker energetic presence in the blue. By minimizing ionic depolarization, minimizing shielding of the plasmon electromagnetic field, and maximizing the field strength while maintaining the plasmon frequency at the proper wavelength, we demonstrate an enhancement of 5,000-fold in the photocurrent production by bacteriorhodopsin.

Chapter 5 explores a variation on the theme of **Chapter 4** with an application in cancer therapeutics. Here, a photodynamic cancer drug, protoporphyrin IX (PpIX), is incorporated into complexes with silver nanospheres, gold nanospheres, and gold nanorods. Each of these nanoparticles displays a plasmon resonance in a different region of the spectrum, with consequent different overlap with the absorption or emission of the drug. Photodynamic therapeutic potential is measured *in situ* and *in vivo*, and the drug activity is shown to be strongest when drug absorption overlaps with plasmon resonance. Absorption by electronic excitations in the particle crystal lattice is shown to function as a competitive light filter and decrease drug activity. Additionally, the method of attachment of the drug to the nanoparticle is examined. Maximum enhancement of drug activity is shown to require the drug to remain bound close to the nanoparticle surface, where the electromagnetic field strength is highest. This plasmonic enhancement effect on drug activity is shown to outstrip the increase

in drug activity seen when using the nanoparticle solely as a delivery platform.

In **Chapter 6**, some synthetic techniques are presented for various nanomaterials. Included are syntheses for gold, silver, and semiconductor nanoparticles of a variety of shapes and sizes as well as for TiO_2 nanotube arrays. The relationship of the ratio of capping agent to metal salt is explored for gold nanospheres, and a method for facile tuning of the longitudinal plasmon resonance displayed by gold nanorods is presented. Synthetic techniques are also presented for the nanoparticles whose applications are explored in the preceding chapters.

CHAPTER I

INTRODUCTION TO NANOMATERIALS

Nanomaterials have been used by man for centuries; nanoparticles (NPs) are responsible for the unique ways that objects such as the Lycurgus cup and cathedral stained glass windows interact with light (Figure 1).[8] However, nanoparticles have been thrust into the limelight in the past two decades, as scientists have gained both better control over their syntheses [5, 48, 68] as well as the ability to thoroughly characterize them, [13, 36] allowing access to their myriad applications. [9]

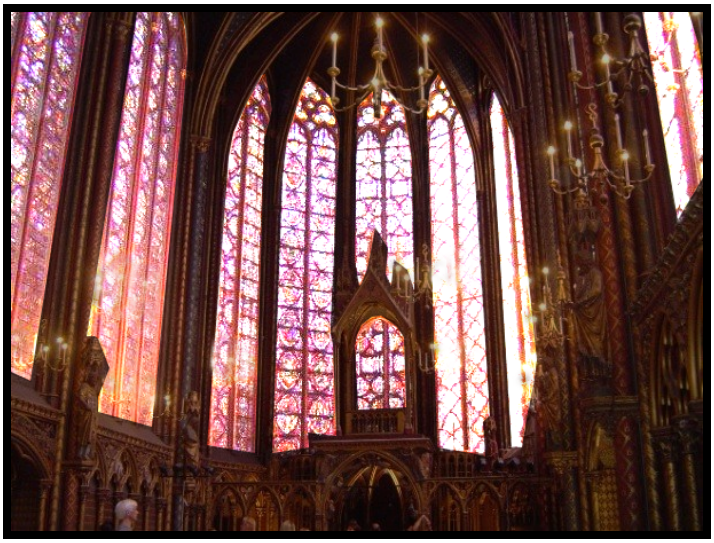

Figure 1: Stained glass window in the Sainte-Chapelle in Paris. Unlike organic dyes, which are suceptible to photobleaching, the gold nanoparticles in these glass windows have retained their vibrant colors for centuries. Photo by SCH.

1.1 Materials on the Nanoscale

When materials are reduced to the nanometer size scale (2-100 nm), new properties develop that differ greatly from the properties of the same material in bulk as well as the properties of the individual constituent atoms. [12] These nanoscale properties

derive fom the differences in electronic motion in the nanoparticle relative to the bulk material. [11]

An example is found in CdSe quantum dots (emmissive semiconductor nanoparticles). When this semiconductor material is reduced to the nanometer size scale, confinement effects increase the energy level spacing as the electronic motion is confined to a smaller volume. [39] As a result, the emission of these particles can be tuned throughout virtually the entire visual spectrum by changing their diameter (Figure 2). [33] The systhesis of these quantum dots is discussed in Appendix 6, and their use for solar energy applications is presented in Chapter 3.

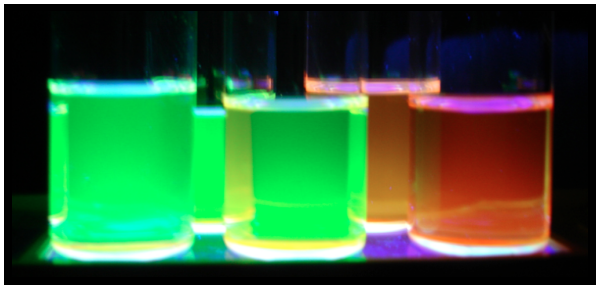

Figure 2: Photograph showing the emission of CdSe quantum dots of increasing diameter (left to right) under UV excitation. The wavelength of emission depends on the size of the nanoparticle due to quantum confinement effects. Synthetic procedures discussed in Chapter 6.Photo by SCH.

Because of the much larger surface area to volume ratio in nanoscale materials, the atoms on the surface of nanoparticles have a pronounced effect on their properties. Thus, the particle characteristics are largely derived from the size and structure of the particle, with the composition and medium dielectric also having an influence. [12] This high surface area to volume ratio makes metal nanoparticles highly useful as catalysts. [53] For plasmonic nanoparticles, in particular gold and silver, the new properties incurred upon the material as a result of its size make nanoparticles of these precious metals particularly interesting for optical applications. [27]

1.2 Precious Metals on the Nanoscale

The brilliant colors of cathedral stained glass windows was attributed to the presence of colloidal gold nanoparticles by Faraday in the 1850's. [69] Later, it was shown that their peculiar properties arise from the way in which incident light interacts with their conduction band electrons, as illustrated in Figure 3 and discussed forthwith.

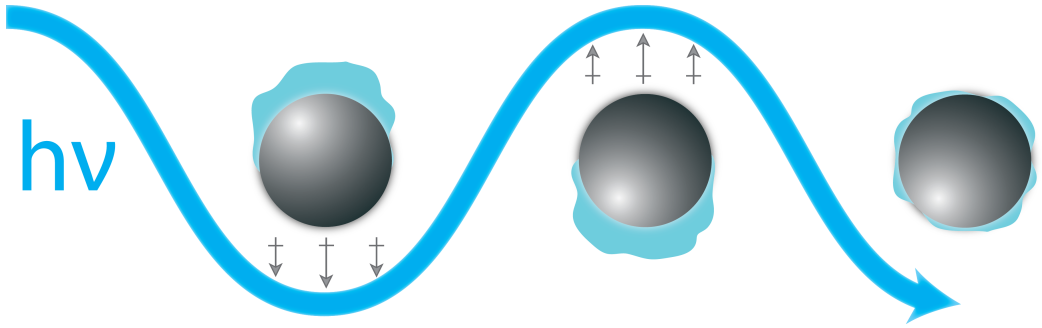

Figure 3: Schematic representation of the interaction between incident electromagnetic radiation of the proper wavelength and the conduction band electrons in a nanoparticle. The electrons respond to the polarization in the lightwave, which leads to a flux in the electron density. This flux is called a plasmon, and its effect is seen most strongly at the surface of the particle.

1.2.1 The Plasmon Resonance

Nanoparticles (2 - 100 nm) are roughly an order of magnitude smaller than the wavelengths of visible light (ca. 350 - 800 nm). Since electromagnetic radiation travels as a polarized wave much larger than the nanoparticles, [2] the inherently-fluid conduction band electrons in certain metal nanoparticles respond to the polarization of the incident lightwaves. [47] Thus, the exposure of precious metal nanoparticles to resonant photons results in a collective oscillation of the conduction band electrons in the nanoparticles, which in turn induces an electromagnetic field. Electrons on the surface of the nanoparticles move more freely than those in the interior, and their coherent oscillations across the nanoparticle from one surface to the other - along the exciting light polarization vector - are subject to the pendulum effect. This effect results in the induced fields spending more time at the turning points of the oscillation

(i.e. at the surface). Thus, this event is termed a localized surface plasmon resonance (LSPR).

For particles much smaller than the wavelength of light, it is valid to assume that the absorption derives entirely from the dipole mode [34] and to assume that the electric field of light is constant. [31] At this dipolar and quasi-static limit, the polarizability of a spherical particle is given by Equation 1:

$$\alpha = 3\epsilon_0 V \frac{\epsilon - \epsilon_m}{\epsilon + 2\epsilon_m} \tag{1}$$

where ϵ_0 is the permittivity of vacuum, V is the particle volume, ϵ_m is the dielectric constant of the surrounding medium, which is real for almost all typical media, and ϵ is the dielectric function of the metal, which is complex and given by Equation 2 as a function of the angular frequency of light (ω). [38]

$$\epsilon(\omega) = \epsilon_{real}(\omega) + i\epsilon_i(\omega) \tag{2}$$

The real portion of the dielectric $\epsilon_{real}(\omega)$ is related to the particle's stored energy in the medium, while the imaginary part $\epsilon_i(\omega)$ is related to the dissipation of energy within the particle. [55]

When the imaginary portion of the metal dielectric function is sufficiently small and the real component is negative, the denominator in Equation 1 approaches zero, and the polarizability approaches its maximum. This maximum occurs when

$$\epsilon_{real} = -2\epsilon_m \tag{3}$$

In this case, the polarizability approachs infinity and a plasmon resonance can be supported on the particle at the appropriate irradiation frequency. [31] Most elements lack sufficiently real dielectric functions to support a plasmon resonance, with the exception of noble metals and some alkali metals. [31] Of these, only noble metals (copper, silver, and gold) have a plasmon resonance in the visible, [42] rendering these materials particularly interesting for optical applications, though copper is rarely used due to its high susceptibility to surface oxidation.

1.2.2 Energy of the Plasmon Resonance

The energetic differences between silver and gold nanoparticles are easily contrasted by considering the full width at half max of the plasmon band. The plasmon bandwidth at half-maximum is given by Equation 4, [38]

$$\Delta\omega_{1/2} \approx \frac{2\epsilon_i}{\frac{\delta\epsilon_r}{\delta\omega}} \mid_{sp} \tag{4}$$

at the light frequency (ω_{sp}) that satisfies Equation 3, thereby generating the surface plasmon maximum condition. This relationship indicates a narrower bandwidth when the imaginary portion of the dielectric is small and when the slope of ϵ_{real} with respect to ω is high.

Silver and gold have very similar $\delta\epsilon_{real}$ and $\delta\omega_{sp}$ values; however, the imaginary component of the dielectric function for silver is much smaller than for gold. Thus, silver has a much more narrow plasmon bandwidth, a much higher scattering-to-absorption ratio, [38] and a much stronger plasmon field compared to gold nanoparticles of the same size. [58] These properties lead to increased utility of one or the other metal depending on the application. For example, silver nanoparticles are highly useful in Surface Enhanced Raman Spectroscopy (SERS), where the scattering cross section determines the signal strength. [22] Gold nanoparticles find utility in plasmonic photothermal cancer therapy (PPTT), in which the lower scattering to absorption ratio are needed to generate localized heat and the relative stability of gold makes it less toxic and more biocompatible. [24]

1.2.3 The Plasmon-Induced Electromagnetic Field

The plasmon oscillation is considered to be a photon that has been confined to the nanoscale size of the particle. [29] Though the diffraction limit does not conventially allow the the confinement of light to a size smaller than its wavelength, the plasmon resonance does provide for confinement of the electromagnetic field to a size scale that is orders of magnitude smaller than the wavelength of the original photon. [4]

As a result, the field generated by the plasmon at the surface of the particle is quite strong and can lead to great enhancement of radiative processes in adjacent electronic systems. [30] Thus, plasmonic nanoparticles have found great utility in applications such as the trace detection of explosives via Raman spectroscopy, [7, 46] the enhancement of photocurrent in biomimetic and dye-sensitized solar cells, [71, 6, 10] and the enhancement of activity in photodynamic cancer drugs [32].

The strength of the field decays exponentially with increasing distance from the nanoparticle surface, [14] as seen in Figure 4. Additionally, the strength of the field is greatly dependent on the shape of the nanoparticle. [19] Figure 4 shows the plot of the field strength for a 40 nm edge length silver cube (left) and a 40 nm diameter silver sphere (right), each on its own scale. The field is significantly more localized and stronger in regions of higher-order geometries, such as corners and edges. This is known as the lightning rod effect, and it results from the relatively high surface area-to-volume ratio in these regions. [18, 3]

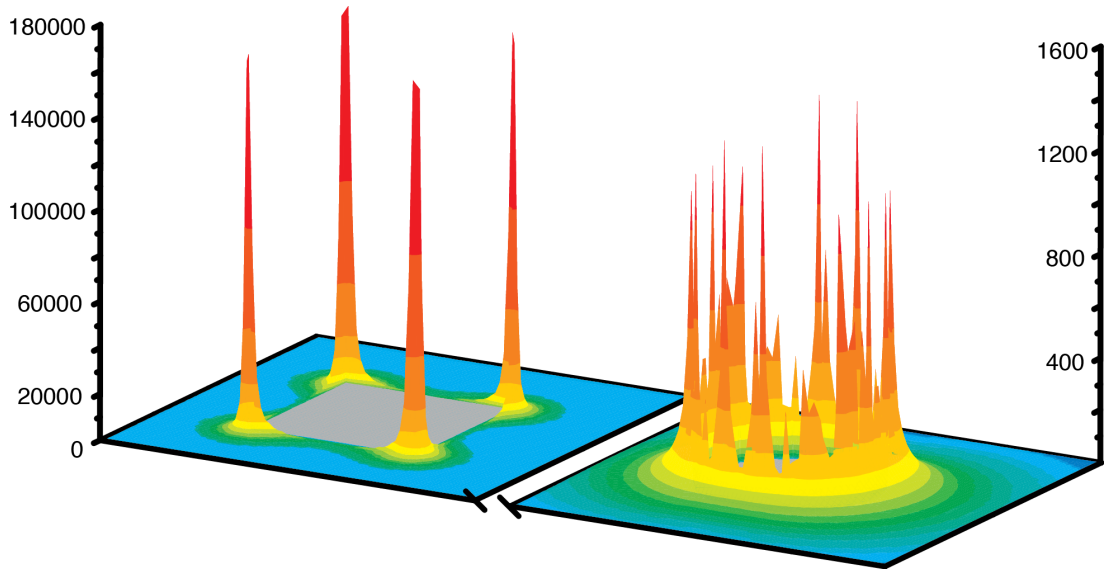

Figure 4: Three dimensional electromagnetic field plot for a 40 nm edge length silver cube (left) and a 40 nm diameter silver sphere (right), each on its own intensity scale. The field is significantly stronger and more localized in regions of more complex geometry, such as corners and edges. This is known as the lightning rod effect, and it results from the relatively high surface-area-to-volume ratio in these regions.

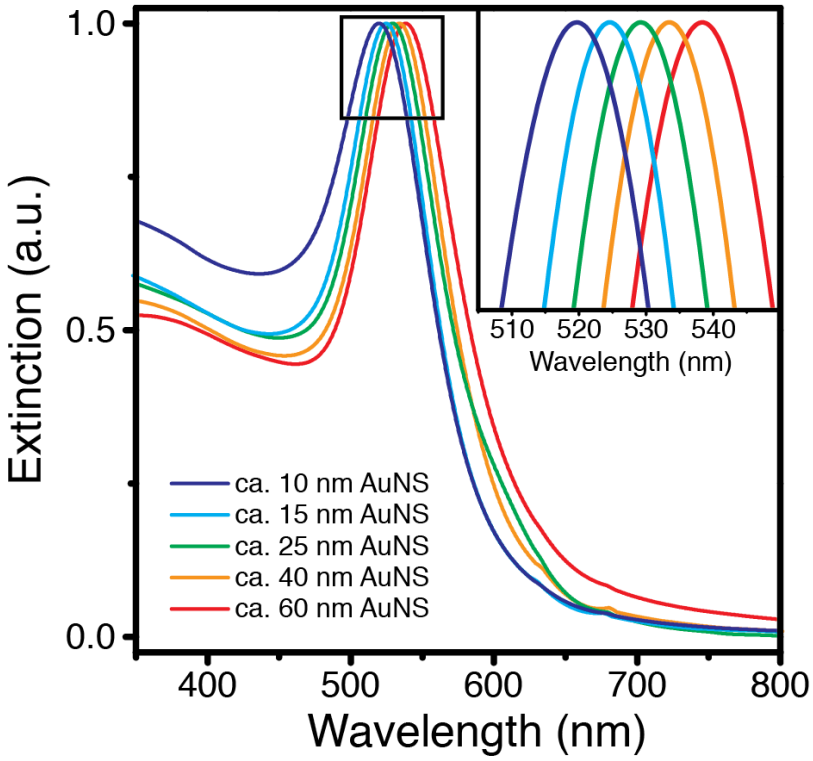

Figure 5: Extinction profile of gold nanospheres of increasing diameter. Zoom view emphasizes bathochromic shift with increasing nanoparticle size.

Increasing nanoparticle size results in the concurrent increase in depolarization of the electric field of light due to the finite ratio of particle size to wavelength. [41] This is termed electromagnetic retardation, and it results in both a red-shift and a broadening of the plasmon extinction band. This bathochromic shift with increasing size is seen in the example spectra shown in Figure 5. As a result of this shift, plasmonic nanoparticles - in particular gold nanoparticles - show facile tunability throughout a large wavelength region. This holds true for all shapes, though it is somewhat limited in spherical particles [26] and much more pronounced in anisotropic shapes, such as rods. [43]

1.2.4 Components of the Extinction Cross Section

The number of electrons in a nanoparticle increases in direct proportion to the volume of the nanoparticle, and as a result, the extinction cross section of the particle

also increases with volume. [49] The extinction cross section has two components: scattering and absorption.

When plasmonic nanoparticles are irradiated with light that satisfies the surface plasmon resonance condition, the nanoparticle behaves as depicted in Figure 6, where silver nanospheres are irradiated with 400 nm light. In this case, the nanoparticle absorbs and scatters a relatively large component of the radiation, and the ratio of scattered light to absorbed light increases with increasing particle size. [37]

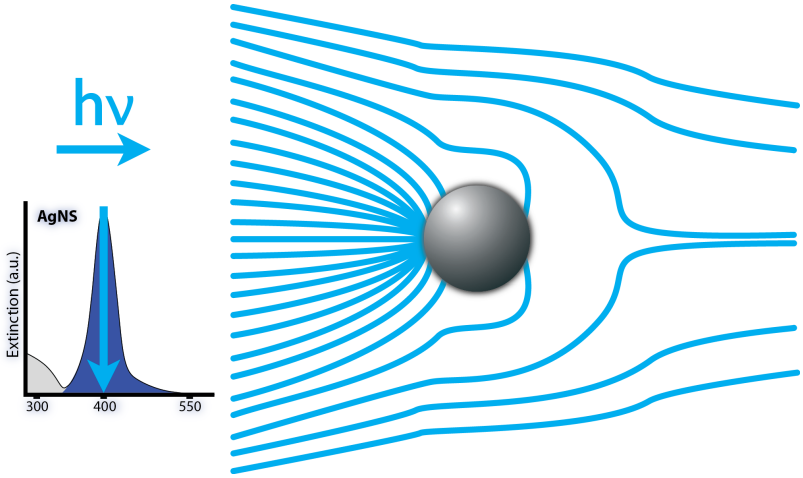

Figure 6: Field lines depicting the nature of interaction between a plasmonic nanoparticle (silver sphere) and incident radiation (400 nm) that is of the same energy as the plasmon resonance (400 nm). Adapted from Hutter et al. [25]

By contrast, if the same nanoparticles are irradiated with light that is not the same wavelength as the resonant frequency of the plasmon, the resultant absence of the plasmon and its field result in an interaction between the particles and the radiation that resembles that of non-plasmonic particles. [25] This is illustrated in Figure 7, where silver nanospheres (plasmon resonance at 400 nm) are irradiated with 550 nm light.

1.2.4.1 Scattering

The scattering cross section becomes significant in particles that are much smaller than the electronic mean free path of the metal (< 100 nm) [40] but large enough that

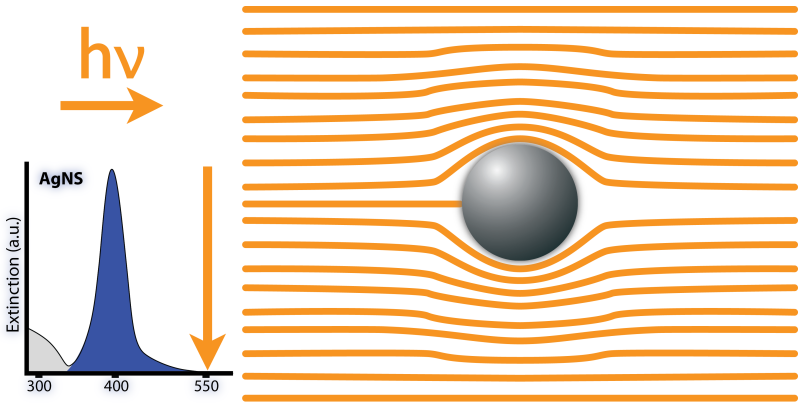

Figure 7: Field lines depicting the nature of interaction between a plasmonic nanoparticle (silver sphere) and incident radiation (550 nm) that is not of the same energy as the plasmon resonance (400nm). Adapted from Hutter et al. [25]

quantum size effects can be ignored (> 3 nm) [1]. As the particle size increases within this 3 to 100 nm range, radiative damping increases. [31] This arises from spontaneous emission of radiation by the electronic oscillations that comprise the plasmon, and it leads to an increased contribution from scattering as the particle size increases. Scattering is an elastic phenomenon; [59] thus, nanoparticles can be used as nanoscale lenses to focus light on an incredibly local level. [45] Functionality as a nanoscale lens facilitates the use of nanoparticles in applications where the absorption cross section of the system in question affects its functionality, [52] such as in solar energy (Chapter 4) and photodynamic therapy (Chapter 5). In these, elastic scattering - or focusing - of the light is shown to greatly increase the absorption - and therefore activity - of the system.

1.2.4.2 Absorption

The absorption component of the extinction cross section arises from one of two events: absorption by the plasmon or absorption by the d-orbitals in the crystal lattice. [51] The absorption of light by the plasmon resonance fuels the plasmon itself, thereby fueling the electromagnetic field around the nanoparticle. The intensity of the absorption cross section of the plasmon is dependent on the size, [31, 41] structure,

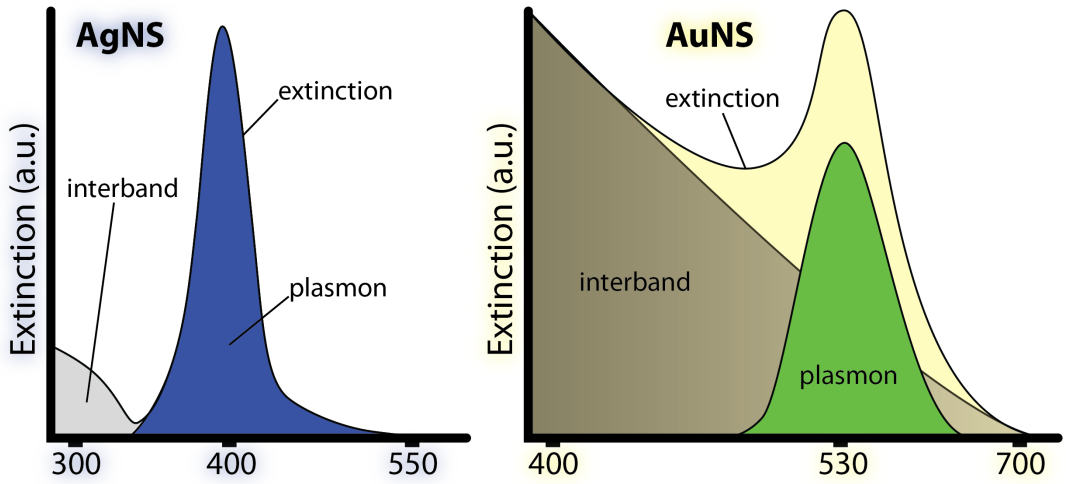

Figure 8: Deconvoluted model extinction spectra for silver nanospheres (left) and gold nanospheres (right) showing approximate interband absorbance, plasmon resonance frequency, and full extinction spectra.

[50, 43, 56] and composition[34] of the nanoparticle and is additionally affected by the dielectric of the surrounding medium [17, 70]. The plasmon decays via electron-phonon coupling on the picosecond timescale as it transfers energy to the positive nuclear lattice. [64] This energy then dissipates into the surrounding medium on the ca. 100 picosecond timescale through phonon-phonon coupling. [42]

Light can also be directly absorbed by interband transitions (Figure 8). Excitation of the interband transitions invariably results in thermal (i.e. non-radiative) relaxations. Absorbance by the interband is therefore non-advantageous to systems seeking to use NPs to enhance the absorbance of adjacent systems. The intensity of the interband increases with decreasing surface-area-to-volume ratio; however, as interband transitions are a property of the metal, their energies cannot be red- or blue-shifted by changing particle size or shape. For gold NPs, these interband absorption events occur in the UV and blue wavelength regions (Figure 8, right). For silver NPs, the interband lies in the UV (Figure 8, left). Absorbance by the interband also detracts from the strength of the plasmon field, which is relatively damped in gold because of the energetic proximity of the plasmon resonance to the interband

absorption edge in addition to the previously-discussed larger imaginary component of the gold dielectric function (Equation 4).

1.2.5 Coupling between Plasmonic Nanoparticles

When the distance between two plasmonic nanoparticles is less than the particle diameter, the electromagnetic plasmon fields around the NPs couple. [67] This coupling results from the plasmon on each NP becoming coherent with the plasmon on the other NP, [15] as illustrated in Figure 9. As the plasmons couple and their oscillations become coherent, a dipole is formed on each particle. These dipoles render the movement of the electrons more energetically favorable (e^- in one NP towards δ^+ on the other NP);[62] thus, coupling results in both (1) a decrease in the energy of the surface plasmon oscillation of the nanoparticle pair with respect to the isolated particle [28] and (2) an increase in the electromagnetic field intensity between the NPs. [65] The extent of the red-shift increases as NPs become closer and also increases as the number of coupled NPs increases. [35, 57, 66]

The resultant field intensity between coupled nanoparticles is greater than the sum of the two individual field strengths, and this is mainly attributed to coupling of higher order multipoles. [16, 60, 21] The coupling of these fields and consequent spike in field intensity between the pair leads to localized hot spots, which have found utility in applications such as sensing and detection of trace compounds for security screenings, [63] deweaponization of landmines, [61, 20] and disease detection [23, 44]. In these applications, field enhancements on the order of 10^{13} - 10^{15} have allowed for single-molecule detection. [54] Another interesting application of this coupling is explored in Chapter 2, where the clustering of gold nanoparticle probes on cell membranes is monitored over time as a function of the bathochromic shift in the plasmon resonance.

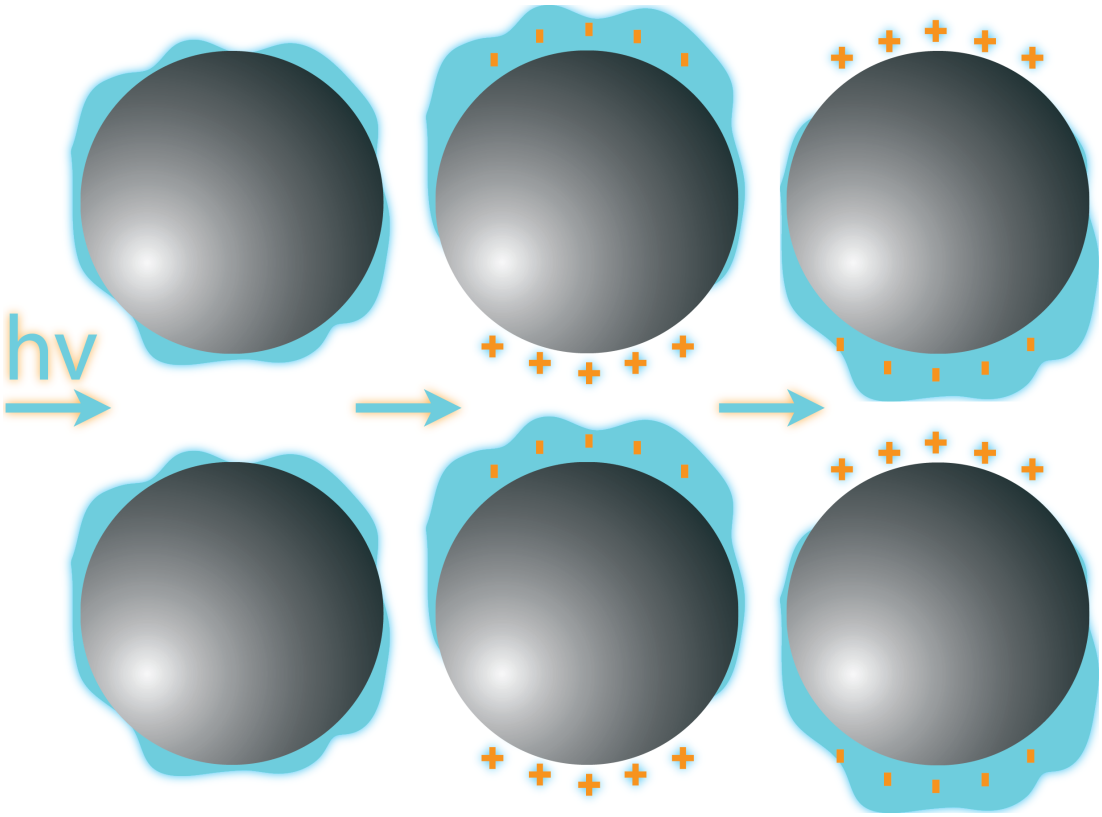

Figure 9: Coupling between adjacent nanoparticles results from oscillations of their valence electrons in coherence with one another, leading to the formation of a dipole and a resultant bathochromic shift in the oscillation frequency as the flux that comprises the plasmon becomes more energetically favorable.

1.3 REFERENCES

[1] Alvarez, M., Khoury, J., Schaaff, T., Shafigullin, M., Vezmar, I., and Whetten, R., "Optical absorption spectra of nanocrystal gold molecules," *The Journal of Physical Chemistry B*, vol. 101, no. 19, pp. 3706–3712, 1997.

[2] Bohren, C. and Huffman, D., *Absorption and scattering of light by small particles*. Wiley-Vch, 2008.

[3] Boyd, G., Rasing, T., Leite, J., and Shen, Y., "Local-field enhancement on rough surfaces of metals, semimetals, and semiconductors with the use of optical second-harmonic generation," *Physical Review B*, vol. 30, no. 2, p. 519, 1984.

[4] Brongersma, M., Hartman, J., and Atwater, H., "Electromagnetic energy transfer and switching in nanoparticle chain arrays below the diffraction limit," *Physical Review B*, vol. 62, no. 24, pp. 16356–16359, 2000.

[5] Brust, M., Walker, M., Bethell, D., Schiffrin, D., and Whyman, R., "Synthesis of thiol-derivatised gold nanoparticles in a two-phase liquid–liquid system," *J. Chem. Soc., Chem. Commun.*, no. 7, pp. 801–802, 1994.

[6] Catchpole, K. and Polman, A., "Plasmonic solar cells," *Optics express*, vol. 16, no. 26, pp. 21793–21800, 2008.

[7] Cheng, C., Kirkbride, T., Batchelder, D., Lacey, R., and Sheldon, T., "In situ detection and identification of trace explosives by raman microscopy," *Journal of forensic sciences*, vol. 40, pp. 31–31, 1995.

[8] Colomban, P., "The use of metal nanoparticles to produce yellow, red and iridescent colour, from bronze age to present times in lustre pottery and glass:

solid state chemistry, spectroscopy and nanostructure," *Journal of Nano Research*, vol. 8, pp. 109–132, 2009.

[9] Daniel, M., Astruc, D., and others, "Gold nanoparticles: assembly, supramolecular chemistry, quantum-size-related properties, and applications toward biology, catalysis, and nanotechnology," *Chemical Reviews-Columbus*, vol. 104, no. 1, p. 293, 2004.

[10] Ding, I., Zhu, J., Cai, W., Moon, S., Cai, N., Wang, P., Zakeeruddin, S., Grätzel, M., Brongersma, M., Cui, Y., and others, "Plasmonic dye-sensitized solar cells," *Advanced Energy Materials*, vol. 1, no. 1, pp. 52–57, 2011.

[11] El-Sayed, M., "Some interesting properties of metals confined in time and nanometer space of different shapes," *Accounts of Chemical Research*, vol. 34, no. 4, pp. 257–264, 2001.

[12] Eustis, S. and El-Sayed, M. A., "Why gold nanoparticles are more precious than pretty gold: Noble metal surface plasmon resonance and its enhancement of the radiative and nonradiative properties of nanocrystals of different shapes," *Chemical Society Reviews*, vol. 35, no. 3, pp. 209–217, 2006. Eustis, S El-Sayed, MA.

[13] Fedlheim, D. and Foss, C., *Metal nanoparticles: synthesis, characterization, and applications*. CRC, 2001.

[14] Genov, D., Sarychev, A., Shalaev, V., and Wei, A., "Resonant field enhancements from metal nanoparticle arrays," *Nano Letters*, vol. 4, no. 1, pp. 153–158, 2004.

[15] Ghosh, S., Pal, T., and others, "Interparticle coupling effect on the surface plasmon resonance of gold nanoparticles: from theory to applications," *Chemical Reviews-Columbus*, vol. 107, no. 11, pp. 4797–4862, 2007.

[16] Gunnarsson, L., Rindzevicius, T., Prikulis, J., Kasemo, B., Käll, M., Zou, S., and Schatz, G., "Confined plasmons in nanofabricated single silver particle pairs: experimental observations of strong interparticle interactions," *The Journal of Physical Chemistry B*, vol. 109, no. 3, pp. 1079–1087, 2005.

[17] Haes, A. and Van Duyne, R., "A nanoscale optical biosensor: sensitivity and selectivity of an approach based on the localized surface plasmon resonance spectroscopy of triangular silver nanoparticles," *Journal of the American Chemical Society*, vol. 124, no. 35, pp. 10596–10604, 2002.

[18] Hao, E., Schatz, G. C., and Hupp, J. T., "Synthesis and optical properties of anisotropic metal nanoparticles," *Journal of Fluorescence*, vol. 14, no. 4, pp. 331–341, 2004.

[19] Hao, E. and Schatz, G., "Electromagnetic fields around silver nanoparticles and dimers," *The Journal of chemical physics*, vol. 120, p. 357, 2004.

[20] Harper, R. J., "Improving the scientific reliability of biological detection of explosives by canis familiaris: Active odour signatures and their implications," *Proceedings of the 8th International Symposium on the Analysis and Detection of Explosives (ISADE), Ottowa, Canada, 2004*, 2005.

[21] Hicks, E., Zou, S., Schatz, G., Spears, K., Van Duyne, R., Gunnarsson, L., Rindzevicius, T., Kasemo, B., and Käll, M., "Controlling plasmon line shapes through diffractive coupling in linear arrays of cylindrical nanoparticles fabricated by electron beam lithography," *Nano letters*, vol. 5, no. 6, pp. 1065–1070, 2005.

[22] Hildebrandt, P. and Stockburger, M., "Surface-enhanced resonance raman spectroscopy of rhodamine 6g adsorbed on colloidal silver," *The Journal of Physical Chemistry*, vol. 88, no. 24, pp. 5935–5944, 1984.

[23] Huang, X. H., El-Sayed, I. H., Qian, W., and El-Sayed, M. A., "Cancer cells assemble and align gold nanorods conjugated to antibodies to produce highly enhanced, sharp, and polarized surface raman spectra: A potential cancer diagnostic marker," *Nano Letters*, vol. 7, no. 6, pp. 1591–1597, 2007. Huang, Xiaohua El-Sayed, Ivan H. Qian, Wei El-Sayed, Mostafa A.

[24] Huang, X. H., Jain, P. K., El-Sayed, I. H., and El-Sayed, M. A., "Plasmonic photothermal therapy (pptt) using gold nanoparticles," *Lasers in Medical Science*, vol. 23, no. 3, pp. 217–228, 2008. Huang, Xiaohua Jain, Prashant K. El-Sayed, Ivan H. El-Sayed, Mostafa A.

[25] Hutter, E. and Fendler, J., "Exploitation of localized surface plasmon resonance," *Advanced Materials*, vol. 16, no. 19, pp. 1685–1706, 2004.

[26] Jain, P. K., Eustis, S., and El-Sayed, M. A., "Plasmon coupling in nanorod assemblies: Optical absorption, discrete dipole approximation simulation, and exciton-coupling model," *Journal of Physical Chemistry B*, vol. 110, no. 37, pp. 18243–18253, 2006. Jain, Prashant K. Eustis, Susie El-Sayed, Mostafa A.

[27] Jain, P. K., Huang, X. H., El-Sayed, I. H., and El-Sayed, M. A., "Noble metals on the nanoscale: Optical and photothermal properties and some applications in imaging, sensing, biology, and medicine," *Accounts of Chemical Research*, vol. 41, no. 12, pp. 1578–1586, 2008. Jain, Prashant K. Huang, Xiaohua El-Sayed, Ivan H. El-Sayed, Mostafa A.

[28] Jain, P., Huang, W., and El-Sayed, M., "On the universal scaling behavior of the distance decay of plasmon coupling in metal nanoparticle pairs: a plasmon ruler equation," *Nano Letters*, vol. 7, no. 7, pp. 2080–2088, 2007.

[29] Jain, P. K. and El-Sayed, M. A., "Surface plasmon coupling and its universal size scaling in metal nanostructures of complex geometry: Elongated particle

pairs and nanosphere trimers," *The Journal of Physical Chemistry C*, vol. 112, no. 13, pp. 4954–4960, 2008. doi: 10.1021/jp7120356.

[30] Jensen, T., Kelly, L., Lazarides, A., and Schatz, G., "Electrodynamics of noble metal nanoparticles and nanoparticle clusters," *Journal of Cluster Science*, vol. 10, no. 2, pp. 295–317, 1999.

[31] Kelly, K., Coronado, E., Zhao, L., and Schatz, G., "The optical properties of metal nanoparticles: the influence of size, shape, and dielectric environment," *The Journal of Physical Chemistry B*, vol. 107, no. 3, pp. 668–677, 2003.

[32] Khaing Oo, M., Yang, Y., Hu, Y., Gomez, M., Du, H., and Wang, H., "Gold nanoparticle-enhanced and size-dependent generation of reactive oxygen species from protoporphyrin ix," *ACS nano*, vol. 6, no. 3, pp. 1939–1947, 2012.

[33] Klimov, V., Mikhailovsky, A., Xu, S., Malko, A., Hollingsworth, J., Leatherdale, C., Eisler, H., and Bawendi, M., "Optical gain and stimulated emission in nanocrystal quantum dots," *Science*, vol. 290, no. 5490, pp. 314–317, 2000.

[34] Kreibig, U. and Vollmer, M., "Optical properties of metal clusters," 1995.

[35] Lazarides, A. and Schatz, G., "Dna-linked metal nanosphere materials: structural basis for the optical properties," *The Journal of Physical Chemistry B*, vol. 104, no. 3, pp. 460–467, 2000.

[36] Lechner, M. and Mächtle, W., "Characterization of nanoparticles," in *Macromolecular Symposia*, vol. 145, pp. 1–7, Wiley Online Library, 1999.

[37] Lee, K. S. and El-Sayed, M. A., "Dependence of the enhanced optical scattering efficiency relative to that of absorption for gold metal nanorods on aspect

ratio, size, end-cap shape, and medium refractive index," *Journal of Physical Chemistry B*, vol. 109, no. 43, pp. 20331–20338, 2005. Lee, KS El-Sayed, MA.

[38] Lee, K. and El-Sayed, M., "Gold and silver nanoparticles in sensing and imaging: sensitivity of plasmon response to size, shape, and metal composition," *The Journal of Physical Chemistry B*, vol. 110, no. 39, pp. 19220–19225, 2006.

[39] Leutwyler, W., Bürgi, S., and Burgl, H., "Semiconductor clusters, nanocrystals, and quantum dots," *Science*, vol. 271, p. 933, 1996.

[40] Link, S., Burda, C., Wang, Z. L., and El-Sayed, M. A., "Electron dynamics in gold and gold-silver alloy nanoparticles: The influence of a nonequilibrium electron distribution and the size dependence of the electron-phonon relaxation," *Journal of Chemical Physics*, vol. 111, no. 3, pp. 1255–1264, 1999. Link, S Burda, C Wang, ZL El-Sayed, MA.

[41] Link, S. and El-Sayed, M., "Size and temperature dependence of the plasmon absorption of colloidal gold nanoparticles," *The Journal of Physical Chemistry B*, vol. 103, no. 21, pp. 4212–4217, 1999.

[42] Link, S. and El-Sayed, M., "Optical properties and ultrafast dynamics of metallic nanocrystals," *Annual review of physical chemistry*, vol. 54, no. 1, pp. 331–366, 2003.

[43] Link, S., Mohamed, M. B., and El-Sayed, M. A., "Simulation of the optical absorption spectra of gold nanorods as a function of their aspect ratio and the effect of the medium dielectric constant," *Journal of Physical Chemistry B*, vol. 103, no. 16, pp. 3073–3077, 1999. Link, S Mohamed, MB El-Sayed, MA.

[44] Lui, H., Zhao, J., McLean, D., and Zeng, H., "Real-time raman spectroscopy for in vivo skin cancer diagnosis," *Cancer research*, vol. 72, no. 10, pp. 2491–2500, 2012.

[45] Maier, S., Kik, P., Atwater, H., Meltzer, S., Harel, E., Koel, B., and Requicha, A., "Local detection of electromagnetic energy transport below the diffraction limit in metal nanoparticle plasmon waveguides," *Nature materials*, vol. 2, no. 4, pp. 229–232, 2003.

[46] Moore, D., "Instrumentation for trace detection of high explosives," *Review of Scientific Instruments*, vol. 75, no. 8, pp. 2499–2512, 2004.

[47] Moores, A. and Goettmann, F., "The plasmon band in noble metal nanoparticles: an introduction to theory and applications," *New J. Chem.*, vol. 30, no. 8, pp. 1121–1132, 2006.

[48] Murphy, C., "Nanocubes and nanoboxes," *Science*, vol. 298, no. 5601, pp. 2139–2141, 2002.

[49] Murphy, C., Sau, T., Gole, A., and Orendorff, C., "Surfactant-directed synthesis and optical properties of one-dimensional plasmonic metallic nanostructures," *Mrs Bulletin*, vol. 30, no. 05, pp. 349–355, 2005.

[50] Murphy, C., Sau, T., Gole, A., Orendorff, C., Gao, J., Gou, L., Hunyadi, S., and Li, T., "Anisotropic metal nanoparticles: synthesis, assembly, and optical applications," *The Journal of Physical Chemistry B*, vol. 109, no. 29, pp. 13857–13870, 2005.

[51] Muskens, O., Del Fatti, N., Vallée, F., Huntzinger, J., Billaud, P., and Broyer, M., "Single metal nanoparticle absorption spectroscopy and optical characterization," *Applied physics letters*, vol. 88, no. 6, pp. 063109–063109, 2006.

[52] Nakayama, K., Tanabe, K., and Atwater, H., "Plasmonic nanoparticle enhanced light absorption in gaas solar cells," *Applied Physics Letters*, vol. 93, no. 12, pp. 121904–121904, 2008.

[53] Narayanan, R. and El-Sayed, M. A., "Shape-dependent catalytic activity of platinum nanoparticles in colloidal solution," *Nano Letters*, vol. 4, no. 7, pp. 1343–1348, 2004. Narayanan, R El-Sayed, MA.

[54] Nie, S. M. and Emery, S. R., "Probing single molecules and single nanoparticles by surface-enhanced raman scattering," *Science*, vol. 275, no. 5303, pp. 1102–1106, 1997. ISI Document Delivery No.: WJ503 Times Cited: 2000 Cited Reference Count: 48.

[55] Nolte, D., "Optical scattering and absorption by metal nanoclusters in gaas," *Journal of applied physics*, vol. 76, no. 6, pp. 3740–3745, 1994.

[56] Oldenburg, S., Averitt, R., Westcott, S., and Halas, N., "Nanoengineering of optical resonances," *Chemical Physics Letters*, vol. 288, no. 2, pp. 243–247, 1998.

[57] Park, S., Lazarides, A., Mirkin, C., Brazis, P., Kannewurf, C., and Letsinger, R., "The electrical properties of gold nanoparticle assemblies linked by dna," *Angewandte Chemie International Edition*, vol. 39, no. 21, pp. 3845–3848, 2000.

[58] Pustovit, V. and Shahbazyan, T., "Finite-size effects in surface-enhanced raman scattering in noble-metal nanoparticles: a semiclassical approach," *JOSA A*, vol. 23, no. 6, pp. 1369–1374, 2006.

[59] Shu, J., Wilson, K., Ahmed, M., Leone, S., Graf, C., and Rühl, E., "Elastic light scattering from nanoparticles by monochromatic vacuum-ultraviolet radiation," *The Journal of chemical physics*, vol. 124, p. 034707, 2006.

[60] Shuford, K., Ratner, M., and Schatz, G., "Multipolar excitation in triangular nanoprisms," *The Journal of chemical physics*, vol. 123, p. 114713, 2005.

[61] Singh, S., "Sensors - an effective approach for the detection of explosives," *Journal of Hazardous Materials*, vol. 144, no. 1-2, pp. 15–28, 2007. ISI Document Delivery No.: 178BV Times Cited: 15 Cited Reference Count: 87 Singh, Suman.

[62] Šloufová-Srnová, I. and Vlčková, B., "Two-dimensional assembling of au nanoparticles mediated by tetrapyridylporphine molecules," *Nano Letters*, vol. 2, no. 2, pp. 121–125, 2002.

[63] Smith, W., "Practical understanding and use of surface enhanced raman scattering and surface enhanced resonance raman scattering in chemical and biological analysis," *Chemical Society Reviews*, vol. 37, no. 5, pp. 955–964, 2008.

[64] Stietz, F., Bosbach, J., Wenzel, T., Vartanyan, T., Goldmann, A., and Träger, F., "Decay times of surface plasmon excitation in metal nanoparticles by persistent spectral hole burning," *Physical review letters*, vol. 84, no. 24, pp. 5644–5647, 2000.

[65] Storhoff, J., Elghanian, R., Mucic, R., Mirkin, C., and Letsinger, R., "One-pot colorimetric differentiation of polynucleotides with single base imperfections using gold nanoparticle probes," *Journal of the American Chemical Society*, vol. 120, no. 9, pp. 1959–1964, 1998.

[66] Storhoff, J., Lazarides, A., Mucic, R., Mirkin, C., Letsinger, R., and Schatz, G., "What controls the optical properties of dna-linked gold nanoparticle assemblies?," *Journal of the American Chemical Society*, vol. 122, no. 19, pp. 4640–4650, 2000.

[67] Su, K., Wei, Q., Zhang, X., Mock, J., Smith, D., and Schultz, S., "Interparticle coupling effects on plasmon resonances of nanogold particles," *Nano Letters*, vol. 3, no. 8, pp. 1087–1090, 2003.

[68] Sun, Y. and Xia, Y., "Shape-controlled synthesis of gold and silver nanoparticles," *Science*, vol. 298, no. 5601, pp. 2176–2179, 2002.

[69] Thompson, D., "Michael faraday's recognition of ruby gold: the birth of modern nanotechnology," *Gold Bulletin*, vol. 40, no. 4, pp. 267–269, 2007.

[70] Underwood, S. and Mulvaney, P., "Effect of the solution refractive index on the color of gold colloids," *Langmuir*, vol. 10, no. 10, pp. 3427–3430, 1994.

[71] Yen, C., Hayden, S., Dreaden, E., Szymanski, P., and El-Sayed, M., "Tailoring plasmonic and electrostatic field effects to maximize solar energy conversion by bacteriorhodopsin, the other natural photosynthetic system," *Nano letters*, vol. 11, no. 9, pp. 3821–3826, 2011.

CHAPTER II

NANOPARTICLES AT BIOLOGICAL INTERFACES

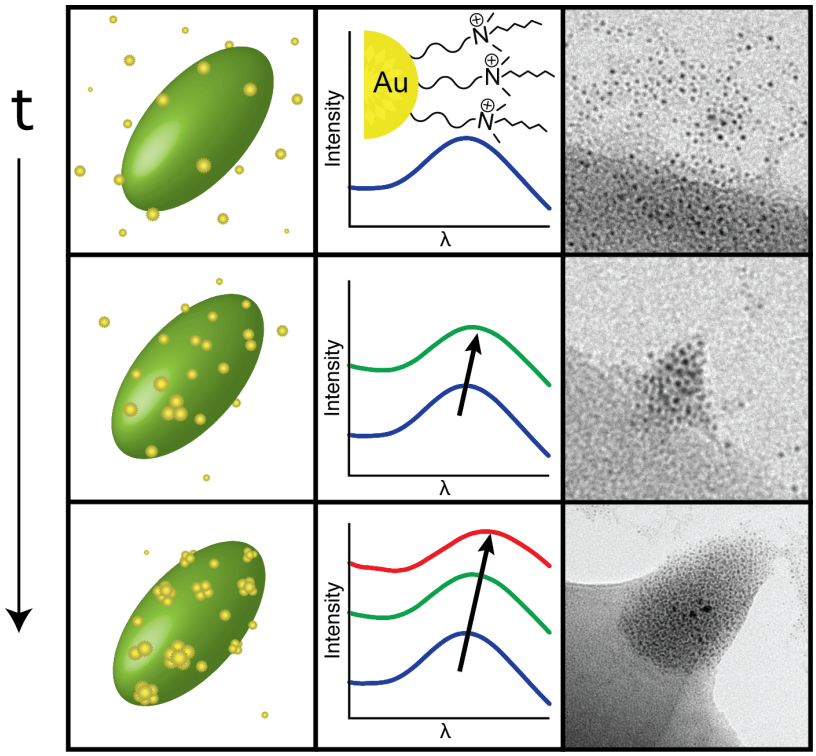

Figure 10: Cartoon and accompanying TEM images and spectra showing a bathochromic shift over time as NPs aggregate on the surface of *E. coli*.

2.1 Chapter Summary

The constituents, dynamics, and macroscopic organization of cell membranes are of consequence to areas of study as impactful as drug design [35] and therapeutics. [12, 2] In these areas, the cell membrane defines the barrier between efficacy and impotence; therefore, the nature of the interaction of nanoscale species with cell membranes is of great concern. Fundamental insight into the interaction of nanoparticles with bacterial cell membranes would provide direction in the design of bacteriacidal agents

and sensor systems. [25, 26, 30, 8] However, the interaction of AuNPs with bacterial cell membranes is not well understood. No good models exist concerning how this interaction takes place or to which loci, if any, the AuNPs are most attracted.

Cationic monolayer-protected gold nanoparticles (AuNPs) with sizes of 2 or 6 nm interact with the cell membranes of *Escherichia coli* (Gram-negative) and *Bacillus subtilis* (Gram-positive), resulting in the formation of strikingly distinct AuNP surface aggregation patterns or lysis, depending upon the size of the AuNPs. Upon proteolytic treatment of the bacteria, the distinct aggregation patterns disappear. Distinct topographic mapping of the bacterial surface by functionalized gold nanoparticles demonstrates the effect of hydrophobicity and local charge on real-time AuNP association on the surface of a living organism. This work also has implications in phamacology, as mechanical perturbations of specific regions of the cell membrane may aid in some types of drug delivery. [14]

2.2 Bacterial Cell Walls

Bacteria are encapsulated in cell walls that give them both their characteristic shape and determine their virulence. In fact, the symptoms of many diseases can be ellicited in humans merely by injection of isolated bacterial cell walls. This gives bacterial cell walls considerable medical significance and has led to the use of these types of injections as vaccinations to invoke the patient's immune response against a particular strain or species of bacteria.

2.2.1 Bacterial Cell Wall Constituents

Bacterial cell walls are made up of peptidoglycan, which is itself composed of polysaccharide and polypeptide chains. These form several concentric layers of covalently cross-linked β-sheets that completely encapsulate the cell. Two main branches of bacteria exist today, and these differ most strikingly in the constitution of their cell membranes. The surface layer of Gram-positive (Gram+) bacteria is a thick layer (ca.

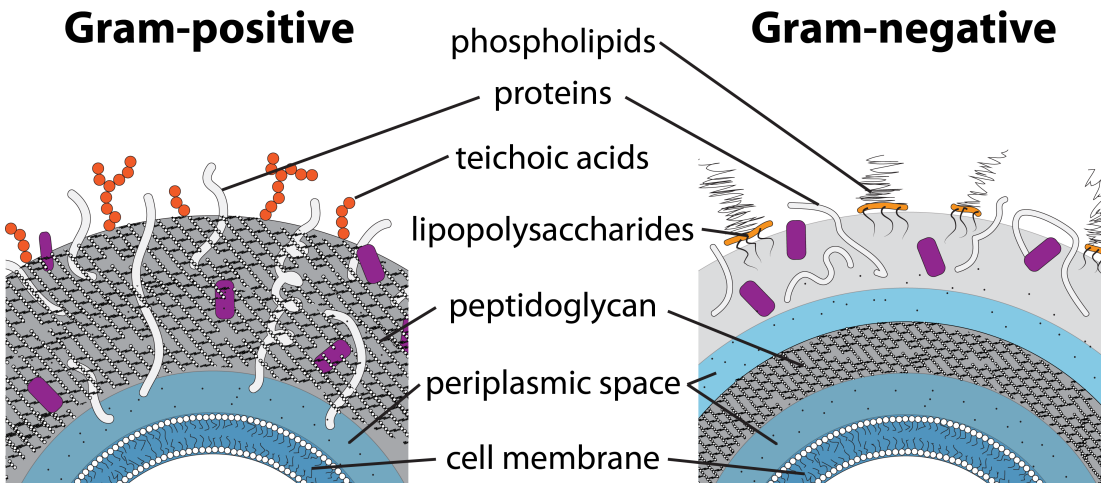

Figure 11: Schematic of Gram-positive and Gram-negative cell wall constituents. The most external layer of Gram-positive bacteria is the peptidoglycan layer, which is riddled with teichoic acids. By contrast, Gram-negative bacteria have a second membrane over their peptidoglycan layer that prevents uptake of Gram stain.

25 nm) of peptidoglycan [32] that is riddled with proteins and teichoic acids. [1, 3] Pepetidoglycan readily absorbs Gram stain - a mixture of crystal violet and iodine - thus, the designation as Gram-positive. Gram-negative (Gram-) bacteria have an additional membrane over their much thinner peptidoglycan layer (ca. 3 nm) that prevents them from taking up the Gram stain. [10, 5] This additional membrane is composed of lipopolysaccharides and phospholipids (Figure 11).

Both Gram-negative and Gram-positive bacterial cell surfaces are negatively charged, and each has varying degrees of surface hydrophobicity. [9] While the constituents of the bacterial cell surface and their functionalities are well understood, the spatial arrangement of these molecular species is less explored from a supramolecular point of view.

2.2.2 Bacterial Cell Wall Curvature

Cell surface deformation into curved structures is crucial for various cellular processes, including endocytosis, cytokinesis, and cytoskeletal protrusion. [17] The formation of several curved membrane assemblies, including buds, lipid tubules, [27] and blebs,

[11] results from mechanisms such as binding of curved proteins, changes in lipid composition, etc. [23]

Specific lipid species (e.g. cholesterol) in cell wall microdomains are known to be present in higher local concentrations at the sites of many curved membrane structures, illustrating the possible involvement of membrane microdomains in cytoskeletal rearrangements. [31, 24] Sasaki et al. have shown that lipid domains can sterically confine proteins, leading to deformation and consequent tubulation of model membranes. [29] However, other topological membrane features of supramolecular interest, such as hydrophobic domains, local charges, and the role of these in membrane curvature in living organisms, have yet to be systematically explored.

2.3 Nanoparticles and Cell Membranes

Positively charged gold nanoparticles (AuNPs) can selectively interact with bacterial cell surfaces via complementary charge interactions. [25] Murphy and coworkers [4] demonstrated that Gram-positive *B. cereus* coordinates to CTAB-protected gold nanorods, but the coverage of the bacteria was found to be isotropic. Similar observations were made by other groups that investigated the interaction of AuNPs with microbes to access bioinspired advanced materials. [15, 36, 20] Jiang and coworkers [37] demonstrated that diamino pyrimidine thiol-functionalized, cationic, 3 nm-sized AuNPs induce formation of outer membrane vesicles (i.e. blebbing) that lead to membrane disruption and uncontrolled release of bacterial DNA in *P. aeruginosa*.

The role of charge and hydrophobicity in the interaction of nanoscale species with cell membranes is of utmost interest in areas such as pharmacology. We investigated the mesoscopic interactions of functionalized AuNPs with representative bacterial strains of both Gram stain types (*E. coli* and *B. subtilis*). To this end, we exploit two interesting properties of AuNPs: their high imaging contrast in transmission electron microscopy (TEM) and their near-field coupling, which is observable via UV-Vis

absorption spectroscopy. As this coupling occurs when two or more gold nanoparticles are proximal, it serves as an indicator of gold nanoparticle cluster formation. Our study confers binding ability on AuNPs through the use of positive charge and hydrophobic ligands. In our system, the positive charges on the particle will promote general particle-bacteria electrostatic association while the hydrophobic ligands will impart hydrophobic specificity to these interactions. These particles are used to demonstrate cell surface mapping and to resolve the effects of these interactions on membrane curvature.

We show that positively charged, 2- and 6 nm gold-core hydrophobic nanoprobes localize into specific, mesoscopic arrangements on the cell surfaces of strains of *B. subtilis* and *E. coli*. We exploit this surprising nanoparticle self-organization to elucidate the fundamental topographical properties of hydrophobicity and charge on different bacterial surfaces. Herein, we demonstrate the utility of gold nanoprobes for cell surface mapping and demonstrate enhanced toxicity that is dependent both on the size of the nanoparticle and the Gram stain of the cell.

The antimicrobial activity of these monolayer-protected AuNPs, which was also investigated by Feldheim and co-workers, [6] is an attractive applicative boon. Depending upon the specific membrane and NP structure, membrane interaction with nanoparticulate matter can result in blebbing, tubule formation, [37, 6, 29] or creation or enlargement of membrane defects, etc., [22, 21] in a subtle structural interplay of the NP and membrane structures.

2.3.1 Cationic, Hydrophobic AuNPs

Nanoparticles were surface-passivated with a hexyl-substituted, ammonium-functionalized thiol (Figure 12) as a protective coat, as this ligand had previously shown optimal interaction with different bacterial species and strains, apparently displaying the correct mix of hydrophobicity and positive charge. [25] We examined both 2 nm (**NP2**) and

6 nm sized (**NP1**) AuNPs. The latter display a well-behaved plasmon band upon aggregation, and the resulting bathochromic shift of this band correlates with the number and separation distance of interacting particles. Decreasing the interparticle distance and increasing the number of particles leads to larger shift, giving a valuable tool to study aggregation of **NP1** on bacteria in suspension.

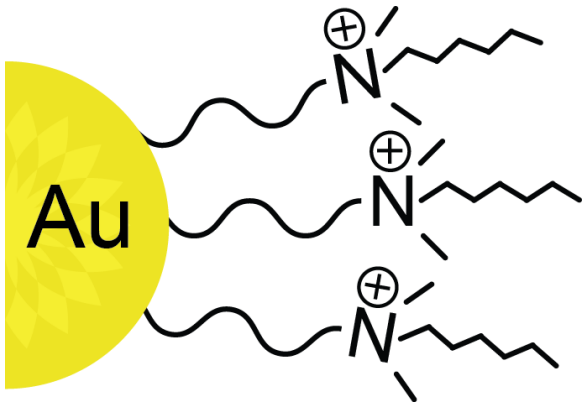

Figure 12: Schematic diagram of a monolayer-protected AuNP used in this study (**NP1**, 6 nm diameter; **NP2**, 2 nm diameter)

NP1 were obtained from place exchange of undecanethiol-capped AuNPs formed via the heat-induced size evolution method;[16, 34] **NP2** were obtained via place-exchange of pentane-thiol-capped AuNPs formed through the Schiffrin-Brust method. [7] In the first experiment (Figures 13, 14) **NP1** was mixed with a bacterial suspension of *B. subtilis* or *E. coli* (Details see AppendixA). Aliquots of this NP/bacteria mixture were removed successively at increasing time intervals, applied to TEM grids, and fixed with 1% uranyl acetate. Imaging with a JEOL JEM-1400 TEM equipped with Gatan Orius SC1000 and Ultrascan 1000 CCD cameras yielded the images seen in Figures 13, 14 and 19.

2.3.2 TEM Investigation of the Interaction of 6 nm AuNP Probes with Bacterial Cell Walls

Aggregation in the *B. subtilis* samples begins immediately and progresses more rapidly to full aggregation than in the *E. coli* samples. However, all bacteria examined show

aggregation patterns, with no cell showing random isolated particle distribution over its surface. **NP1** sits on top of the glycocalix, the tough outer membrane of Gram+ bacteria. With increasing time, the number and the size of the discrete aggregates increases and a striking pattern develops (Figure 13D). The micrographs indicate that **NP1** either clusters on hotspots of increased hydrophobicity and/or negative charge density on the bacterial surface or induces hotspots with increased binding to the cell. In Figure 13D, the aggregates have higher contrast, and some of them are located on the periphery on membrane protrusions of the bacterium in this particular image view, suggesting that binding occurs at the bacterial surface and that **NP1** is not endocytosed or otherwise translocated to the inside of the bacterium.

In the *E. coli* samples, the formation of **NP1** aggregates is also seen but is less developed than in *B. subtilis* (Figure 14). Here, at short time intervals, single **NP1** appear almost randomly distributed over the body of the bacterium. However, at increased exposure times, aggregation is apparent, though the aggregates are smaller than those observed in the *B. subtilis* samples. After 30 min, *E. coli* features a large number of smaller aggregates that are evenly dispersed over the whole surface of the bacterium. Figures 13 and 14 show typical micrographs in which the interaction of **NP1** with bacterial cells is demonstrated. Control micrographs of **NP1** in fresh and used growth media are presented in Appendix A.

2.3.3 Spectroscopic Investigation of the Interaction of 6 nm AuNP Probes with Bacterial Cell Walls

We next investigated the kinetics of the aggregation phenomenon as a collective on many bacterial cells exploiting the use of the localized surface plasmon resonance on these nanoparticles. Surface plasmon coupling is observed when two or more particles are close together. [13, 33] This results in a red-shift in the plasmon band absorption as the energy of the electronic oscillation responsible for the plasmon decreases. The strength of this coupling is dependent on the interparticle distance;

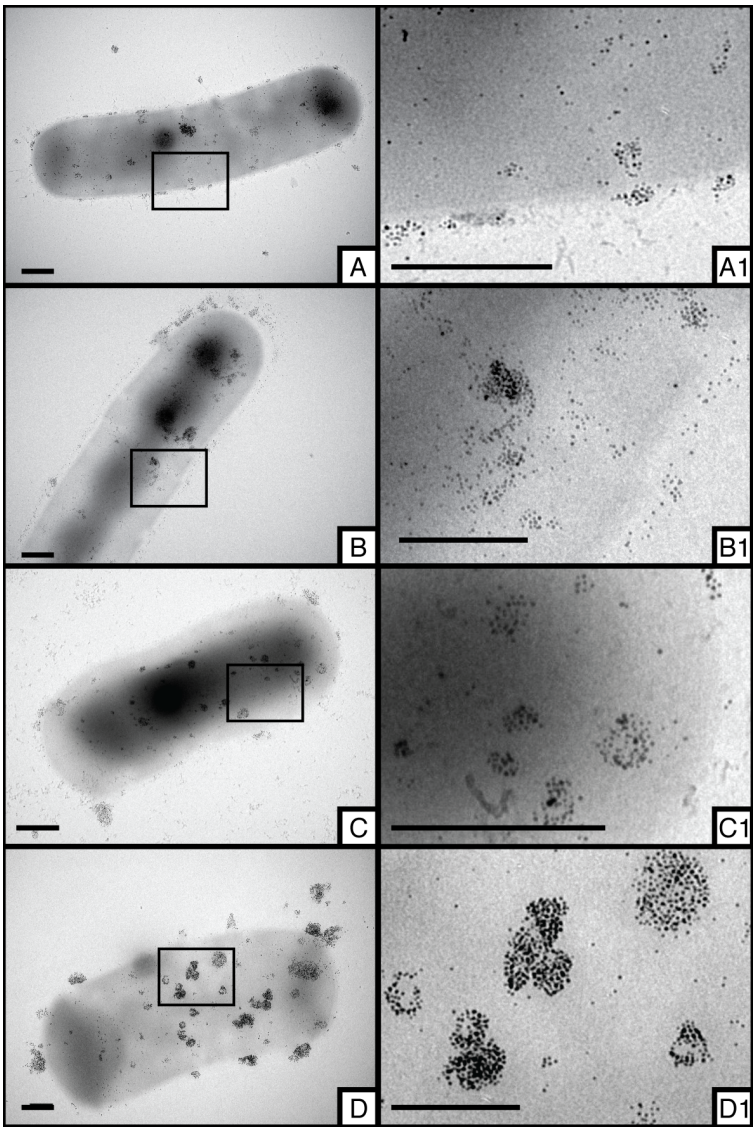

Figure 13: TEM images of timed stages of interaction of **NP1** with *B. subtilis* with corresponding higher magnification views of the boxed areas in the second panel. Shows the development of distinct aggregation patterns over time. Images were collected at incubation time points of (A) 20 sec, (B) 1.5 min, (C) 3 min, and (D) 10 min. Scale bars are 200 nm.

[18] thus, the degree of red-shift in the plasmon band is indicative of more coupling events or stronger coupling interactions, indicating the formation of either larger, more numerous, or more tightly packed clusters of particles.

Figure 15A displays the time-dependent UV-vis spectra of a suspension of *B. subtilis* upon mixing with **NP1**, where the band normally associated with gold

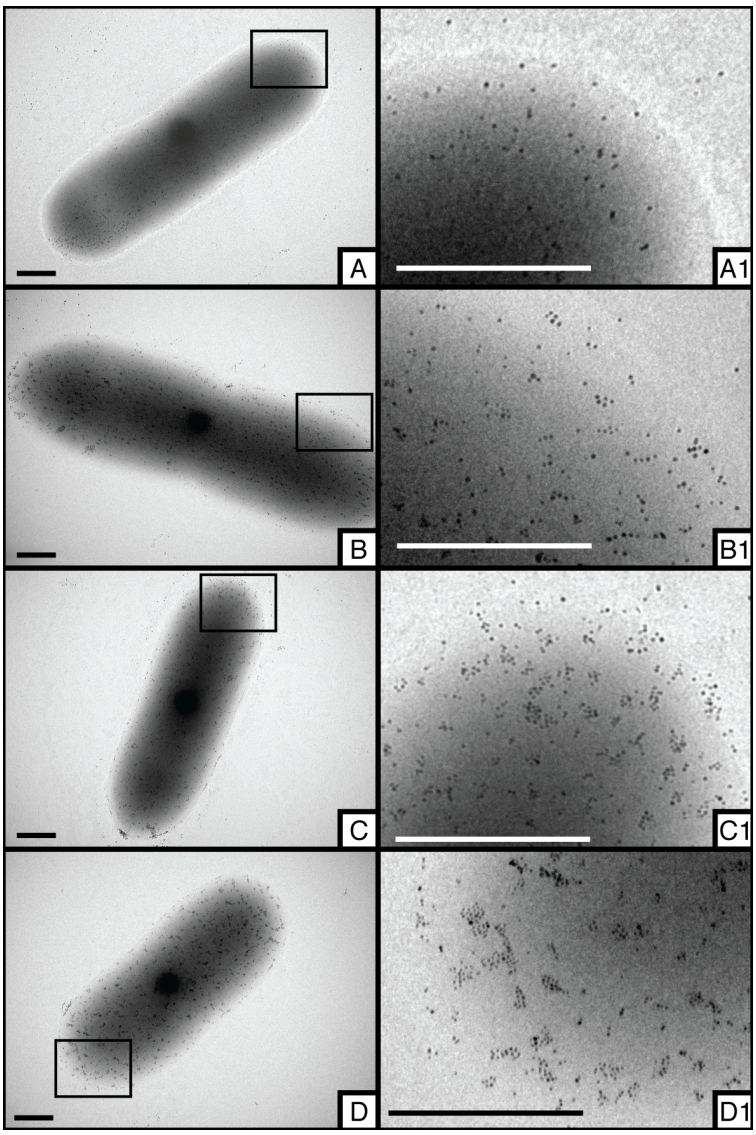

Figure 14: TEM images of timed stages of interaction of **NP1** with *E. coli* with corresponding higher magnification views of the boxed areas in the second panel. Images were collected at incubation time points of (A) 20 sec, (B) 1.5 min, (C) 5 min, and (D) 30 min. Scale bars are 200 nm.

nanospheres red-shifts, broadens, and increases in intensity as the gold nanospheres form into clusters. [19] When fit with an exponential decay, $y_0 = A_0 + exp\frac{-x}{t}$, the rate of cluster formation is indicated by the rate constant for these curves (t), whereas the size of the resulting clusters is indicated by the magnitude of the final shift in the plasmon peak (A_0). At the beginning, the plasmon band of **NP1** is observed at 532

nm, but after 30 seconds, the extinction profile already displays a red-shift (an indication of plasmonic coupling as nanoparticles approach each other) and an increase in intensity as the large particle aggregates scatter more light. After ca. 5 minutes, equilibrium is reached; the band now peaks at 559 nm and does not shift further to the red. In Figure 15B, the frequency of the plasmon peak position is plotted against time.

The analogous experiment was performed for *E. coli* with **NP1**, and the observed shift is considerably less over the same time frame (from 532 nm to 545 nm), with an ultimate endpoint of 552 nm after equilibrium is reached at ca. 900 seconds. This suggests both the formation of significantly smaller aggregates and a decreased rate of aggregate formation (Figure 16). The results from the direct TEM observation and the spectroscopic experiments are therefore mutually reinforcing. The larger cluster formation in the case of *B. subtilis* is presumably due to the higher local charge and hydrophobic character of its surface. [9]

2.3.4 The Role of Surface Proteins in NP1 Aggregation Patterns

The stark difference in the aggregation behavior of *E. coli* and *B. subtilis* could arise as a result of the different lipid concentrations, the gross constitution of the membranes, or even differences in specific protein complexes that reside on the surface of the bacteria. [28] To investigate the role of surface proteins in the aggregation phenomena, we examined aggregation on cells that had recieved proteolytic treatment (treatment with a 1% trypsin solution for 24 h). Under these conditions, the cells are still alive but are stripped of their surface proteins. Membrane lipid content is unaffected.

Figure 17 displays the micrographs of trypsin-treated *E. coli* and *B. subtilis* after addition of **NP1**. There is binding of the NP to the bacterial surfaces, but the clustering has disappeared in both cases. Surface protein removal does not preclude particle association to the bacterial surface, but it does affect the localization of these

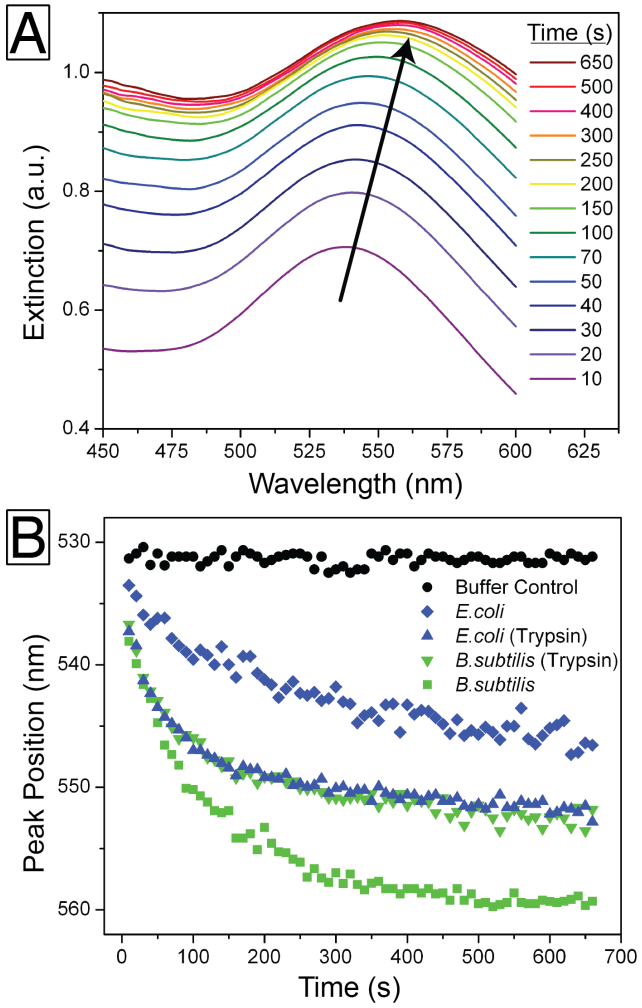

Figure 15: (**A**) The plasmonic peak red-shift of **NP1** resulting from aggregation on the cell surface of *B. subtilis* from 10 s to 650 s exposure time. *E. coli* proceeds similarly but with a differing final wavelength peak position and rate (not shown). (**B**) Plasmon peak position over time for the aggregation of **NP1** on the surface of *E. coli* (blue) and *B. subtilis* (green) for trypsin treated (triangles) and untreated (squares) cells and for cells treated with only buffer (black). Aggregation into clusters proceeds more quickly and results in larger overall cluster formation in *B. subtilis* compared to *E. coli*.

particles into discrete clusters. Thus, the particle association to the surface likely arises from interactions with the bacterial membrane itself.

Whereas untreated bacteria exhibit both strain-specific cluster size and strain-specific rate of cluster formation, trypsin-treated cells of both strains exhibit aggregation kinetics that are almost superimposable (Figure 15B, blue and green triangles),

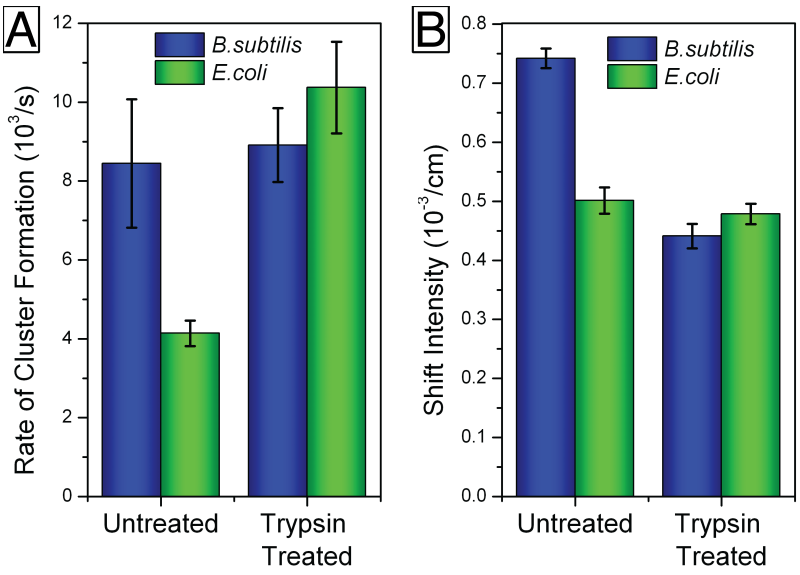

Figure 16: Rate of cluster formation (**A**) and degree of plasmon peak shift (**B**) for trypsin-treated and untreated *B. subtilis* (blue) and *E. coli* (green). Both the rate of formation and the final cluster size are the same for both strains following proteolytic treatment.

with the same rate of formation and the same final number of coupled particles. This results in a rate of surface attachment similar to that seen in *B. subtilis* and a final plasmon shift similar to that observed in *E. coli*. These data suggest that the difference in surface proteins between *B. subtilis* and *E. coli* is likely responsible for the difference observed in the clustering on each strain but has little effect on particle attachment to the surface.

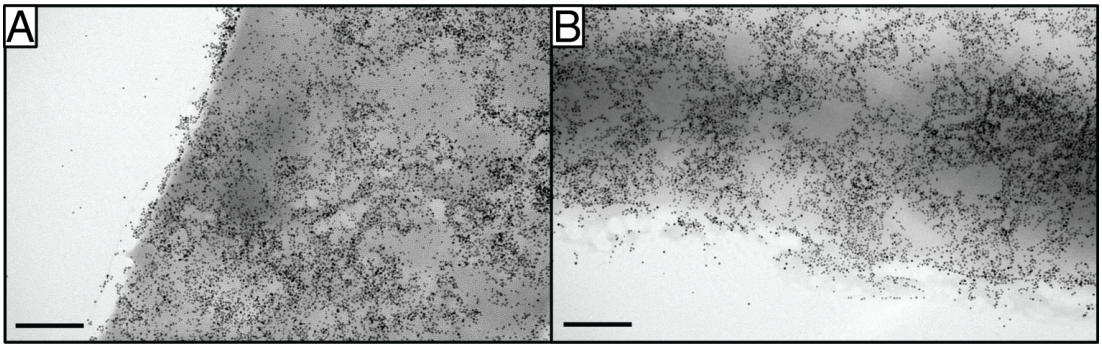

Figure 17: TEM micrograph of trypsin-treated (**A**) *E. coli* and (**B**) *B. subtilis* after 30 min exposure to **NP1**. Particle binding to the surface is apparent, but the clustering effects seen in cells that did not receive proteolytic treatment are markedly absent. Scale bars are 200 nm.

2.3.5 TEM Investigation of the Interaction of 2 nm AuNP Probes with Bacterial Cell Walls

To explore this issue further, we exposed both *B. subtilis* and *E. coli* to 2 nm **NP2**. Under these conditions, most *B. subtilis* cells rupture, while for *E. coli* (Figure 19) time-dependent aggregation via blebbing occurs (Figure 18).

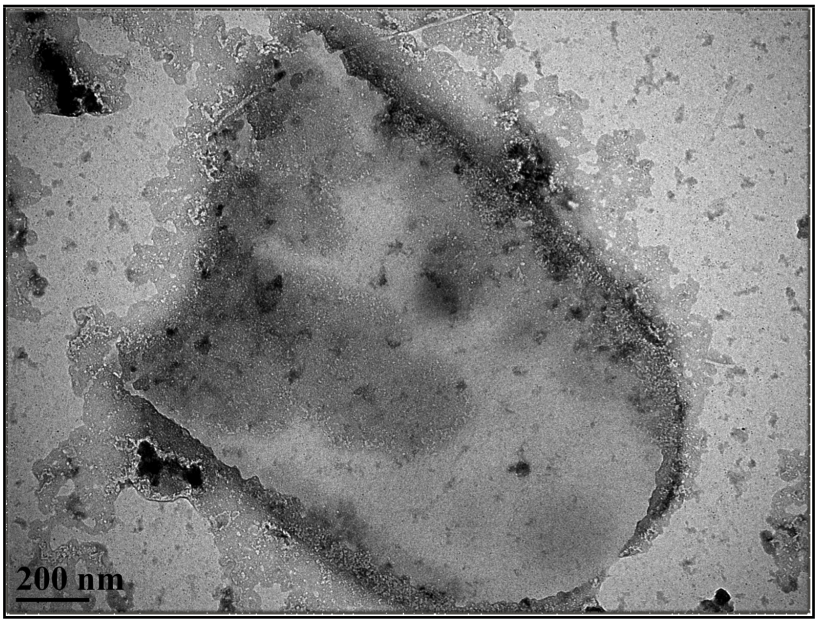

Figure 18: TEM micrograph of a lysed *B. subtilis* following treatment with 2 nm **NP2**.

As seen with **NP1**, **NP2** is initially relatively randomly distributed around the cell membrane of *E. coli* (Figure 19A). After 90 s (Figure 19B), formation of protrusions is visible. Additional **NP2** particles congregate around the already-formed blebs. After 5 min (Figure 19C), the aggregation process appears to have finished, and the bacterial cells are spiked with nanoparticle towers that resemble arrested precursors to the OMVs (outer membrane vesicles) observed in Reference [37].

2.3.6 Investigation of the Cytotxicity of 2 nm NP2 to Gram Positive Bacteria

The rupture of *B. subtilis* in the presence of **NP2** indicates that **NP2** are considerably more toxic than the larger **NP1**. Using a Vybrant cytotoxicity assay

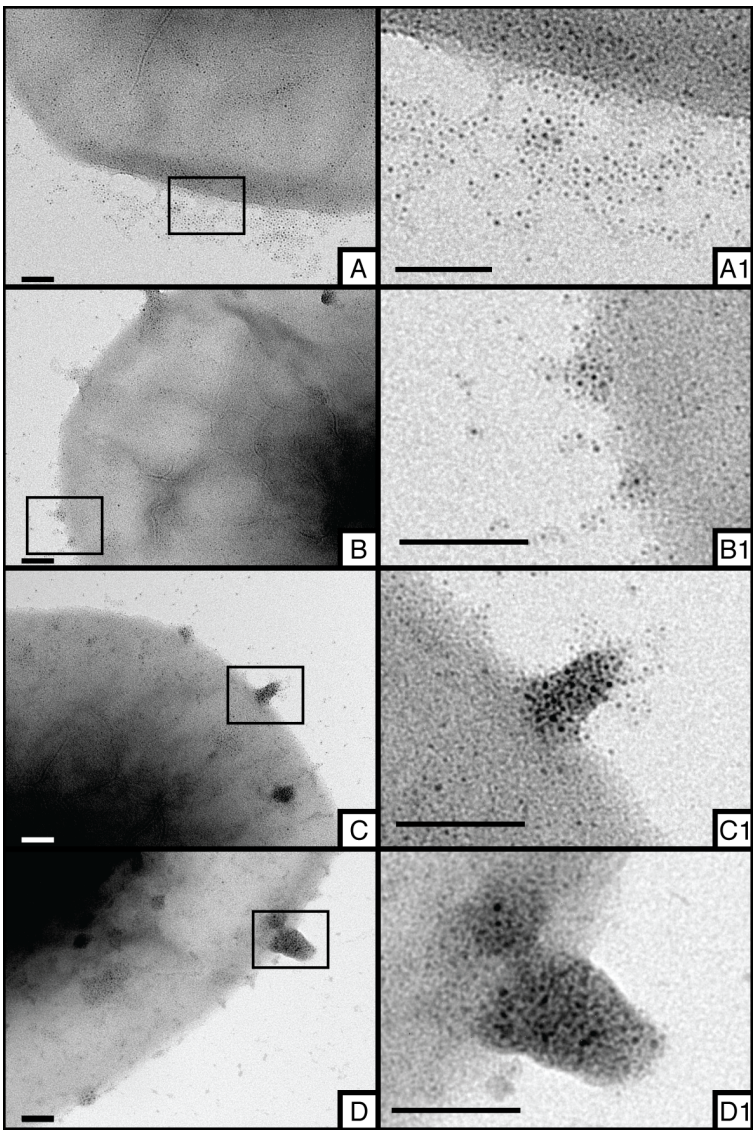

Figure 19: TEM images of various stages of interaction of **NP2** with *E. coli* showing the development of distinct aggregation patterns over time. Corresponding high magnification views of the boxed areas are in the second panel. Times are (**A**) 20 sec, (**B**) 1.5 min, (**C**) 5 min, and (**D**) 17 min. Scale bars are 50 nm.

(See Appendix A), *E. coli* and *B. subtilis* were exposed to **NP2** at various concentrations (100, 200, and 300 nM) followed by the addition of the substrate mixture (G6PD/NADP+/resazurin). Wells containing bacteria and 1X lysis buffer were treated as a positive control (100% membrane damage). The solution mixture was incubated for 5 min at 37 ^{o}C, and the resulting fluorescence from the enzymatic reaction was monitored over time using a fluorescent plate reader.

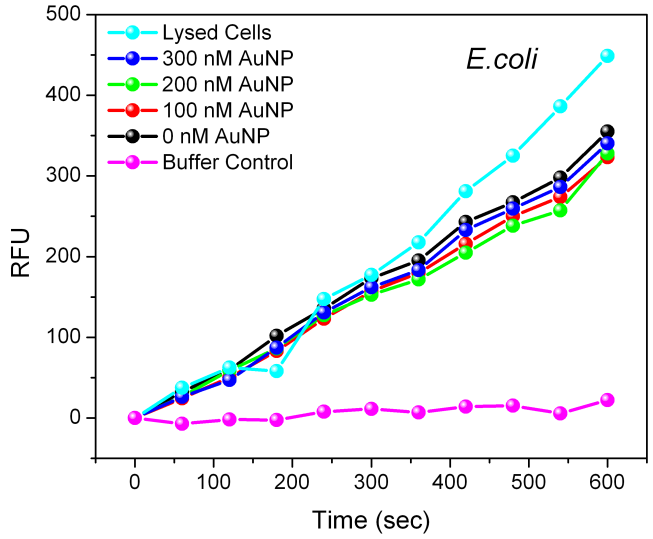

Figure 20: Vybrant Cytotoxicity Assay results over time for *E. coli* treated with increasing concentrations of **NP2**. Fluorescence intensity indicates degree of membrane damage from exposure to **NP2**.

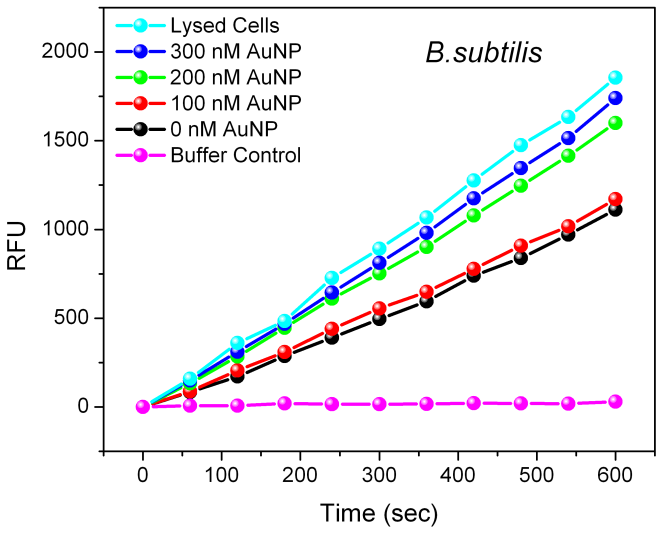

Figure 21: Vybrant Cytotoxicity Assay results over time for *B. subtilis* treated with increasing concentrations of **NP2**. Fluorescence intensity indicates degree of membrane damage from exposure to **NP2**.

Dose-dependent release of G6PD, an indicator of membrane damage, was observed from *B. subtilis*, while *E. coli* showed significantly less release over 5 min

(Figures 20, 21). We calculated the percent of lysed cells based on the positive control for both strains and found that after 5 min, ca. 80% of the *B. subtilis* cells had suffered damage from **NP2**, while only 20% of *E. coli* were affected. These effects are presented in summary in Figure 22.

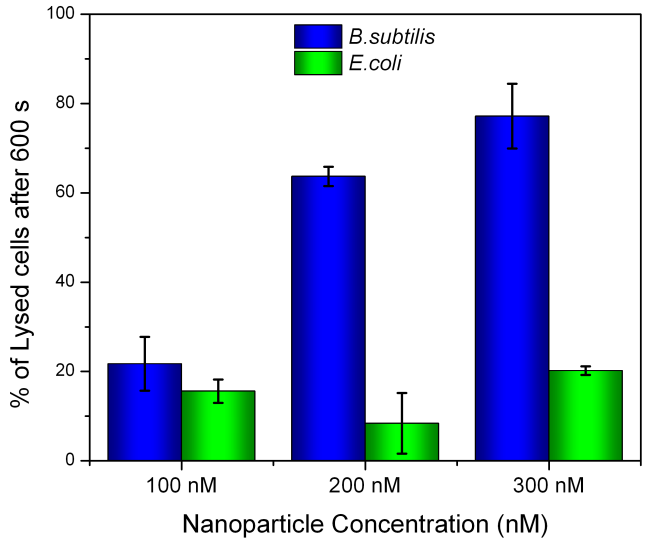

Figure 22: Cell viability of *B. subtilis* (blue) and *E. coli* (green) following 600 sec treatment with 100, 200, and 300 nM **NP2** versus 0 nM control.

This enhanced toxicity to *B. subtilis* for the smaller, 2 nm **NP1** is a surprising juxtaposition to the lack of toxicity of the same particle to *E. coli* as well as the lack of toxicity of the 6 nm **NP2** to *B. subtilis*. Given the high degree of curvature witnessed in the interaction of *E. coli* with **NP2**, it is possible that the increased susceptibility of *B. subtilis* to **NP1** may result from *B. subtilis* having only a single cell membrane, whereas *E. coli* has two. This observation underlines the importance of understanding the macroscopic arrangement of molecular species on cell membranes.

2.4 Concluding Remarks

In summary, hydrophobic, cationic AuNPs develop spatiotemporal aggregation patterns on Gram+ and Gram- bacteria. The patterns depend upon the nature of the

bacterium and the size of the AuNP. In *B. subtilis*, acute toxicity was observed for the 2 nm particles, presumably a product of the high degree of membrane curvature expected from the *E. coli* results coupled with the lack of a secondary cell wall in the Gram-negative *B. subtilis*. The larger, 6 nm particles did not show any toxicity to either bacterial strain but did aggregate onto specific loci on the bacteria.

Timed spectroscopic measurements with 6 nm particles in conjunction with TEM data revealed that the clustering begins as a loose association of particles to the surface and progresses to a state where the particles are organized into stable patches on the cell surface. This effect is more pronounced for *B. subtilis*, indicating the presence of larger local hydrophobic or negatively charged regions on the surface of these cells. Removal of surface proteins via proteolytic treatment led to normalization of the clustering effect for both Gram stain cell types, indicating the significant role of surface proteins in the dynamics of the observed particle clustering process.

The pattern formation might be caused by the NP inducing hydrophobic regions on the cell membrane to coalesce, or by the NP aggregating onto hydrophobic, anionic hotspots already present on the bacteria. Regardless, the results are unexpected and defy the notion that cationic NPs necessarily damage cell walls. Further, there are implications that reach beyond the fundamental modi of interaction between NP and cell wall. Cationic AuNPs might work as effective adjuvants to known antibiotics, as they have been shown to modify the cell surface. The treatment of multidrug-resistant infections might also benefit from surface-binding NPs for related reasons.

Distinct topographic mapping of the bacterial surface by functionalized gold nanoparticles demonstrates the effect of hydrophobicity and local charge on real-time AuNP association on the surface of a living organism. The presence of surface proteins also plays a significant role in the aggregation and ordering processes of AuNPs on bacterial surfaces for both Gram stain types. Experiments with the smaller, hydrophobic **NP1** and Gram-negative *B. subtilis* suggest the role of particle size and

the degree induced membrane deformation in toxicity.

This study has opened a new window to the aggregation pattern of AuNP on cell walls. Other AuNPs may provide access to a variety of different interaction modes. It also might be possible to detect and explain regions of specific biological activity using binding experiments performed during the infection of a eukaryotic cell by a bacterium or during the cell division of bacterial cells.

Ancillary material for this section can be found in Appendix A.

2.5 REFERENCES

[1] Armstrong, J. J., Baddiley, J., Buchanan, J. G., Carss, B., and Greenberg, G. R., "Isolation and structure of ribitol phosphate derivatives (teichoic acids) from bacterial cell walls," *Journal of the Chemical Society*, no. DEC, pp. 4344–4354, 1958. ISI Document Delivery No.: WK681 Times Cited: 180 Cited Reference Count: 54.

[2] Austin, L., Kang, B., Yen, C.-W., and El-Sayed, M., "Plasmonic imaging of human oral cancer cell communities during programmed cell death by nuclear-targeting silver nanoparticles," *Journal of the American Chemical Society*, vol. 133, no. 44473cb0-f94c-af99-0260-2dce2019b484, pp. 17594–17601, 2011. 10.1021/ja207807t.

[3] Baddiley, J., "Bacterial-cell walls and membranes - discovery of the teichoic-acids," *Bioessays*, vol. 10, no. 6, pp. 207–210, 1989. ISI Document Delivery No.: AC128 Times Cited: 14 Cited Reference Count: 27.

[4] Berry, V., Gole, A., Kundu, S., Murphy, C. J., and Saraf, R. F., "Deposition of ctab-terminated nanorods on bacteria to form highly conducting hybrid systems," *Journal of the American Chemical Society*, vol. 127, no. 50, pp. 17600–17601, 2005. ISI Document Delivery No.: 994CW Times Cited: 18 Cited Reference Count: 16.

[5] Bos, M. P., Robert, V., and Tommassen, J., "Biogenesis of the gram-negative bacterial outer membrane," *Annual Review of Microbiology*, vol. 61, pp. 191–214, 2007. ISI Document Delivery No.: 231RB Times Cited: 60 Cited Reference Count: 113 Bos, Martine P. Robert, Viviane Tommassen, Jan.

[6] Bresee, J., Maier, K., Boncella, A., Melander, C., and Feldheim, D., "Growth inhibition of staphylococcus aureus by mixed monolayer gold nanoparticles," *Small*, vol. 7, no. 14, pp. 2027–2031, 2011.

[7] Brust, M., Walker, M., Bethell, D., Schiffrin, D. J., and Whyman, R., "Synthesis of thiol-derivatized gold nanoparticles in a 2-phase liquid-liquid system," *Journal of the Chemical Society-Chemical Communications*, no. 7, pp. 801–802, 1994.

[8] Daniel, M.-C. and Astruc, D., "Gold nanoparticles: assembly, supramolecular chemistry, quantum-size-related properties, and applications toward biology, catalysis, and nanotechnology," *Chemical Reviews*, vol. 104, no. a213219e-00c4-fad2-5f23-8c11dc845d91, pp. 293–639, 2004. 10.1021/cr030698+.

[9] Dickson, J. S. and Koohmaraie, M., "Cell surface charge characteristics and their relationship to bacterial attachment to meat surfaces," *Applied and environmental microbiology*, vol. 55, no. 4, pp. 832–6, 1989.

[10] Duong, F., Eichler, J., Price, A., Leonard, M. R., and Wickner, W., "Biogenesis of the gram-negative bacterial envelope," *Cell*, vol. 91, no. 5, pp. 567–573, 1997. ISI Document Delivery No.: YH960 Times Cited: 108 Cited Reference Count: 84.

[11] Fackler, O. T. and Grosse, R., "Cell motility through plasma membrane blebbing," *Journal of Cell Biology*, vol. 181, no. 6, pp. 879–884, 2008. Fackler, Oliver T. Grosse, Robert.

[12] Gao, X. H., Cui, Y. Y., Levenson, R. M., Chung, L. W. K., and Nie, S. M., "In vivo cancer targeting and imaging with semiconductor quantum dots," *Nature Biotechnology*, vol. 22, no. 8, pp. 969–976, 2004. ISI Document Delivery

No.: 842YB Times Cited: 1553 Cited Reference Count: 56 Gao, XH Cui, YY Levenson, RM Chung, LWK Nie, SM Nature publishing group New york.

[13] Hao, E., Schatz, G. C., and Hupp, J. T., "Synthesis and optical properties of anisotropic metal nanoparticles," *Journal of Fluorescence*, vol. 14, no. 4, pp. 331–341, 2004.

[14] Hayden, S., Zhao, G., Saha, K., Phillips, R., Li, X., Miranda, O., Rotello, V., El-Sayed, M., Schmidt-Krey, I., and Bunz, U., "Aggregation and interaction of cationic nanoparticles on bacterial surfaces," *Journal of the American Chemical Society*, vol. 134, no. 16, pp. 6920–6923, 2012.

[15] He, Y., Yuan, J., Su, F., Xing, X., and Shi, G., "Bacillus subtilis assisted assembly of gold nanoparticles into long conductive nodous ribbons," *The Journal of Physical Chemistry B*, vol. 110, no. 36, pp. 17813–17818, 2006.

[16] Hostetler, M. J., Templeton, A. C., and Murray, R. W., "Dynamics of place-exchange reactions on monolayer-protected gold cluster molecules," *Langmuir*, vol. 15, no. 11, pp. 3782–3789, 1999. ISI Document Delivery No.: 201RY Times Cited: 371 Cited Reference Count: 36 Amer chemical soc Washington.

[17] Huttner, W. B. and Zimmerberg, J., "Implications of lipid microdomains for membrane curvature, budding and fission: Commentary," *Current Opinion in Cell Biology*, vol. 13, no. 4, pp. 478–484, 2001.

[18] Jain, P. K., Huang, W. Y., and El-Sayed, M. A., "On the universal scaling behavior of the distance decay of plasmon coupling in metal nanoparticle pairs: A plasmon ruler equation," *Nano Letters*, vol. 7, no. 7, pp. 2080–2088, 2007. ISI Document Delivery No.: 188NK Times Cited: 60 Cited Reference Count: 60 Jain, Prashant K. Huang, Wenyu El-Sayed, Mostafa A.

[19] Jain, P. K. and El-Sayed, M. A., "Surface plasmon coupling and its universal size scaling in metal nanostructures of complex geometry: Elongated particle pairs and nanosphere trimers," *The Journal of Physical Chemistry C*, vol. 112, no. 13, pp. 4954–4960, 2008. doi: 10.1021/jp7120356.

[20] Kahraman, M., Zamaleeva, A., Fakhrullin, R., and Culha, M., "Layer-by-layer coating of bacteria with noble metal nanoparticles for surface-enhanced raman scattering," *Analytical and Bioanalytical Chemistry*, vol. 395, no. 8, pp. 2559–2567, 2009.

[21] Leroueil, P., Berry, S., Duthie, K., Han, G., Rotello, V., McNerny, D., Baker Jr, J., Orr, B., and Holl, M., "Wide varieties of cationic nanoparticles induce defects in supported lipid bilayers," *Nano Letters*, vol. 8, no. 2, pp. 420–424, 2008.

[22] Leroueil, P., Hong, S., Mecke, A., Baker Jr, J., Orr, B., and Banaszak Holl, M., "Nanoparticle interaction with biological membranes: does nanotechnology present a janus face?," *Accounts of Chemical Research*, vol. 40, no. 5, pp. 335–342, 2007.

[23] McMahon, H. T. and Gallop, J. L., "Membrane curvature and mechanisms of dynamic cell membrane remodelling," *Nature*, vol. 438, no. 7068, pp. 590–596, 2005. McMahon, HT Gallop, JL.

[24] Parton, R. G. and Simons, K., "The multiple faces of caveolae," *Nature Reviews Molecular Cell Biology*, vol. 8, no. 3, pp. 185–194, 2007. Parton, Robert G. Simons, Kai.

[25] Phillips, R. L., Miranda, O. R., You, C. C., Rotello, V. M., and Bunz, U. H. F., "Rapid and efficient identification of bacteria using gold-nanoparticle - poly(para-phenyleneethynylene) constructs," *Angewandte Chemie-International*

Edition, vol. 47, no. 14, pp. 2590–2594, 2008. Phillips, Ronnie L. Miranda, Oscar R. You, Chang-Cheng Rotello, Vincent M. Bunz, Uwe H. F.

[26] Rosi, N. and Mirkin, C., "Nanostructures in biodiagnostics," 2005.

[27] Schekman, R. and Orci, L., "Coat proteins and vesicle budding," *Science*, vol. 271, no. 5255, pp. 1526–1533, 1996.

[28] Scott, J. and Barnett, T., "Surface proteins of gram-positive bacteria and how they get there," *Annual Review of Microbiology*, vol. 60, pp. 397–423, 2006.

[29] Stachowiak, J. C., Hayden, C. C., and Sasaki, D. Y., "Steric confinement of proteins on lipid membranes can drive curvature and tubulation," *Proceedings of the National Academy of Sciences of the United States of America*, vol. 107, no. 17, pp. 7781–7786, 2010. Stachowiak, Jeanne C. Hayden, Carl C. Sasaki, Darryl Y.

[30] Storhoff, J. and Mirkin, C., "Programmed materials synthesis with dna," *ChemInform*, vol. 30, no. 39, pp. no–no, 1999.

[31] Subtil, A., Gaidarov, I., Kobylarz, K., Lampson, M. A., Keen, J. H., and McGraw, T. E., "Acute cholesterol depletion inhibits clathrin-coated pit budding," *Proceedings of the National Academy of Sciences of the United States of America*, vol. 96, no. 12, pp. 6775–6780, 1999. Subtil, A Gaidarov, I Kobylarz, K Lampson, MA Keen, JH McGraw, TE.

[32] Sutcliffe, I. C., "The lipoteichoic acids and lipoglycans of gram-positive bacteria - a chemotaxonomic perspective," *Systematic and Applied Microbiology*, vol. 17, no. 4, pp. 467–480, 1995. ISI Document Delivery No.: QL322 Times Cited: 0 Cited Reference Count: 135.

[33] Tabor, C., Murali, R., Mahmoud, M., and El-Sayed, M. A., "On the use of plasmonic nanoparticle pairs as a plasmon ruler: The dependence of the near-field dipole plasmon coupling on nanoparticle size and shape," *Journal of Physical Chemistry A*, vol. 113, no. 10, pp. 1946–1953, 2009. Times Cited: 0.

[34] Teranishi, T., Hasegawa, S., Shimizu, T., and Miyake, M., "Heat-induced size evolution of gold nanoparticles in the solid state," *Advanced Materials*, vol. 13, no. 22, pp. 1699–1701, 2001. ISI Document Delivery No.: 494HY Times Cited: 115 Cited Reference Count: 22 Wiley-v c h verlag gmbh Berlin.

[35] Wender, P. A., Mitchell, D. J., Pattabiraman, K., Pelkey, E. T., Steinman, L., and Rothbard, J. B., "The design, synthesis, and evaluation of molecules that enable or enhance cellular uptake: Peptoid molecular transporters," *Proceedings of the National Academy of Sciences of the United States of America*, vol. 97, no. 24, pp. 13003–13008, 2000. ISI Document Delivery No.: 376UZ Times Cited: 645 Cited Reference Count: 46 Wender, PA Mitchell, DJ Pattabiraman, K Pelkey, ET Steinman, L Rothbard, JB Natl acad sciences Washington.

[36] Zhang, D. Q., Li, G. S., and Yu, J. C., "Inorganic materials for photocatalytic water disinfection," *Journal of Materials Chemistry*, vol. 20, no. 22, pp. 4529–4536, 2010. ISI Document Delivery No.: 601GJ Times Cited: 0 Cited Reference Count: 120 Zhang, Dieqing Li, Guisheng Yu, Jimmy C. Royal soc chemistry Cambridge.

[37] Zhao, Y., Tian, Y., Cui, Y., Liu, W., Ma, W., and Jiang, X., "Small molecule-capped gold nanoparticles as potent antibacterial agents that target gram-negative bacteria," *Journal of the American Chemical Society*, vol. 132, no. 35, pp. 12349–12356, 2010.

CHAPTER III

SOLAR ENERGY CONVERSION: TITANIUM DIOXIDE / SEMICONDUCTING NANOCRYSTAL HYBRID ELECTRODES FOR WASTEWATER TREATMENT

3.1 Chapter Summary

Titanium dioxide nanotubes offer distinct advantages over films of the same material in the production of reactive species from water under irradiation. This can be used for subsequent inactivation of *Escherichia coli* in wastewater. However, the visible light absorption capability of titinium dioxide is limited. Semiconducting nanocrystals of cadmium sulfide have been used to increase the sensitivity of TiO_2 nanotubes to visible light. A small applied potential, using CdS-coated TiO_2 nanotube arrays, allowed for total inactivation of *E. coli* in hitherto record short time. [17]

3.2 Global Energy Concerns of Today and Tomorrow

Secure, clean, sustainable energy is quite possibly the most important scientific challenge facing the world today, as acquisition of energy security has far-reaching repercussions in areas such as national, environmental, and economic security. Further, meeting the projected demands for the mid-21^{st} century will neccessarily involve not only increased efficiency at energy capture and use, but also some incredible advancement in our ability to generate carbon-neutral energy, primarily from sunlight.

3.2.1 The Pressing Need for Carbon-Neutral Energy Sources

Factoring in both the increasing trend of global average energy consumption as well as the decreasing trend in global average energy intensity, a result of improvements

Table 2: Global energy and carbon dioxide emission estimates taken from Reference [19].

	Units	2001	2050	2100
Population	B persons	6.145	9.4	10.4
GDP	T dollars/yr	46	140	284
Per capita GDP	dollars/(person-yr)	7,470	14,850	27,320
Energy intensity	W/(dollars/yr)	0.294	0.20	0.15
Energy consumption rate	TW	13.5	27.6	43.0
Carbon intensity	KgC/(W•yr)	0.49	0.40	0.31
Carbon emission rate	GtC/yr	6.57	11.0	13.3
Equivalent CO_2 emission rate	$GtCO_2$/yr	24.07	40.3	48.8

in technology throughout the energy production, distribution, and end-use chain, the world energy consumption rate is projected to double by 2050 and to triple by 2100 (Table 2). [19] And, though there is argument concerning the amount of fossil fuel reserves that remain on Earth, the use of these fuels is expected to inject an increasing amount of CO_2 into the environment. Indeed, even factoring in the relative decline in carbon emissions rate versus total energy consumption as we move away from high-carbon energy souces such as coal and toward low-carbon energy sources such as natural gas, the world carbon emission rate is expected to increase from 6.6 (2001) to 11.0 billion metric tons of carbon per year. [24]

While CO_2 concentration in the environment does not necessarily determine the global average temperature, it is known to have been highly correlated with temperature swings over the past 650,000 years that have caused ice ages on the planet. [26] During this 650,000 year time period, atmospheric CO_2 concentration has only fluctuated between 210 and 300 ppm. [26] In the past 50 years, CO_2 concentration has risen to an excess of 380 ppm. If left unchecked, this value could double the level of preanthropogenic CO_2 during the 21^{st} century. Various models have been used to predict the impact of this relatively rapid change in CO_2 concentration on the

environment, and their outcomes range from moderately disastrous to the end of life on Earth. [26]

Given these projections, the development of carbon-neutral energy sources becomes increasingly critical. Three general methods exist to produce such large amounts of carbon-neutral power: nuclear fission, carbon capture and storage, and renewable energy. [19] Nuclear fission would exhaust the available terrestrial uranium resouces in less than thirty years in addition to requiring construction of a full nuclear power plant every 1.6 days to meet the projected energy demands. [12] For the second option, carbon capture and storage, to be viable, carbon would have to be sequestered reliably in underground aquefiers with a leak rate of less than 1% over the course of 500-1000 years in order to keep the emitted flux less than that intended to be initially mitigated. [23] To determine if this is even viable, at-scale experiments are needed with extensive accompanying modeling, simulation, monitoring, and validation. [19]

The third choice becomes the most obviously valid, as renewable energy sources abound. And, while wind, water, and geothermal sources have their own specific drawbacks including regional availability and local environmental impacts, these will remain useful energy sources in some regions of the world. However, of the various renewable energy sources, solar energy dwarfs its competition in potential utility. This derives from the fact that sunlight is not only available on virtually all parts of the planet but also from the fact that more energy from the sun strikes the earth in 1 hour than is currently consumed in one year by the entire planet. [15]

3.3 Titanium Dioxide as a Photocatalyst

Since the 1960s, titanium dioxide (TiO_2) has been the focus of much research in the area of photoelectrochemical solar energy conversion. TiO_2 is an excellent material for photocatalysis, a fact that derives from several of its properties: it is inexpensive, has excellent chemical stability, and its photogenerated holes are highly oxidixing

(+2.53 V). [14] These holes react with water to produce hydroxyl radicals ($OH^{\bullet}$), which can propogate through solution with only slightly decreased redox potential. Its electrons have a redox potential of ca. -0.52 V, which would be negative enough to generate hydrogen from water in the absence of electron trapping. However, even with the posibility - and relative prevalance - of trapping, a significant number are able to reduce molecular oxygen to superoxide (O_2^-) or hydrogen peroxide (H_2O_2). All of these reactive species are important to the use of TiO_2 that we present here, though the redox power and prevalence of the $OH^{\bullet}$ radical make it perhaps the most important of these species. Three important reactions that take place on TiO_2 are given in equations 5, 6, and 7.

$$2H_2O + 4h^+ \rightarrow O_2 + 4H^+ \tag{5}$$

$$O_2 + 2H^+ + 2e^- \rightarrow H_2O_2 \tag{6}$$

$$H_2O + h^+ \rightarrow OH^{\bullet} + H^+ \tag{7}$$

These reactions are useful for a plethora of side-applications, including the utilization of sunlight and titanium dioxide for the inactivation of bacteria in secondary wastewater effluents.

3.4 Worldwide Wastewater Use and Corresponding Health Concerns

With the rising human population and consequent urbanization and crowding of cities, the world today faces increasing scarcity of good quality water resources. This has led to an accelerating upward trend in the use of wastewater, excreta, and greywater[1] for

[1]Greywater: Wastewater generated brom domextic activities such as laundry, dishwashing, or bathing. Does not contain human waste.

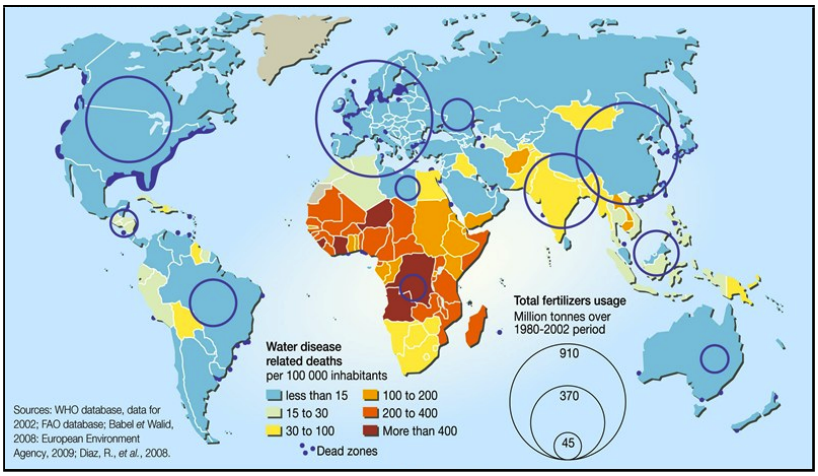

Figure 23: Water disease related deaths by country, adapted from the WHO report *Annual Assesment of Sanitization and Drinking Water*. [25]

agriculture and aquaculture. [25] Human health bears the burden. Diarrhoeal disease alone leads to the deaths of 1.8 million people every year, accounting for 4.1 % of the global disease burden. Over 88 % of this burden can be attributed to unsafe water supply, sanitation, and hygiene, and it is mostly concentrated in children in developing countries (Figure 23). [25]

Over 1 billion people worldwide lack access to safe drinking water. This fact leads to millions of deaths annually: of all child deaths annually, 18% are directly attributable to unsafe drinking water, and of the 35% that can be attributed to malnutrition, half of those malnutrition cases are themselves a result of unsafe drinking water. [25] Additionally, many cancers, tooth/skeletal damage, cholera, and parasitic infections (e.g. schistosomiasis[2]) lower quality of life in individuals without access to proper sanitization and a safe water supply.

Treating this problem on a global scale will require access to cheap, reusable technologies capable of decontaminating water effluent. The affordability and catalytic properties of titanium dioxide and the availability of sunlight around the globe make

[2]On contact with humans, the parasite burrows into the skin, matures into another stage (schistosomula), then migrates to the lungs and liver, where it matures into the adult form. The adult worm then migrates to its preferred body part, depending on its species. These areas include the bladder, rectum, intestines, liver, portal venous system, spleen, and lungs. [10]

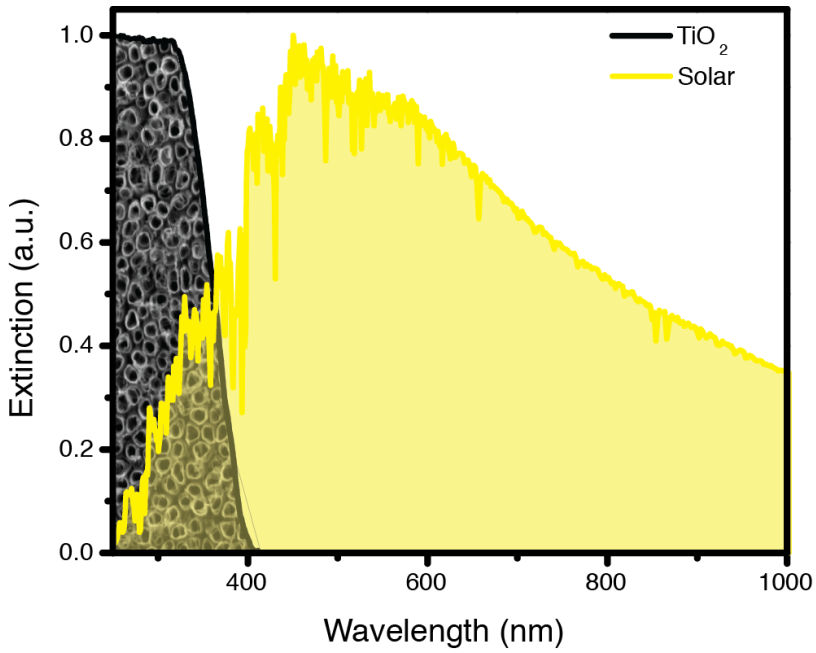

Figure 24: Extinction spectrum of titanium dioxide (grey) showing overlap with the solar spectrum (yellow). TiO_2 has poor light absorption capabilities in the visible, which comprises the bulk of the solar spectrum.

the combination of these two quite attractive for wastewater treatment. However, TiO_2 displays limited absorption of visible light, which comprises the bulk of the solar spectrum (Figure 24). To this end, we considered a method to enhance the visible light-harvesting capability of titanium dioxide in order to more efficiently inactivate harmful bacteria using sunlight.

3.5 Use of Titanium Dioxide in the Photoelectrochemical Inactivation of Bacteria in Wastewater

Escherichia coli is a Gram-negative bacterium that is well known for its toxicity to humans, being the cause of afflictions ranging from inflammations and peritonitis to food poisoning and urinary infections. [20] This toxicity has led to the development of many strategies to disinfect various media of these organisms, [11] and although many semiconducting materials are being tested, titanium dioxide is still among the most efficient and widely used catalysts in the disinfection of *E. coli*. [22] Hydroxyl radicals

are potent inactivators of bacteria, as they rapidly decimate the organic components of cells. [22] However, two barriers limit the use of TiO_2 for photocatalytic inactivation of bacteria using sunlight: its relatively low efficiency of sunlight utilization due to its wide bandgap (3.0 - 3.2 eV) and its poor charge-transfer properties. [22]

3.5.1 TiO_2 Nanotube Arrays

To avoid the need of recuperating TiO_2 particles from water post-use, researchers have turned to methods of immobilization of TiO_2 particles, such as thin films. These suffer from poor charge transfer, leading to a high rate of electron-hole recombination. Baram et al. [8] have very recently reported a great enhancement in the inactivation of *E. coli* using immobilized, anodically fabricated TiO_2 nanotube (NT) arrays[1, 6, 2] in a photocatalytic cell. The aligned porosity, crystallinity, and oriented nature of these arrays make them attractive electron percolation pathways for vectorial charge transfer between interfaces. [4, 5, 3] Through the use of NT arrays, Baram et al. achieved an inactivation interval of less than 10 min using 25 cm^2 surface area NT arrays, a UV light source, and an applied bias of 3-5 V_{SEC} for bacterial solutions with a concentration on the order of 10^6 CFU/mL *E. coli*. [8] These results are quite promising for the use of NTs in water treatment; however, the system is still limited by the weak visible light absorption capability of the TiO_2 NTs.

3.5.2 Limited Solar Light Absorption of TiO_2

More efficient visible light utilization would render this system quite attractive for disinfection procedures with sunlight as the energy source. Recent and very active research relates to the anchoring of small-bandgap nanocrystals to wide-bandgap semi-conducting metal oxides, rendering these oxides sensitive to visible light. [9, 21] Of particular interest are CdS nanocrystals, which have a relatively small bandgap and thus are capable of harvesting photons in the visible and near-infrared regions. [7]

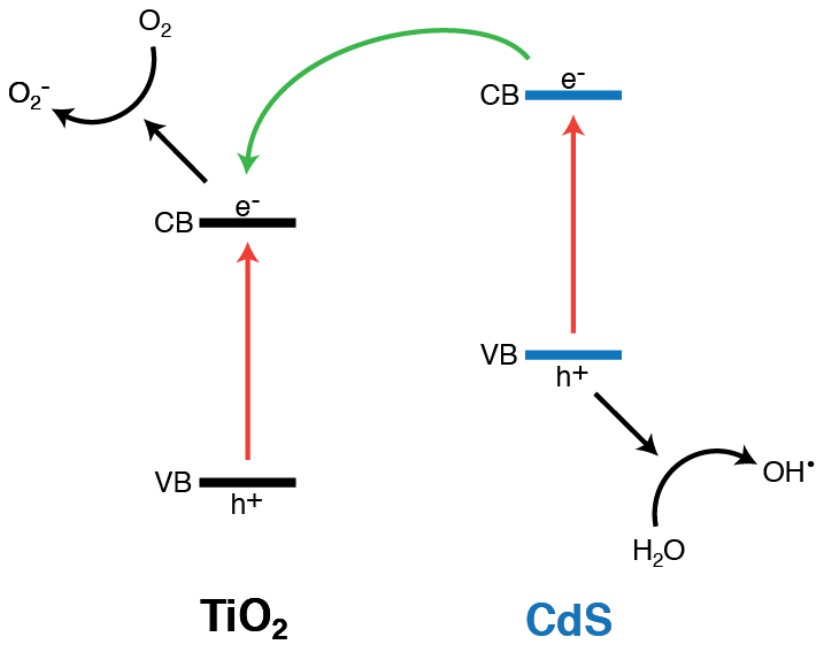

Figure 25: Band-gap diagram for titanium dioxide coupled to cadmium sulfide. Illustrates how CdS helps TiO_2 to harvest energy outside the region over which it normally absorbs.

The use of CdS is shown to enhance the charge carrier separation process[7] and consequently is expected to enhance the inactivation efficiency of *E. coli* in wastewater (Figure 25). In this regard, a complex system (Pt/CdS/TiO_2) was investigated, [18] but this system suffers from the drawbacks of higher cost (from Pt) and poor charge transfer as a result of its multijunction nature and the high level of CdS coverage, which is shown in this work to adversely affect the inactivation efficiency of *E. coli*. In the present work, we explored the capabilities of a simpler system, TiO_2/CdS hybrid electrodes for the disinfection of water contaminated by *E. coli*. Using this hybrid system, total inactivation of *E. coli* was achieved in less than 3 min using a small chip (1 cm^2), a relatively small applied bias (0.5 V), and a white, CW (xenon) light source.

Two sets of experiments were performed to explore the efficiency of our material to inactivate *E. coli*: photochemical (light only) and photoelectrochemical (light and applied bias). For the sake of comparison, three types of semiconductor electrodes

were used in each experiment: TiO_2 thin films, TiO_2 NT arrays, and TiO_2 NT/CdS hybrid arrays.

3.5.3 Electrode Characterization

Figure 30 shows the diffuse reflectance spectroscopy (DRS) UV-vis spectra of the three electrodes. Note that the absorption edge of the hybrid electrode is shifted bathochromically (ca. 570 nm) from that of the TiO_2 thin film and NT (ca. 300 nm). Given equation 8 (from Reference [9]),

$$\lambda(nm) = \frac{1240}{E}(eV), \tag{8}$$

the estimated bandgap of the hybrid electrode is 2.17 eV, indicating the ability of the hybrid array to harvest visible light.

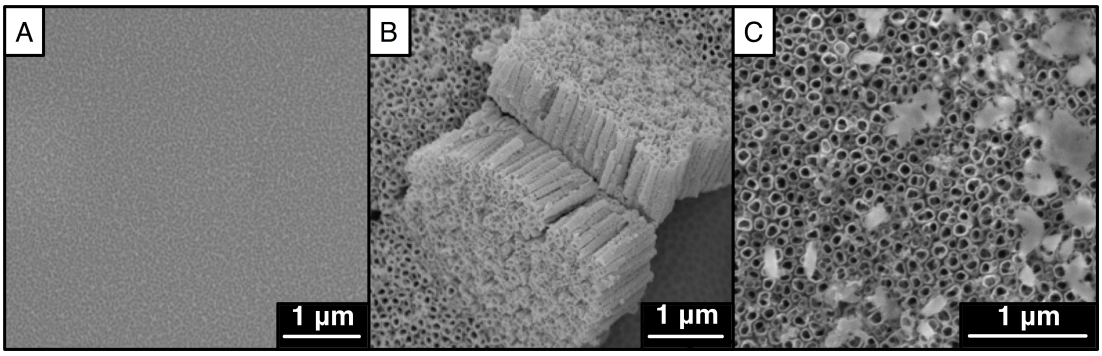

Figure 26: FESEM images of TiO_2 thin film (A), a titanium dioxide nanotube array (B), and a TiO_2 nanotube/CdS hybrid electrode.

Figure 26 shows scanning electron microscopy (SEM) images of the three electrodes used in this study. It can be seen that the oxide film is homogeneous and covers the entire surface (Figure 26A). In the cross-sectional view of the NT arrays (Figure 26B), the tubular structure is evident, with nearly uniform wall thicknesses and NT lengths (1.0 ± 0.1 μm). The FESEM of the hybrid electrode shows crystallites of CdS scattered on the NT surface (Figure 26C). X-ray photoelectron spectroscopy (XPS) analyses confirm the composition of the three electrodes (Figure 27).

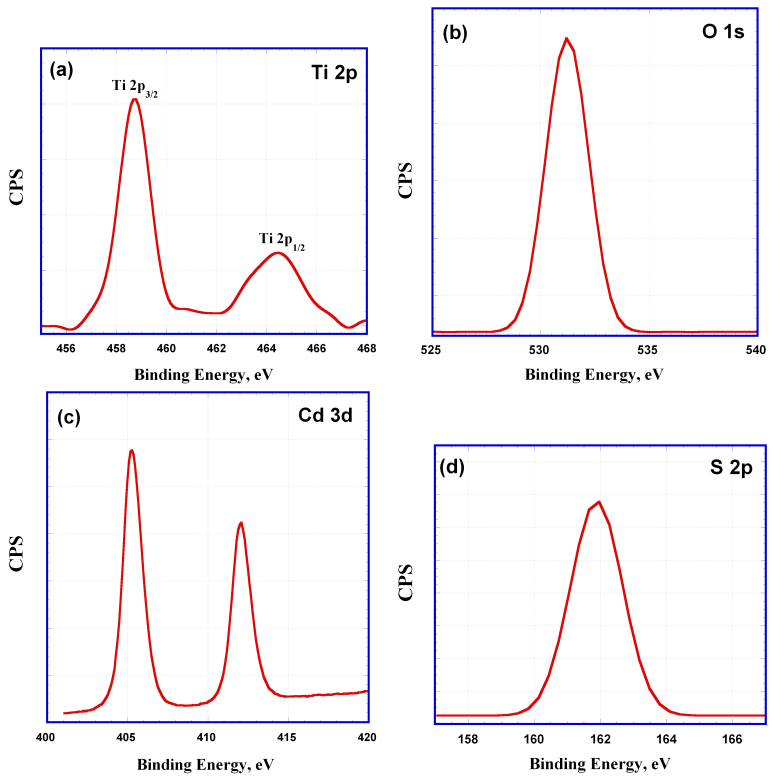

Figure 27: XPS spectra of CdS/TiO_2 nanotube hybrid electrode

The formation of titanium dioxide is evident from the O 1s and Ti 2p peaks, with a Ti/O molar ratio close to the stoichiometric proportion (Figure 27). Note that both Ti peaks, $2p_{3/2}$ and $2p_{1/2}$, are observed with a spin-orbit splitting of 5.7 eV, confirming that both signals correspond to Ti^{4+}. [6] Peaks for Cd and S were also detected for the hybrid electrode.

3.5.4 Photochemical and Photoelectrochemical Inactivation of Bacteria

In the photochemical study, electrodes were immersed in separate solutions containing *E. coli* in sulfate buffer (200 mL, 10^7 cfu *E. coli*, 1.4 mM Na_2SO_4) under stirring and illumination from a xenon lamp (150 mW/cm^2), with a water filter to block the IR, and samples were collected every 10 min, then diluted, plated, and cultured via the traditional plating and culturing method. Colonies were counted, and then dilution factor was used to back-calculate the bacteria concentration at each timpoint. Full experimental details can be found in Appendix B. *E. coli* inactivation with the same

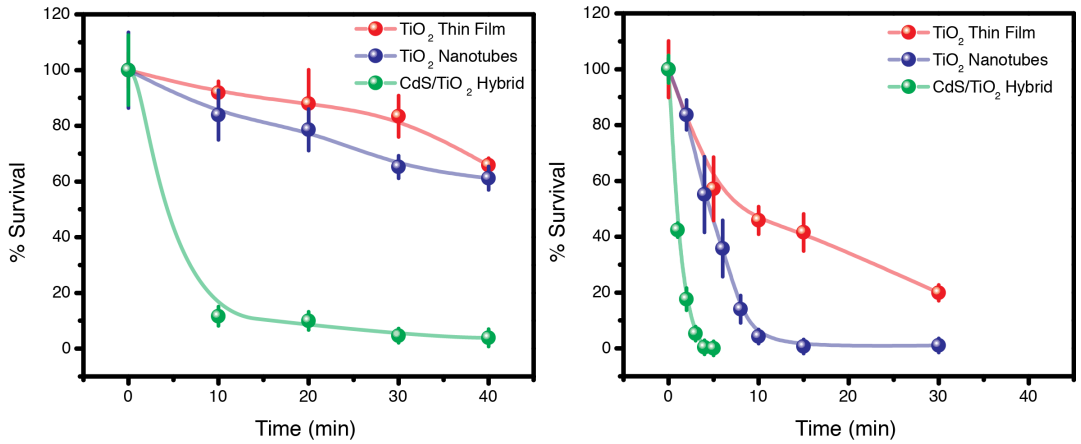

Figure 28: Percent survivability for *E. coli* treated via the photochemical (left) and photoelectrochemical (right) methods with TiO_2 thin film (red), TiO_2 nanotubes (green), and TiO_2/CdS hybrid electrodes (blue).

set-up was measured without any illumination and found to be negligible. For the photoelectrochemical study, a two-electrode electrochemical cell (35 mL, Figure 30) was used with the semiconductor material as the working electrode and Pt foil as the counter electrode under a constant applied potential of 0.5 V and illumination from a xenon lamp (150 mW/cm^2). Samples were collected every 10 min for the thin film, every 5 min for the NT array, and every 1 min for the CdS-coated NT arrays.

Figure 28 (left) shows the results obtained from the photochemical experiment; use of the hybrid electrode led to an almost complete inactivation of *E. coli* in only 10 min without any applied bias. Meanwhile, the use of both the thin film and the pure NT array led to the inactivation of only 40% and 45% of the bacteria, respectively, even after 40 min exposure under the xenon lamp. The enhanced charge transfer and light absorption capability of the hybrid electrode render it more efficient and account for the observed increase in the inactivation rate of *E. coli* as compared to the thin film and the pure NT electrodes.

Figure 28 (right) shows the inactivation of *E. coli* in the photoelectrochemical experiment under 0.5 V applied bias, to help separate the charge carriers. It is evident that the use of the TiO_2/CdS hybrid electrode resulted in the inactivation of

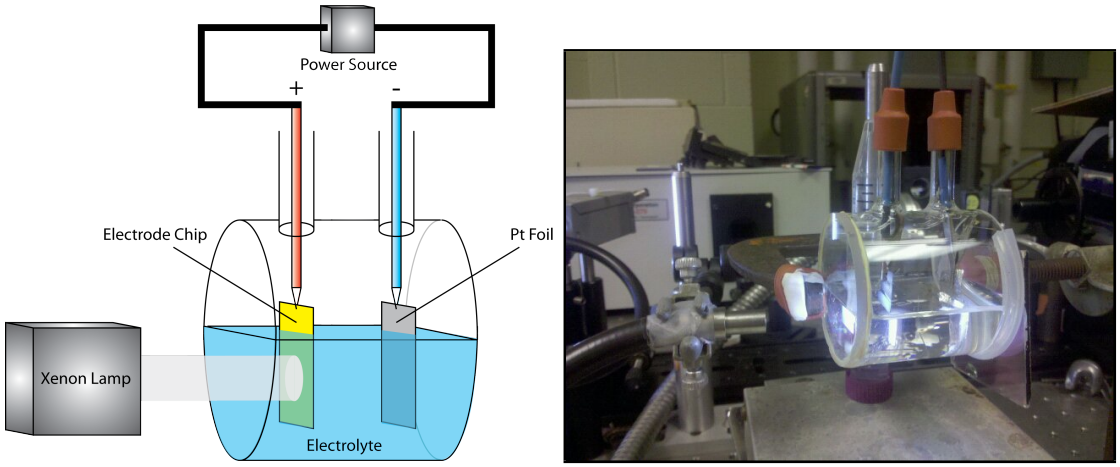

Figure 29: Schematic and photograph of the photoelectrochemical setup used for bacterial inactivation with TiO_2. The photochemical set up employed the same constituents, but no bias was placed across the electrodes.

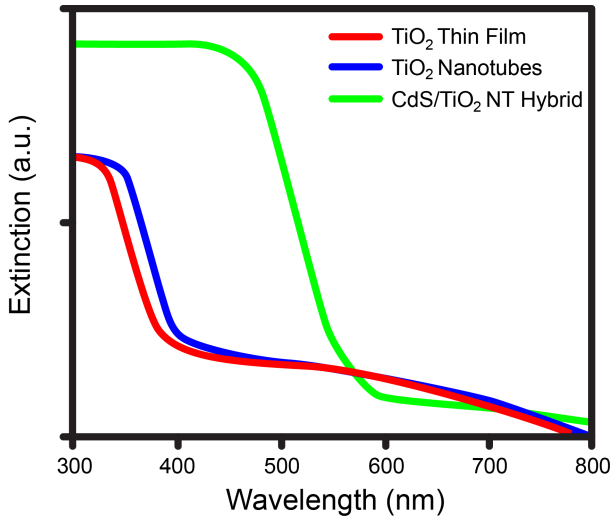

Figure 30: Diffuse reflectance spectroscopy UV-vis spectra of TiO_2 thin film (red), TiO_2 nanotubes (blue), and CdS/TiO_2 nanotube hybrid (green) electrodes.

the *E. coli* in only 3 min (Figure 31).

To quantify the kinetics of the inactivation process, we used the Chick model [13] to estimate the inactivation rate constants (Table 3). Our estimated rate constants for the TiO_2 NTs and thin films are in very good agreement with those reported by Baram et al., [8] provided that lamp intensity, chip area, and current discrepancies are taken into consideration. However, our hybrid electrode showed marked inactivation rate improvements: a 1928% improvement over the thin-film electrodes and a 396%

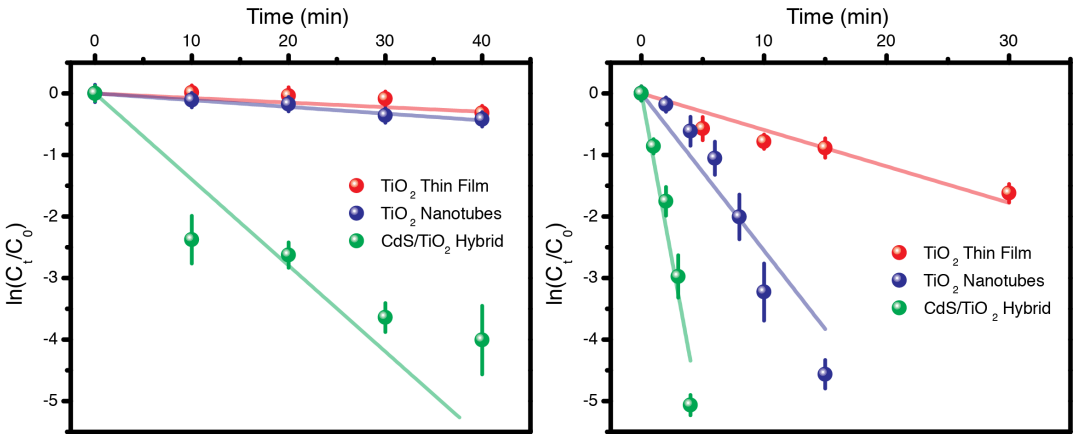

Figure 31: Inactivation rates for *E. coli* treated via the photochemical (left) and photoelectrochemical (right) methods with TiO_2 thin film (red), TiO_2 nanotubes (green), and CdS/TiO_2 nanotube hybrid electrodes (blue).

Table 3: Inactivation rates of *E. coli* under photochemical and photoelectrochemical conditions using TiO_2 thin film, TiO_2 nanotubes, and CdS/TiO_2 nanotube hybrid electrodes

	Photochemical (min^{-1})	Photoelectrochemical (min^{-1})
Thin Film TiO_2	0.0093	0.0581
TiO_2 Nanotubes	0.0122	0.283
TiO_2 Nanotube/CdS Hybrid	0.0833	1.12

improvement over the inactivation rate displayed by the pure NT arrays (Figure 31, right).

We observed a relationship between the degree of CdS coverage of the NT array surface and the inactivation efficiency. When CdS was made to cover the entire surface completely (more than three layers), the chips displayed little to no inactivation ability. This is in agreement with Guijarro et al., [16] who reported a severe drop in the incident photon-to-electron conversion efficiency (IPCE) of their solar cell device when their TiO_2 surface was completely blocked from solvent contact by CdSe. The need for a sparse coverage of nanocrystals on the NT surface is both economically and environmentally promising for the use of these types of systems in water treatment

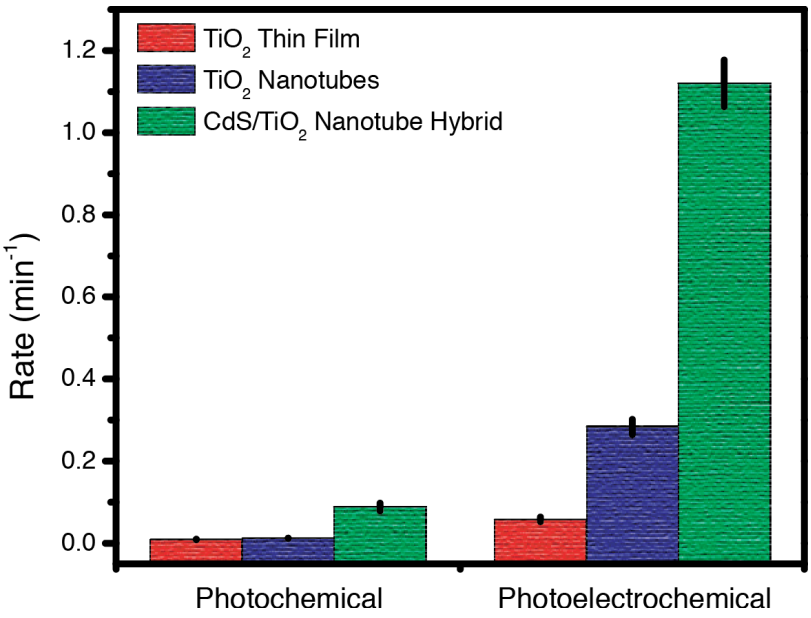

Figure 32: Inactivation rate summary for both photochemical and photoelectrochemical experiments using titanium dioxide thin film (red), titanium dioxide nanotubes (green), and CdS/titanium dioxide nanotube hybrid (blue) electrodes.

procedures.

3.6 Concluding Remarks

We documented the inactivation of *E. coli* in aqueous media at a previously unattainable rate using CdS to bridge the bandgap discrepancy and render TiO_2 sensitive to visible light. The rate was shown to be even further improved upon the use of a small applied potential. This work is a step toward realizing more efficient wastewater treatment systems and has possible applications in the field of energy production. Work with other bandgap-bridging materials and with deposition procedures to more precisely control the deposited nanocrystals will further reveal the applicability of these results.

The utility of nanostructures in increasing the light absorption capability of other species is not confined to this system. The following two chapters present variations on this theme: first continuing in the field of solar energy conversion and second in the photodynamic treatment of cancers.

3.7 REFERENCES

[1] ALLAM, N. K. and GRIMES, C. A., "Effect of cathode material on the morphology and photoelectrochemical properties of vertically oriented tio2 nanotube arrays," *Solar Energy Materials and Solar Cells*, vol. 92, no. 11, pp. 1468–1475, 2008. ISI Document Delivery No.: 355DB Times Cited: 9 Cited Reference Count: 37 Allam, Nageh K. Grimes, Craig A. Ford Foundation [DE-FG02-06ER15772] Support of this work by the Department of Energy under Grant DE-FG02-06ER15772 is gratefully acknowledged. Nageh K. Allam gratefully acknowledges support under the IFP fellowship provided by the Ford Foundation. Elsevier science bv Amsterdam.

[2] ALLAM, N. K. and GRIMES, C. A., "Effect of rapid infrared annealing on the photoelectrochemical properties of anodically fabricated tio2 nanotube arrays," *Journal of Physical Chemistry C*, vol. 113, no. 19, pp. 7996–7999, 2009. ISI Document Delivery No.: 443FL Times Cited: 2 Cited Reference Count: 35 Allam, Nageh K. Grimes, Craig A. Department of Energy [DE-FG02-06ER15772] Support of this work by the Department of Energy under Grant DE-FG02-06ER15772 is gratefully acknowledged. Amer chemical soc Washington.

[3] ALLAM, N. K. and GRIMES, C. A., "Room temperature one-step polyol synthesis of anatase tio2 nanotube arrays: Photoelectrochemical properties," *Langmuir*, vol. 25, no. 13, pp. 7234–7240, 2009. ISI Document Delivery No.: 464UR Times Cited: 3 Cited Reference Count: 41 Allam, Nageh K. Grimes, Craig A. Department of Energy [DE-FG36-08GO18O74] Support of this work by the Department of Energy under Grant DE-FG36-08GO18O74 is gratefully acknowledged. Amer chemical soc Washington.

[4] Allam, N. K., Shankar, K., and Grimes, C. A., "A general method for the anodic formation of crystalline metal oxide nanotube arrays without the use of thermal annealing," *Advanced Materials*, vol. 20, no. 20, pp. 3942–+, 2008. ISI Document Delivery No.: 369QM Times Cited: 16 Cited Reference Count: 29 Allam, Nageh K. Shankar, Karthik Grimes, Craig A. Department of Energy [DE-FG02-06ER15772]; Ford Foundation Support of this work by the Department of Energy under grant DE-FG02-06ER15772 is gratefully acknowledged. Nageh K. Allam gratefully acknowledges support under the IFP fellowship provided by the Ford Foundation. We thank Dr. Joe Kulik of the Penn State Materials Research Institute for help with the TEM analysis, and the referees for their helpful comments. Wiley-v c h verlag gmbh Weinheim.

[5] Allam, N. K., Shankar, K., and Grimes, C. A., "Photoelectrochemical and water photoelectrolysis properties of ordered tio2 nanotubes fabricated by ti anodization in fluoride-free hcl electrolytes," *Journal of Materials Chemistry*, vol. 18, no. 20, pp. 2341–2348, 2008. ISI Document Delivery No.: 307XT Times Cited: 14 Cited Reference Count: 43 Allam, Nageh K. Shankar, Karthik Grimes, Craig A. Royal soc chemistry Cambridge.

[6] Allam, N. K. and El-Sayed, M. A., "Photoelectrochemical water oxidation characteristics of anodically fabricated tio2 nanotube arrays: Structural and optical properties," *The Journal of Physical Chemistry C*, vol. 114, no. 27, pp. 12024–12029, 2010. doi: 10.1021/jp1037014.

[7] Baker, D. R. and Kamat, P. V., "Photosensitization of tio2 nanostructures with cds quantum dots: Particulate versus tubular support architectures," *Advanced Functional Materials*, vol. 19, no. 5, pp. 805–811, 2009. ISI Document Delivery No.: 423NC Times Cited: 29 Cited Reference Count: 62 Baker, David R.

Kamat, Prashant V. Office of Basic Energy Science of the Department of the Energy ; Notre Dame Radiation Laboratory. [NDRL-4762] The research described herein was supported by the Office of Basic Energy Science of the Department of the Energy. This is contribution NDRL-4762 from the Notre Dame Radiation Laboratory. Wiley-v c h verlag gmbh Weinheim.

[8] Baram, N., Starosvetsky, D., Starosvetsky, J., Epshtein, M., Armon, R., and Ein-Eli, Y., "Enhanced inactivation of e-coli bacteria using immobilized porous tio2 photoelectrocatalysis," *Electrochimica Acta*, vol. 54, no. 12, pp. 3381–3386, 2009. ISI Document Delivery No.: 430TN Times Cited: 7 Cited Reference Count: 39 Baram, Nir Starosvetsky, David Starosvetsky, Jeana Epshtein, Marina Armon, Robert Ein-Eli, Yair Pergamon-elsevier science ltd Oxford.

[9] Bird, J. P., *Electron Transport in Quantum Dots*. Springer, 2003.

[10] Chitsulo, L., Engels, D., Montresor, A., and Savioli, L., "The global status of schistosomiasis and its control," *Acta tropica*, vol. 77, no. 1, pp. 41–51, 2000.

[11] Cho, M., Kim, J., Kim, J. Y., Yoon, J., and Kim, J. H., "Mechanisms of escherichia coli inactivation by several disinfectants," *Water Research*, vol. 44, no. 11, pp. 3410–3418, 2010. ISI Document Delivery No.: 613NH Times Cited: 0 Cited Reference Count: 44 Cho, Min Kim, Jaeeun Kim, Jee Yeon Yoon, Jeyong Kim, Jae-Hong Ministry of Education, Science and Technology [400-2008-0230]; Ministry of Environment This work was supported by WCU (World Class University) program through the Korea Science and Engineering Foundation funded by the Ministry of Education, Science and Technology (400-2008-0230) and the Ministry of Environment as "The Eco-technopia 21 project". The authors thank

Dr. Hwangsoo Joo at National Institutes of Health (NIH) for protein analysis experimental supports. Pergamon-elsevier science ltd Oxford.

[12] Deutch, J., Moniz, E., Ansolabehere, S., Driscoll, M., Gray, P., Holdren, J., Joskow, P., Lester, R., and Todreas, N., "The future of nuclear power," *an MIT Interdisciplinary Study, http://web. mit. edu/nuclearpower*, 2003.

[13] Erkmen, O. and Dogan, C., "Kinetic analysis of escherichia coli inactivation by high hydrostatic pressure in broth and foods," *Food Microbiology*, vol. 21, no. 2, pp. 181–185, 2004. ISI Document Delivery No.: 779XX Times Cited: 19 Cited Reference Count: 22 Academic press ltd elsevier science ltd London.

[14] Fujishima, A., Rao, T., and Tryk, D., "Titanium dioxide photocatalysis," *Journal of Photochemistry and Photobiology C: Photochemistry Reviews*, vol. 1, no. 1, pp. 1–21, 2000.

[15] Goldemberg, J. and Johansson, T., *World Energy Assessment: Overview: 2004 Update*. United Nations Publications, 2004.

[16] Guijarro, N., Lana-Villarreal, T., Mora-Sero, I., Bisquert, J., and Gomez, R., "Cdse quantum dot-sensitized tio2 electrodes: Effect of quantum dot coverage and mode of attachment," *Journal of Physical Chemistry C*, vol. 113, no. 10, pp. 4208–4214, 2009. ISI Document Delivery No.: 415ZM Times Cited: 12 Cited Reference Count: 44 Guijarro, Nestor Lana-Villarreal, Teresa Mora-Sero, Ivan Bisquert, Juan Gomez, Roberto Spanish Ministry of Science and Innovation [HOPE CSD2007-00007, CTQ2006-06286] This work was financially supported by the Spanish Ministry of Science and Innovation through projects HOPE CSD2007-00007(Consolider-Ingenio2010) and CTQ2006-06286.

N.G. thanks the MEC for the award of a FPU grant. Amer chemical soc Washington.

[17] Hayden, S. C., Allam, N. K., and El-Sayed, M. A., "Tio(2) nanotube/cds hybrid electrodes: Extraordinary enhancement in the inactivation of escherichia coli," *Journal of the American Chemical Society*, vol. 132, no. 41, pp. 14406–14408, 2010. Hayden, Steven C. Allam, Nageh K. El-Sayed, Mostafa A.

[18] Kang, Q., Lu, Q. Z., Liu, S. H., Yang, L. X., Wen, L. F., Luo, S. L., and Cai, Q. Y., "A ternary hybrid cds/pt-tio2 nanotube structure for photoelectrocatalytic bactericidal effects on escherichia coli," *Biomaterials*, vol. 31, no. 12, pp. 3317–3326, 2010. ISI Document Delivery No.: 576EB Times Cited: 0 Cited Reference Count: 66 Kang, Qing Lu, Qing Z. Liu, Shao H. Yang, Li X. Wen, Ling F. Luo, Sheng L. Cai, Qing Y. National Basic Research Program of China [2009CB421601]; National Science Foundation of China [20775024]; National Science Foundation [50725825] Support of this work by the National Basic Research Program of China (Grants No. 2009CB421601), the National Science Foundation of China (Grant No. 20775024), and the National Science Foundation for Distinguished Young Scholars (Grant No. 50725825) is gratefully acknowledged. We also thank the editor and reviewers whose valuable suggestions improved the quality of the manuscript. Elsevier sci ltd Oxford.

[19] Lewis, N. and Nocera, D., "Powering the planet: Chemical challenges in solar energy utilization," *Proceedings of the National Academy of Sciences*, vol. 103, no. 43, pp. 15729–15735, 2006.

[20] Manning, S.; Alcamo, I. H. D., *Escherichia Coli Infections (Deadly Diseases and Epidemics)*. Chelsea House Publications, 2004.

[21] McClure, S. A., Worfolk, B. J., Rider, D. A., Tucker, R. T., Fordyce, J. A. M., Fleischauer, M. D., Harris, K. D., Brett, M. J., and Buriak, J. M., "Electrostatic layer-by-layer assembly of cdse nanorod/polymer nanocomposite thin films," *Acs Applied Materials and Interfaces*, vol. 2, no. 1, pp. 219–229, 2010. ISI Document Delivery No.: 547CQ Times Cited: 1 Cited Reference Count: 99 McClure, Sean A. Worfolk, Brian J. Rider, David A. Tucker, Ryan T. Fordyce, Jordan A. M. Fleischauer, Michael D. Harris, Ken D. Brett, Michael J. Buriak, Jillian M. Natural Sciences and Engineering Research Council of Canada (NSERC), NRC-NINT ; University of Alberta, Micralyne Inc, iCORE ; Canadian Foundation for Innovation ; Alberta Ingenuity Fund ; Killarn Foundation This work was supported by the Natural Sciences and Engineering Research Council of Canada (NSERC), NRC-NINT, the University of Alberta, Micralyne Inc, iCORE, the Canadian Foundation for Innovation and Alberta Ingenuity Fund (J.A.M.F.). D.A.R. and M.F. acknowledge the Killarn Foundation for PDF fellowships. Dr. Sun at the Cross Cancer Institute and Dr. Chen in the Department of Medicine and Dentistry at the University of Alberta are thanked for their assistance with TEM. Abeed Lalany is acknowledged for Al Deposition and PV device testing, as well as Dr. Michael Taschuk for extensive work in calibrating the solar simulator. Dr. Al Meldrum and Ross Lockwood are thanked for access to and assistance with PL spectroscopy. Amer chemical soc Washington.

[22] McCullagh, C., Robertson, J., Bahnemann, D., and Robertson, P., "The application of tio 2 photocatalysis for disinfection of water contaminated with pathogenic micro-organisms: a review," *Research on Chemical Intermediates*, vol. 33, no. 3, pp. 359–375, 2007.

[23] Metz, B., Davidson, O., De Coninck, H., Loos, M., and Meyer, L.,

"Carbon dioxide capture and storage–special report of the intergovernmental panel on climate change," 2005.

[24] Nakicenovic, N. and Swart, R., "Emissions scenarios," *Intergovernmental Panel on Climate Change, Washington, DC, Summary for Policy Makers*, pp. 48–55, 2000.

[25] Organization, W. H., *UN-water Global Annual Assessment of Sanitation and Drinking-water: GLAAS 2010: Targeting Resources for Better Results*. World Health Organization, 2010.

[26] Siegenthaler, U., Monnin, E., Kawamura, K., Spahni, R., Schwander, J., Stauffer, B., Stocker, T., BARNOLA, J., and Fischer, H., "Supporting evidence from the epica dronning maud land ice core for atmospheric co2 changes during the past millennium," *Tellus B*, vol. 57, no. 1, pp. 51–57, 2005.

CHAPTER IV

SOLAR ENERGY CONVERSION: BIOMIMETIC PHOTOVOLTAICS WITH THE PHOTOSYNTHETIC PROTEIN, BACTERIORHODOPSIN

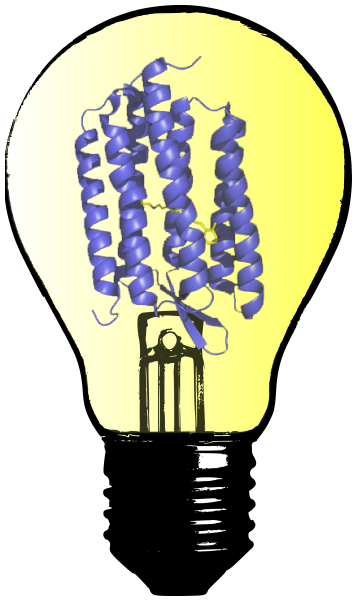

4.1 Chapter Summary

Bacteriorhodopsin (bR) is a light-transducing membrane protein proton pump that is easily cultured and isolated from certain strains of halophilic bacteria. We have explored the plasmonic field enhancement of bR photocurrent production by maximizing the blue light effect. In the blue light effect, the influx of blue photons absorbed by the long-lived M intermediate drastically shortens the time scale of the bR photocycle, leading to current enhancement. To this end, we used three approaches in our solution-based cell: (1) We improved the charge carrier separation in solution through

the use of a proton-selective Nafion membrane. (2) We maximized the plasmonic surface field effects by selecting the capping polymer with minimum surface field screening and best nanoparticle stability. (3) We selected the plasmonic nanoparticle with the strongest plasmonic field whose surface plasmon resonance has the best spectral overlap with the absorption of the M intermediate. Theoretical models are used to explain experimental results, which show a 40 nm cuboidal nanoparticle capped with 55k PVP polymer to give the best photocurrent enhancement. Enhanced by this particle, bR in our Nafion membrane solution cell gave a photocurrent of 0.21 μA/cm^3, which is 5000 times larger than the best published results for thin film bR electrochemical cells even with an applied bias. [59]

4.2 Solar Energy Conversion in Nature: Photosynthesis

Photosynthesis provides the energy for virtually all life on Earth, as well as the molecular oxygen necessary for the survival of aerobic organisms, such as monkeys. [57] This photochemical process involves the conversion of solar radiation into energy used to drive metabolic pathways and the synthesis of organic compounds. [48] When light is absorbed by a photosynthetic organism, the energy is converted and stored as high-energy molecular bonds in adenosine triphosphate (ATP), the primary energy carrier of living cells. Green plants containing chlrophyll are the most conspicuous photosynthetic organisms; however some bacteria and blue-green algae also use photosynthesis to power their cellular processes.

4.3 Bacteriorhodopsin, a Photosynthetic Protein

4.3.1 *Halobacterium halobium*

Like chlorophyll, bacteriorhodopsin is also a protein that is capable of photosynthesis. This protein is isolated from *Halobacterium halobium*, a bipolarly flagellated, rod-shaped bacterium approximately half a micron in diameter and 5 microns long (Figure 33). [28, 24]

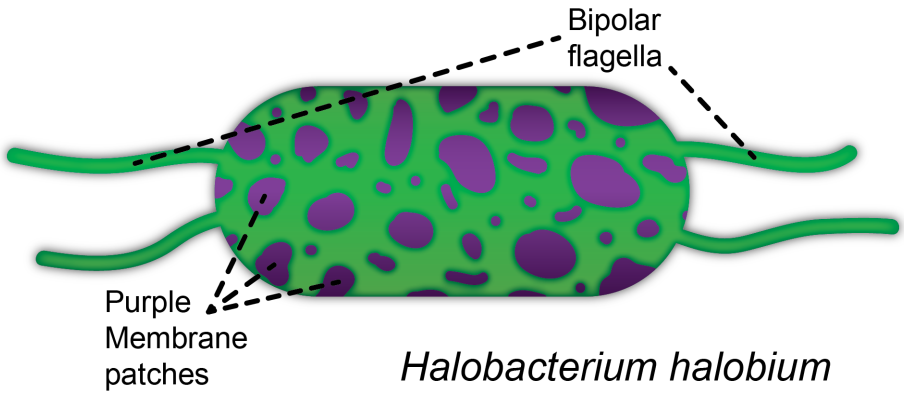

Figure 33: Rendering of the bipolarly-flagellated *Halobacterium Halobium* showing Purple Membrane two-dimensional crystalline patches.

As their name indicates, these halophilic bacteria thrive in environments with high salt concentrations (>3 M NaCl)[29, 41] such as those that have resulted from water evaporation such as the Great Salt Lake, the Dead Sea, and the salt marshes of the San Francisco Bay area. In fact, the original strain of bR that has been cultured and studied by our lab for almost 40 years was scavanged from these salt marshes with a five-gallon bucket in the 1970s. These bacteria are preferential aerobes, using molecular oxygen to power their cellular processes. [40] However, the solubility of O_2 is quite low in brine ponds, which often reach concentrations upwards of 4 M NaCl. Thus, *Halobacterium halobium* has evolved the ability to convert sunlight into energy for cellular processes in the absence of O_2.

4.3.2 The Purple Membrane

The plasma membrane of *H. halobium* is riddled with two-dimensional crystalline patches known as the purple membrane, or PM, [40, 44, 14] which are comprised mainly of the light-absorbing pigment, bR (ca. 75% protein, ca. 25% lipid by weight). [33, 35, 13] Bacteriorhodopsin is the simplest light-driven proton pump known; it is composed of seven alpha helices (248 amino acids), most of which are embedded in the membrane, and one interior retinal chromophore (Figure 34) in a two-dimensional hexagonal structure. [40, 44, 14, 33, 34, 13] It is this retinal chromophore that is

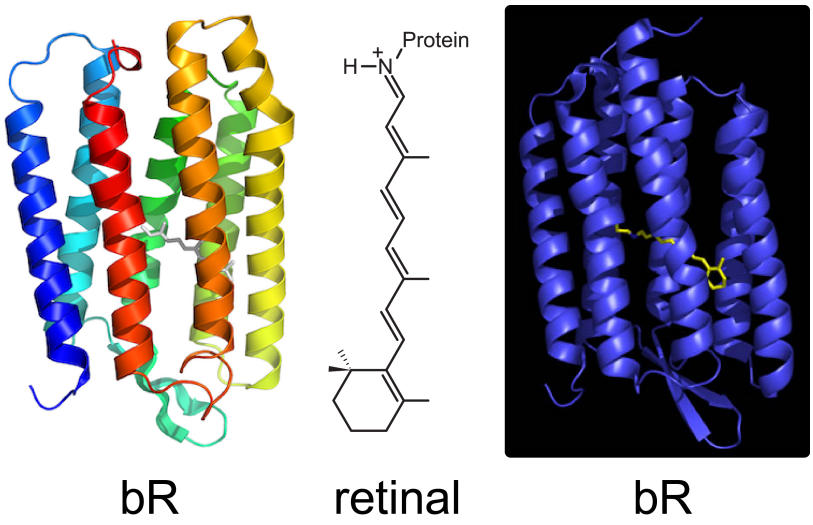

Figure 34: Rendering of the bacteriorhodopsin protein, composed of seven transmembrane alpha helices (emphasized in rainbow, right) and an internal retinal chromophore (molecular structure in middle, emphasized yellow on right).

responsible for the observed brilliant purple color of bR solutions.

4.3.3 The Bacteriorhopsin Protein

The transmembrane bacteriorhodopsin has a length of ca. 4.7 nm and a width of 2.5 - 3.5 nm, excluding its conjugated lipids (Figure 35). The bR protein offers advantages for its ease of generation and handling, as well as for its durability over a wide range of temperature and salt concentration ranges and preserved functionality over a wide pH range. [54, 63] It is also highly resistant to chemical and photochemical degradation. [63]

Following photoexcitation, bR molecules relax to their ground state via a series of conformational changes that allow this light-driven proton pump to move protons from the cytoplasmic to the extracellular side of its membrane. [36] This creates a proton gradient (electrochemical) that is used by the cell under anaerobic conditions for the formation of ATP from adenosine diphosphate (ADP) and inorganic phosphate (P_i) in a process that very closely resembles that used by mitochondria and chloroplasts: protons flow back across the membrane through the enzyme ATPase

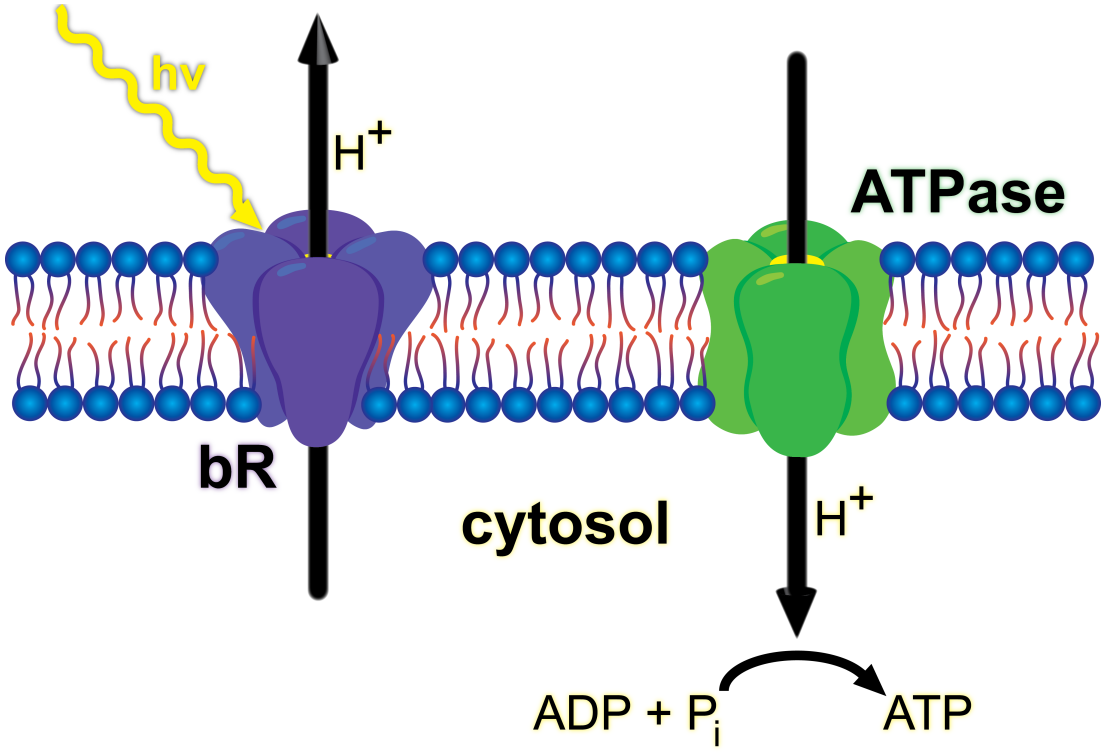

Figure 35: Schmatic rendering showing bR embedded in the membrane and coupling of the bR-produced electrochemical gradient to ATPase activity.

(Figure 35). [2] However, halobacteria neither produce O_2 nor carry out photoreduction of NADP+, which illustrates the less evolved nature of their phototransducing machinery compared to cyanobacteria or higher plants. [38]

4.3.4 The Retinal Chromophore

In the native, ground-state protein conformation, the retinal chromophore is bound to Lys-216 via a Schiff base linkage. [20] The chromophore is oriented ca. 20 degrees to perpendicular with respect to the membrane plane. It is located roughly midway through the membrane, dividing the protein cavity into two half-channels. [10] The outer-membrane half-channel contains polar residues that facilitate the transport of protons in concert with the nearby peptides. In contrast, the intra-membrane half-channel is mostly hydrophobic.

When a solution of bR is kept in the dark, the retinal chromophores reach an

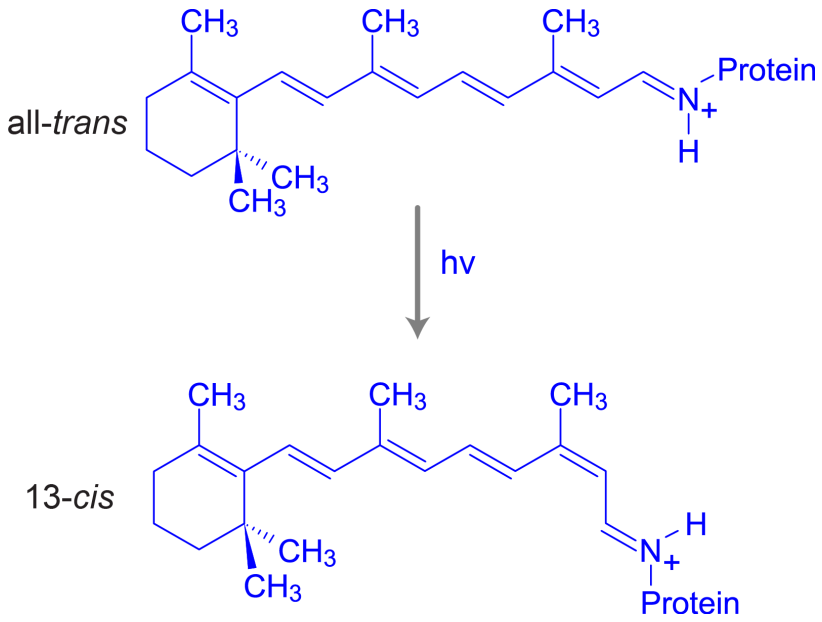

Figure 36: Retinal isomerization from the all-*trans* to the 13-*cis* conformation via absorption of a yellow photon begins the bR photocycle, during which bR uses the energy associated with the 13-*cis* conformation to drive the rest of the photocycle and pump a proton from the intra- to the extra-cellular space.

equilibrium between the all-*trans* and 13-*cis* conformations with roughly half of the chromophores having one configuration and the rest having the other. [49] This dark-adapted state has an absorption maximum at 560 nm, but it is broad enough that a wide range of light can initiate the photocycle. Upon photoexcitation and the resulting isomerization of the retinal chromophore, the protein begins a series of conformational changes to reprotonate the Schiff base and thereby return to the all-*trans* ground state by moving a proton from the intra- to the extra-membrane channel via a conformational change from its all-*trans* to its 13-*cis* conformation (Figure 36). This is performed in concert with its two facilitating residues, Asp-96 and Asp-85, which stabilize the Schiff base.

Overall, this deprotonation and reprotonation provides for vectorial proton transport through the membrane, while the geometry and electrostatic interactions between the Schiff base and its surrounding dipoles and charges (Asp-85, Asp-212, and Arg-82) tune the absorption maximum of bR to fit its biological function. [31] The

initiation of this progression, or photocycle, is characterized by a shift in the bR absorption peak to 568 nm, as the ratio of all-trans to 13-*cis* shifts from ca. 50:50 to ca. 95:5. [21] This is known as the light-adapted state of bR, and all experiments presented in this thesis were performed with bR that had been illuminated for at least 15 minutes to ensure that bR is in this light-adapted state. The specifics of this photocycle are discussed forthwith.

4.3.5 The Bacteriorhodopsin Photocycle

Bacteriorhodopsin has been the subject of intense study for decades. As a result, the lattice parameters of crystallized PM have been investigated extensively, and bR was the first membrane protein to have its crystal structure solved. [20] As a result, the specifics of the conformation change iterations that comprise its photocycle have been very well characterized. A simplified scheme of the photocycle is presented in Figure 37. Each intermediate state along the path back to ground-state bR has its own discrete absorbance profile and lifetime. The absorption maximum of each intermediate derives from the conformation of the retinal-protein system, and each maximum is represented in Figure 37 by the color of its box.

4.3.5.1 Proton Expulsion to the Extracellular Environment; Schiff Base Deprotonation

Ground state bR absorbs photons in the yellow (peak at 560 nm), initiating a transition through the incredibly short-lived (ca. 500 fs) I intermediate, an electronically excited state, the specifics of which are still a matter of some debate. [61, 55, 50, 15] The J intermediate, a thermally excited version of the ground state, follows. The vibrationally-hot J state decays after only 2.5 ps, [10, 3] giving rise to immediate charge separation via formation of the 13-*cis* K, the first intermediate that has been isolated at low temperature. [4]

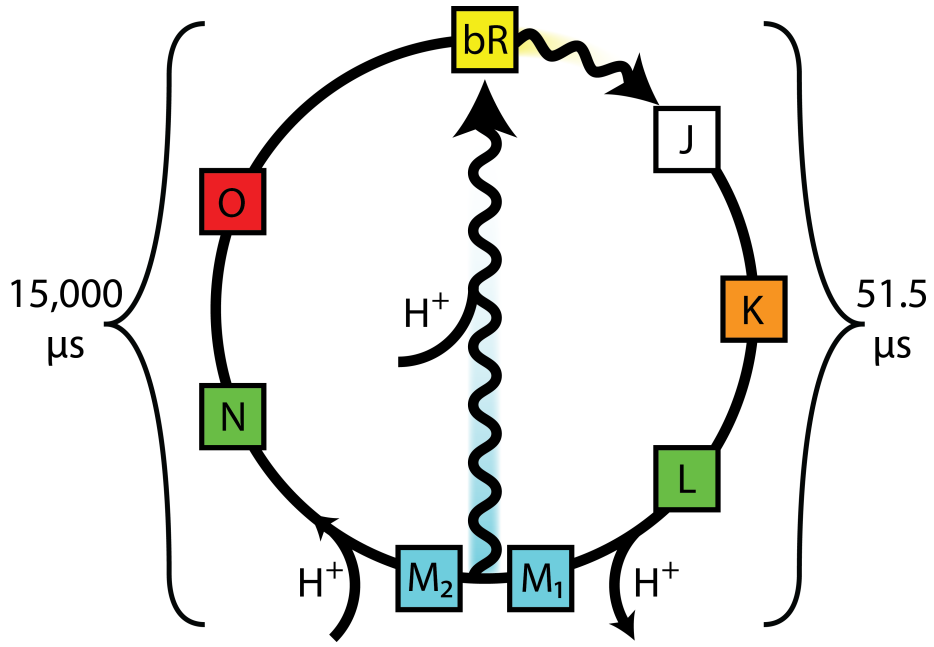

Figure 37: Simplified schematic of the bR photocycle. The photocycle is initiated upon the absorption of light by the retinal chromophore. The formation of M is associated with the loss of a proton to the exterior of the membrane, while the formation of N involves reprotonation of the system by a proton inside the membrane. As a result, a proton gradient is created across the membrane. The M intermediate can either thermally relax to the bR ground state through a series of conformational changes in a time of 15 ms, or can be photochemically converted back to the bR ground-state in a time of 200 ns via absorption of blue light. The color of the box around each intermediate reflects its spectral absorbance maximum in the visible region.

The K intermediate involves a highly strained, 13-*cis* retinal conformation containing enough excess enthalpy (50 $\frac{kJ}{mol}$) to drive the rest of the photocycle. [47] K converts to L over the course of ca. 1 μs, as rearrangements at the protein level relax the retinal somewhat, changing the local environment such that the pK_a value of the protonated Schiff base is lowered to ca. 8 and raising that of Asp-85 to ca. 9. [63] This renders Schiff base deprotonation - the transition to M - more energetically favorable. [30, 63]

M is formed from L as the proton is transferred from the Schiff base to Asp-85. This is witnessed by a relatively large hypsochromic shift in the absorbance peak maximum, giving rise to the blue-absorbing M intermediate, an integral component

to this thesis that will be explored in detail in Section 4.3.6. M is often described as having multiple sub-states; these do not involve changes in the bR protein itself, but rather are associated with clustering and rearrangement of hydrogen-bonded water in the cytoplasmic half-channel[62, 46, 52, 5, 53] that alters the pK_a of Asp-96 in such a way as to facilitate the M-to-N transition. [32]

This portion of the photocycle results in relatively rapid expulsion of a proton to the extracellular environment and, notably, requires only ca. 51.5 μs in total.

4.3.5.2 Proton Uptake from the Intracelluar Environment; Schiff Base Reprotonation

M decays to N under normal conditions as the Schiff base is reprotonated by Asp-96 from the cytoplasmic side of the membrane. [16] This is witnessed physcially, by a bending in the alpha-helices that increases the channel size on the cytoplasmic side, as well as spectrally, by a bathochromic shift in the absorbance maximum. [22] Having given up its proton in the M→N transition, Asp-96 recuperates said proton in the N→O transition. This is concurrent with the reisomerization of the Schiff base back to an all-*trans* conformation, suggesting what was proven in 1998 by Dioumaev - that the two events are coupled. [9]

The O-state is metastable;[45] as a result, little is known regarding its crystal structure. However, it is known to have a large, bathochromically-shifted absorbance in the red (ca. 680 nm). The O-state decays back to the bR ground state via deprotonation of Asp-85, the residue responsible earlier in the photocycle for accepting the Schiff base proton in the proton expulsion phase (L→M transition). The five main proton transfer steps are rendered schematically in Figure 38.

This portion of the photocycle, from M to ground state, requires ca. 15 ms and therefore comprises the bulk ($> 99.7\%$) of the photocycle timescale. This fact gains vital import in Section 4.3.6.

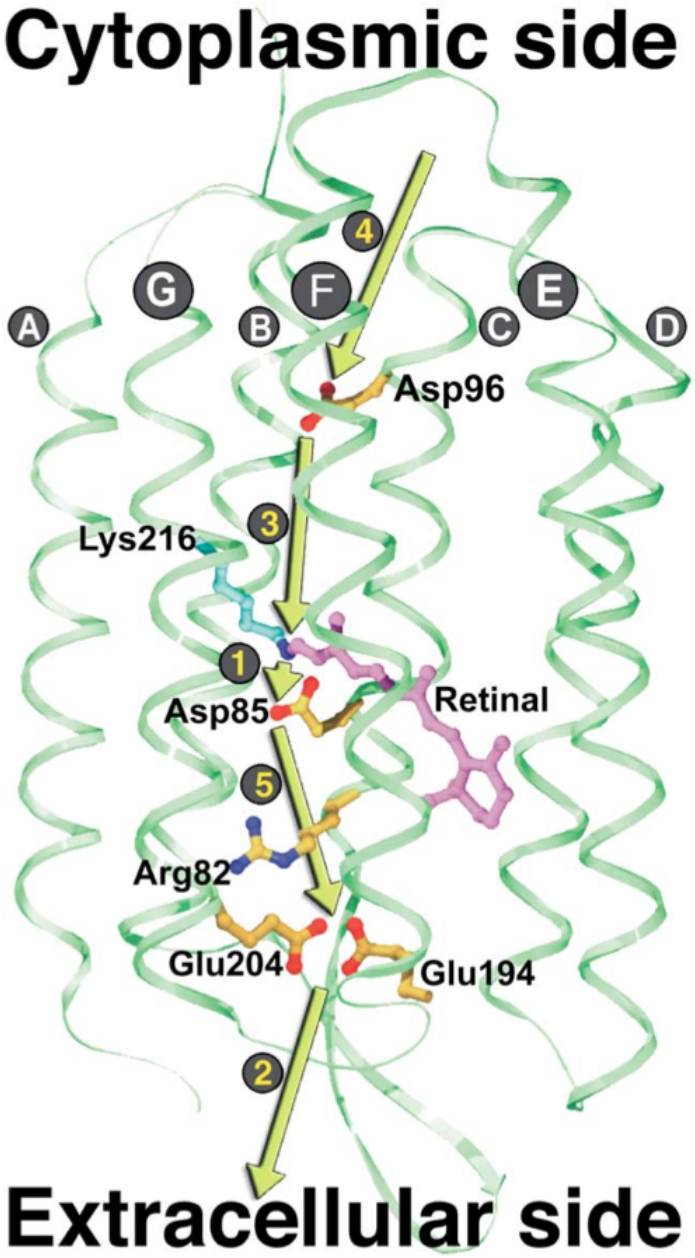

Figure 38: Schematic representation of the proton transfer steps in the bR photocycle, overlaid on the ground state model (ribbon representation in green, showing helices A to G). Strategic residues that participate in the proton transfer (Asp96, Asp85, Arg82, Glu194, Glu204), as well as the retinal bound to Lys216, are highlighted. The primary proton transfer (1) is from the Schiff base to Asp85. A proton is released to the extracellular medium (2) by the proton release group, thought to be formed by Glu194, Glu204 and water molecules. The Schiff base is subsequently reprotonated from Asp96 (3) which is then reprotonated from the cytoplasmic medium (4). The final proton transfer step (5) from Asp85 to the proton release group (via Arg82) restores the ground state. [39]

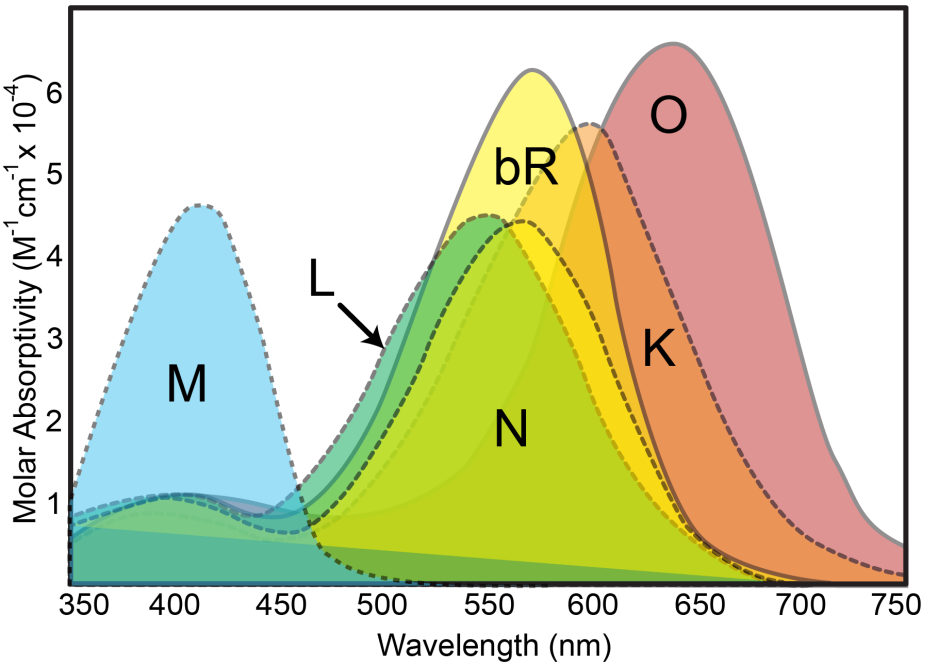

Figure 39: Extinction profiles of the main bR photocycle intermediates discussed in this thesis. The strong absorption of the M intermediate at ca. 410 nm gives rise to the blue light effect, which reduces the time associated with the bR photocycle by ca. 99.7%. Adapted from Birge et al. [1].

4.3.6 The Blue Light Effect

Following formation of the M intermediate, there are two pathways back to the ground state. Under normal conditions, the photocycle progresses through a series of relatively slow confomational changes to undergo thermal relaxation through the M→N→O→bR pathway (Section 4.3.5.2), which requires 15 ms. [43, 27] The second pathway is a photochemical process that occurs rarely in nature and is denoted as M→bR (Figure 37). This pathway is known as the blue light effect, and requires only ca. 200 ns. [37, 18]

The existence of the blue light effect derives from the strong absorbance of the M intermediate at ca. 410 nm (Figure 39). The blue light effect occurs when the M intermediate absorbs a blue photon (ca. 400 nm), resulting in chromophore reisomerization from 13-*cis* to all-*trans* in picoseconds and giving rise to the M' intermediate. M' then quickly decays to the ground state as the Schiff base is reprotonated in ca.

200 nanseconds. [22, 39] This second pathway shortens the traditional photocycle by 99.7%. This is advantageous for applications of bR in current production, as more rapid proton pumping yields greater charge carrier separation, which provides for increased photocurrent generation.

4.3.7 Bacteriorhodopsin Photocurrent

Under continuous wavelength (cw) illumination, bR exhibits a stationary photocurrent as it transforms light energy into electrochemical energy in the form of a proton gradient across its membrane. [7, 23, 56] The unique characteristics of bR (e.g. ease of generation, handling, and durability [54, 63]) make it promising for applications in solar energy. However, a limitation arises from the relatively poor native solar energy conversion efficiency of bR [56] compared to other materials, such as semiconducting metal oxides. [19] Table 4] gives some reported values for photocurrent production by bR thin film systems from a literature review by Jin et al. on this topic. [25] Jin et al. normalized the values to a per-monolayer basis, and the differences in device configurations and experimental set-ups are indicated. As indicated in Table 4, photocurrent values reported for bR thin film systems range on the picoampere scale (0.2 - 40 pA cm^2 per monolayer) even with the use of an applied bias.

4.3.8 The Laser Dynamics Lab 3D Photo-Electrochemical Cell

Recently, our group constructed a solution-based electrochemical cell that has no need for an external bias and does not require bR film preparation. [6] This cell is composed of ITO glass, O-rings, and a molecular porous membrane (Figure 40). The membrane allows for charge-carrier flux between the working (bR, citrate buffer) and reference cells (citrate buffer) while preventing the flux of the protein. Under continuous wavelength illumination, this cell exibits a stationary photocurrent of 1.5 nA/cm^3, [6] an almost two-orders-of-magnitude increase over reported values for bR thin-films per unit surface area.

Table 4: Comparison of photovoltage and/or photocurrent values attained for monolayers of non-aqueous bR in various device configurations. Adapted from Jin et al. [25].

Circuit (open/closed)	Film	Bias	Light trigger	Photo-voltage	Photo-current[a]
Al/bR/-/Au[c] (open)	Sub-ML[d]	Yes	CW $\lambda > 530$ nm 28 mW cm^{-2}	10 mV	none[e]
Al/bR/-/Au (open)	Sub-ML	Yes	CW $\lambda > 530$ nm 28 mW cm^{-2}	4 mV	none
ITO/bR/Al (closed)	1 μm OF[f]	No	Xenon arc lamp 1 mW cm^{-2}	none	3 pA cm^{-2}
ITO/bR/-/Au (open)	4 μm OF	Yes	CW $\lambda = 635$ nm, 2 mW cm^{-2}	3 mV	none
ITO/bR/-/BGO/ ITO[h] (open)	10 μm OF	No	CW $\lambda = 532$ nm 500 μJ cm^{-2}	none	none
(gate of) GaAs FET (open)	100 μm OF	Yes	CW He-Ne laser 50 μJ cm^{-2}	none	100 nA
Al/bR/Au (closed)	ML	Yes	CW $\lambda > 530$ nm, 28 μJ cm^{-2}	none	none
ITO/bR/Al (closed)	0.5 μm OF (in polymer)	Yes	CW λ=532nm, 2 mW cm^{-2}, chopped λ=350-600 nm	none	40 pA cm^{-2}
ITO/bR/Cu[b] (closed)	PVA[i] sol-gel (100 μm)	Yes, 20V	Square wave, $\lambda = 532$ nm, 600 mW cm^{-2}	0.2 mV	6 nA cm^{-2}
ITO/bR/Al (closed)	0.5 μm OF (in polymer)	Yes	CW pump source 2 mW cm^{-2}, $\lambda = 405$ nm	none	40 pA cm^{-2}
ITO/bR/Au/ GaAs (closed)	PVA (100 μm)	Yes	Laser, $\lambda = 632$ nm 800 mW cm^{-2}	none	0.2 pA cm^{-2}
ITO/AM/bR/ AM/InGa[j]	LBL[k]	No	Laser, $\lambda = 532$ nm	15mV	none

[a] Values are per monolayer and assume that the photo-voltage/-current response of bR is linearly proportional to the number of bR monolayers, i.e., the data are normalized in terms of the bR content in the multilayers.[b] Measurement taken under an external bias of 20 V. [c] /-/ = A gap in the circuit - open circuit measurement. [d] ML = monolayer. [e] I_{ph} = photocurrent. [f] OF = electric sedimentation oriented film. [g] PV = photovoltage. [h] BGO = bimuth germanium oxide. [i] PVA = poly(vinyl alcohol). [j] AM = apomembrane. [k] LBL = layer by layer with PDAC.

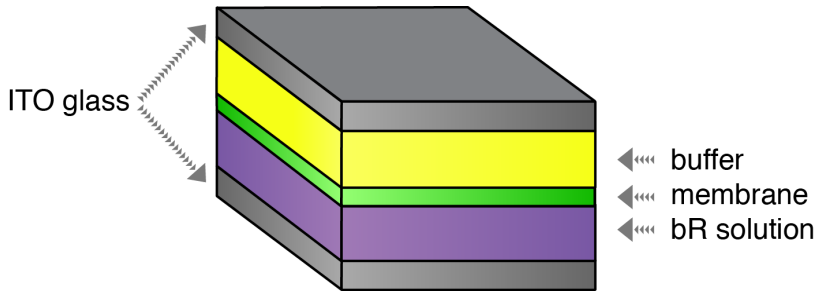

Figure 40: LDL bR electrochemical cell schematic

4.4 Plasmonic Nanoparticle Enhancement of the Bacteriorhodopsin Photocurrent

In an effort to enhance the photocurrent generation of bR further, we exploited the surface plasmon effect, which is induced by coupling of the incident electromagnetic light wave with the conduction band electrons in a metal nanoparticle. Silver nanoparticles, in particular, have a plasmon resonance band that overlaps well with the M intermediate absorption in the blue wavelength region and should enable us to intensify what is known as the blue light effect. [58, 22]

Yen et al. reported that the bR photocurrent is greatly enhanced in the presence of silver nanoparticles when the electrochemical cell is exposed to blue light (Figure 41). [58]

The plasmonic field of silver nanoparticles causes them to function like nanoscale lenses and greatly enhances the flux of blue photons. What follows is an enhancement of the blue light effect and a consequent increase in the rate of proton release. This results in an enhanced steady-state proton concentration and photocurrent. The maximum photocurrent reported previously by our lab is 25 nA/cm^3, using bR mixed with silver nanoparticles (1.2 nM) capped with citrate molecules. [58] These values were reproduced and are shown in Figure 41 both under full visible spectrum irradiation (left) and under the same irradiation but using a filter to block the blue light (right). When bR is in the presence of silver nanospheres but the blue light is blocked, the steady-state photocurrent is the same as that observed for native, un-enhanced

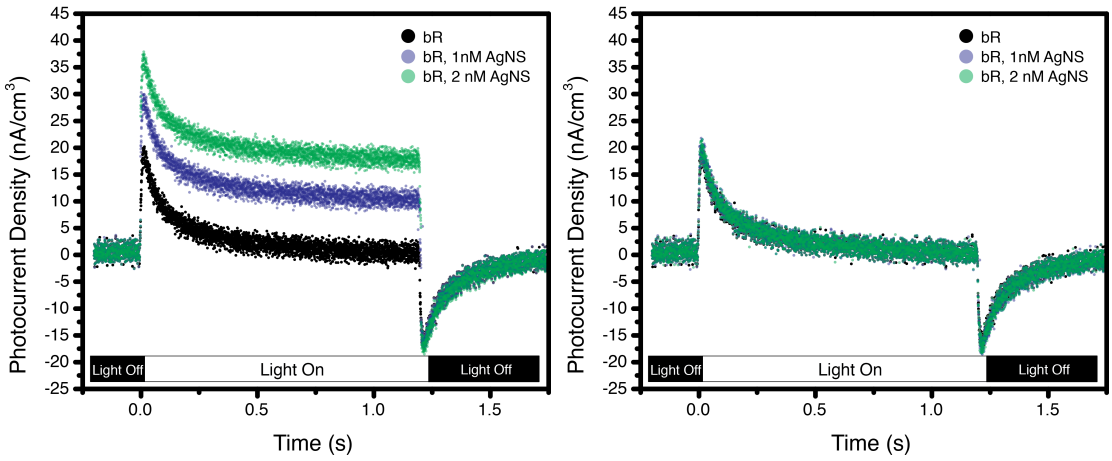

Figure 41: Bacteriorhodopsin photocurrent generation in the presence of 0 nM (black), 1 nM (blue), and 2 nM (green) silver nanospheres under full spectrum visible CW light (left) and under the same irradiation but using a filter to block the blue light (right). Illustrates that the photocurrent enhancement seen in the presence of silver nanospheres is indeed a product of the blue light effect.

bR.

To make bR more promising for solar energy applications, we must maximize the photocurrent generation, which requires maximization of each of three enhancement components. Each of these components is treated in turn in the following sections:

1. Maximize the proton polarization in the solution cell. The nonselective porous membrane is substituted for a proton-selective Nafion membrane.

2. Minimize screening of surface field intensity by optimizing the capping material thickness around the nanoparticle. The charged nature of the Nafion membrane precludes the use of capping agents such as citrate. The most favorable molecular weight of a neutral polymer capping agent (PVP) was chosen based on maximum photocurrent enhancement and best stability.

3. Maximize the plasmonic field intensity and spectral overlap with the M intermediate to maximize the blue light effect.

4.4.1 Minimizing Ionic Depolarization Effects

A porous membrane was used in our previous bR electrochemical cell to separate the two half-cells (bR working cell and reference cell, Section 4.3.8). [58] Porous membranes are attractive for their low cost, but they suffer from nonselective transport of cations and anions across the membrane. [17] This leads to an initial spike in the photocurrent density that results from rapid proton flux across the membrane, and it is followed by a decay in photocurrent density as the larger, bulkier anions traverse the membrane and begin neutralizing some of the charges (Figure 42). This porous membrane generated a stationary photocurrent of 1.5 nA/cm^3, which is only 7% of the intensity of the initially formed photocurrent (20 nA/cm^3).

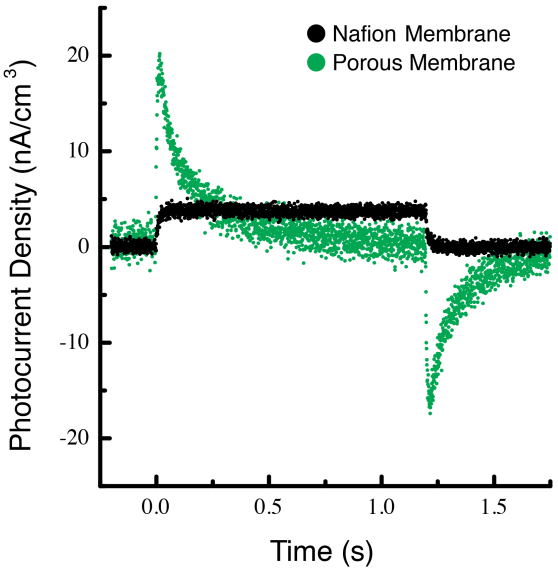

Figure 42: Bacteriorhodopsin native photocurrent generation using porous (green) and Nafion (black) membranes. The steady state current is enhanced as a result of the proton selectivity of the Nafion membrane.

Known for their ability to generate stable photocurrents, Nafion membranes have come into widespread use for applications in areas such as proton exchange membrane (PEM) fuel cells. [42] These membranes exhibit selectivity for cations through the use of anionic channels and thereby limit the flux of anions across the membrane

(Figure 43). [60] This increases the overall charge carrier separation and allows for a stable photocurrent (4.6 nA/cm^3) that is higher than that generated by the porous membrane. Figure 42 illustrates this gain in the steady state current. However, it also shows that we did not reach the initial polarization seen in the transient spike with the porous membrane. This might suggest that by finding a more efficient cation-selective membrane, we might get a great deal more current enhancement.

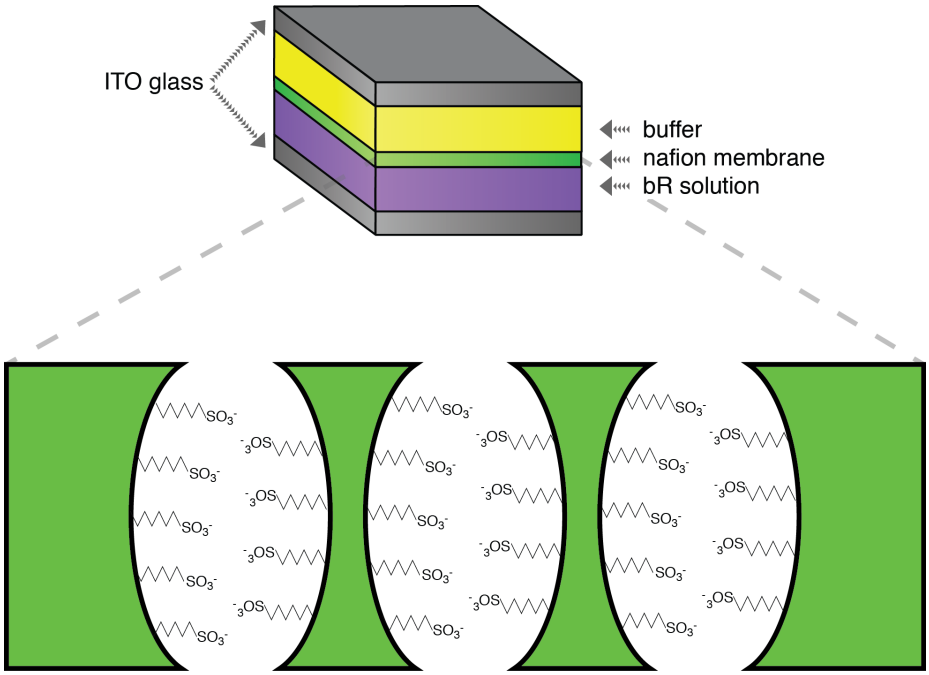

Figure 43: LDL wet electrochemical cell schematic with Nafion membrane. The chemistry of the Nafion membrane pores is depicted in the zoom. The proton-selectivity of this membrane arises from its negatively-charged, sulfate-group-lined pores.

4.4.2 Minimizing Shielding of the Surface Plasmon Fields

The previously used citrate-capped silver nanoparticles (Section 4.3.8) are not suitable for this work, as the charged nature of the Nafion membrane destabilizes charged capping agents and leads to particle aggregation. We instead examined several different molecular weights of polyvinylpyrrolidone (PVP) polymers in order to select the polymer providing the best stability with the thinnest capping shell, as shell thickness screens the nanoparticle surface field felt by the bR molecules in solution. We

studied both the plasmonic field enhancement of the bR photocurrent and the stability of the silver nanoparticles as a function of capping shell thickness. The silver nanospheres with varied chain-length PVP capping agent were prepared via a polyol process[51] using PVP polymers of 10k, 55k, and 365k g/mol molecular weight in separate syntheses (procedure and instrumentation in Appendix C). The synthesized silver spherical nanoparticles of roughly 40 nm (±5 nm) diameter showed excellent spectral overlap with the M intermediate absorption in bR (Figure 44).

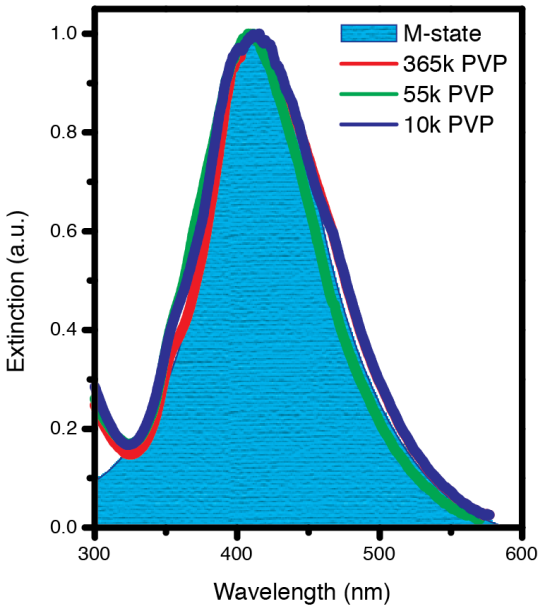

Figure 44: Extinction spectra of silver nanospheres capped with 10k (blue), 55k (green), and 365k (red), M.W. PVP showing spectral overlap with the M intermediate of bR (shaded cyan).

The dynamic light scattering (DLS) technique was used to measure the hydrodynamic diameter of the resulting particles, and transmission electron microscopy (TEM) was used to measure the diameter of the metallic core. Since the particles have the same capping material, subtraction of the core radii from the hydrodynamic radii provides the relative capping shell thicknesses (Figure 45).

The full length of the smallest molecular weight PVP is approximately 600 nm, which is much larger than the thickness of the corresponding capping shell (18 nm).

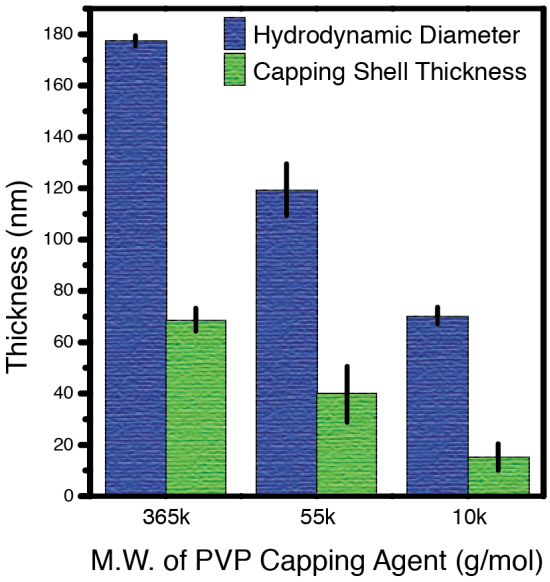

Figure 45: Hydrodynamic diameter (blue) and relative capping shell thickness (green) for 10k, 55k, and 365k M.W. PVP-capped silver spheres.

This suggests that the PVP is wrapped around the nanoparticles in a complex manner. Error bars on the hydrodynamic diameter represent the standard deviation among the 20 DLS measurements for each sample, and error bars on the capping shell thicknesses are propagated from both the hydrodynamic diameter measurements and the TEM measurements.

Figure 51 (black) shows the photocurrent generation of a solution of bR and of bR/silver nanoparticle mixtures. During the irradiation period, the photocurrent reached a maximum steady state in about 50 ms and retained this maximum for the duration of the irradiation period. This plateau feature in the photocurrent profile and lack of spiking are a result of the proton selectivity of the Nafion membrane. Photocurrent measurements of bR in the presence of equivalent concentrations (2 nM) of each of our silver nanoparticles in turn showed an enhancement of the photocurrent with decreasing capping shell thickness (Figure 46, red, green, blue). Stronger effective field intensity from thinner capping shells yields larger photocurrent enhancement for these particles with virtually the same spectral overlap with the M intermediate

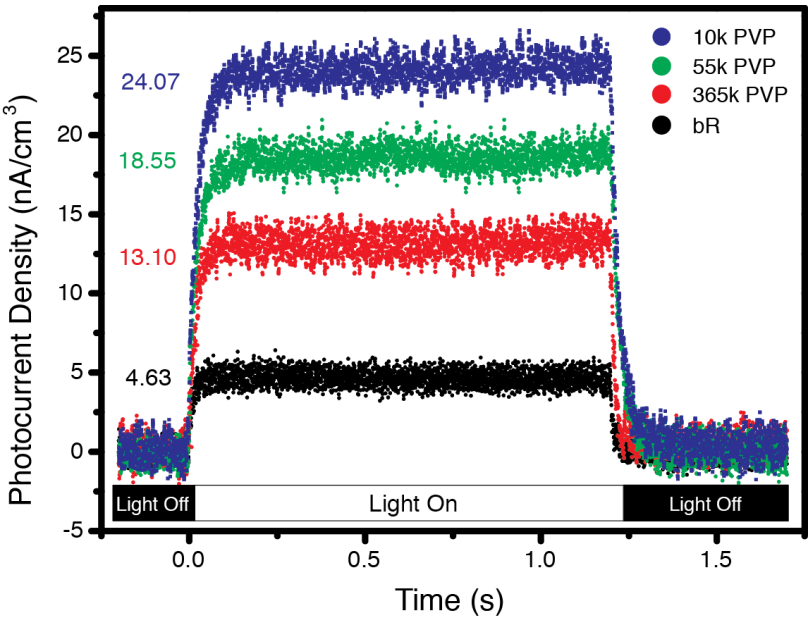

Figure 46: Bacteriorhodopsin native photocurrent generation (black) and bR photocurrent generation under enhancement by 40 nm silver spheres capped with PVP of MW 10k (blue), 55k (green), and 365k (red).

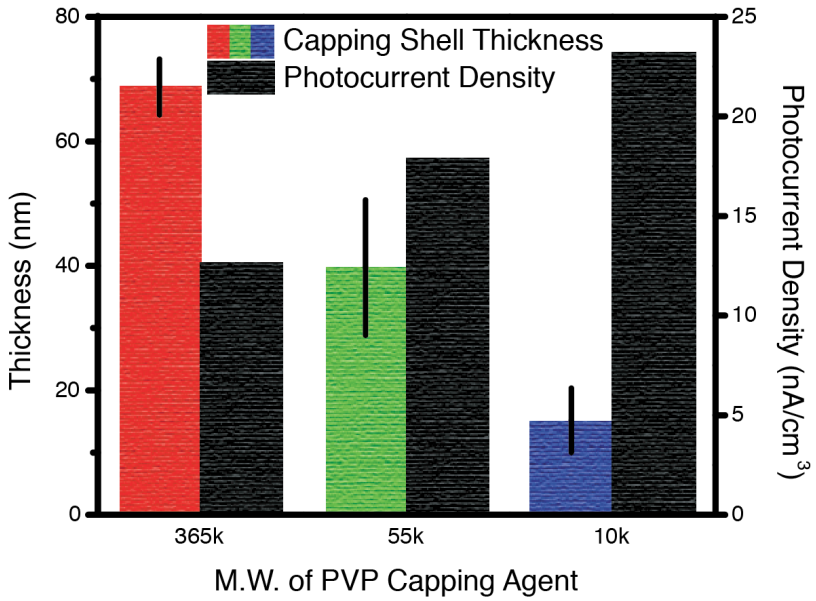

Figure 47: Capping shell thickness (green) and bR photocurrent density (black) for silver spheres capped with PVP of the designated molecular weight. This inverse relationship results from the capping material shielding the particle plasmonic field.

(Figure 44). This relationship between photocurrent generation and capping shell thickness is shown in Figure 47.

Field strength is as critical as postulated, and the 10k PVP-capped spheres provided the best enhancement of the photocurrent; however, particle instability was noted spectrally and via TEM after several 10 min experiments with the same 10k PVP-capped particles. In contrast, the 55k- and 365k-capped particles showed stability up to at least 1 week in the presence of the reaction mixture of bR and citrate buffer, suggesting 55k PVP-capped particles to be the most attractive choice for their balance of large photocurrent enhancement and good long-term stability.

4.4.3 Particle Shape Effects: Importance of Spectral Overlap and Surface Field Strength.

Since the 55k MW PVP provides for the best particle stability with the least detriment to plasmonic field strength, we used this capping agent in our efforts to study the shape dependence of silver nanoparticles on photocurrent enhancement. The unique surface plasmon resonance of metal nanoparticles is highly sensitive to their local environment as well as their size, shape, and composition. [26, 8] In the previous section (Section 4.4.2), we focused solely on spherical silver nanospheres, as their surface plasmon resonance spectrum has the best overlap with M intermediate absorption. Changing the shape of the particle to increase the field intensity should increase the photocurrent enhancement. However, altering particle shape also shifts the absorbance profile, thereby altering spectral overlap with the M intermediate. We examined a progression of shapes from spheres to cubes, all capped with 55k PVP and having very similar capping shell thicknesses (Figure 44), in order to find the particle with both the strongest field and the best spectral overlap of the plasmon with the M intermediate absorption.

Figure 48 shows the TEM images of these particles, which are referred to herein as perfect cubes, cubes with slightly truncated corners (cuboid-B), cubes with highly

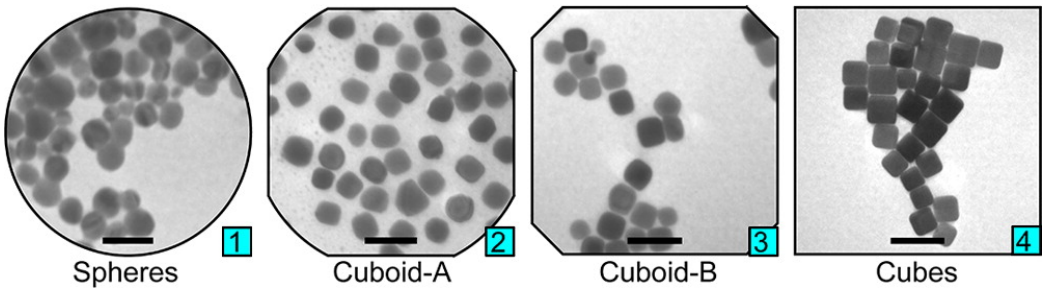

Figure 48: TEM images of spheres (1), cuboid-A with highly truncated corners (2), cuboid-B with slightly truncated corners (3), and perfect cubes (4) with shape-representative image frames. (Scale bars = 100 nm.)

truncated corners (cuboid-A), and cubes with fully truncated corners (spheres). All crystalline nanoparticles (spheres, cubes, and cuboids) were synthesized using the same chemicals, reaction vessels, heat settings, capping agents, and cleaning techniques to ensure that particle and medium composition were consistent throughout. Shape variations were achieved by altering solution perturbation speed during synthesis, with slow stirring (ca. 300 rpm) yielding cubes, high stirring (ca. 900 rpm) generating spheres, and intermediate stirring (ca. 450, ca. 550 rpm) yielding cuboids.

Metal nanoparticles with features such as corners and edges (e.g., prisms, cubes) are known to exhibit larger plasmonic field intensities than particles lacking these geometric features (spheres). We performed discrete dipole approximation (DDA) calculations [11, 12] for a 40 nm silver sphere and a 40 nm edge length cube (Figure 49). When shown on the same field intensity scale, cubes show the expected strongest field intensity at their edges and corners.

This increased field intensity is advantageous for the enhancement of bR photocurrent; however, a red-shift in the plasmon resonance occurs as one progresses from a spherical shape to a cubic shape through cuboidal intermediates. In this progression from a spherical shape to a perfect cube, we see both increasingly better resolution of the cubic peaks and a gradual red-shift in the main plasmon peak (Figure 50) that results in less spectral overlap of the plasmon with the M intermediate absorption.

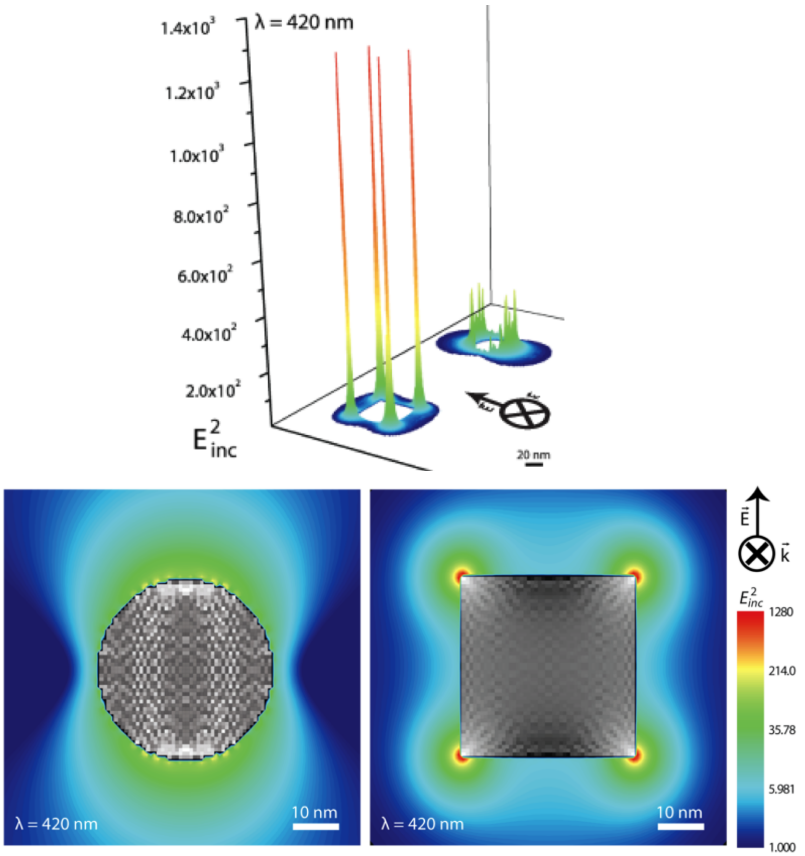

Figure 49: Discrete dipole approximation plots of the electric fields in 3D (top) and 2D (bottom) for a 40 nm silver sphere and a 40 nm edge-length silver cube, demonstrating stronger plasmon field with sharper corners.

We used this shape progression to study the trade-off between an increase in the plasmonic field strength and the decrease that ensues in the degree of spectral overlap with the M intermediate absorption.

Over the 1.2 s time scale (Figure 51), the photocurrent density of bR in the presence of silver cuboid-B is much higher than even that of silver spheres capped with 10k MW PVP. However, the photocurrent density of cuboid-B over this 1.2 s exposure time was not stationary, showing a steady rise. The time scale was adjusted to 1000 s to investigate this. Over the course of this longer time scale experiment (Figure 52), the bR photocurrent density remained the same for both the native bR and for the 55k MW PVP-capped silver spheres as that seen in the short time scale experiments (Figure 51). However, for both cuboids and cubes, the photocurrent density increased

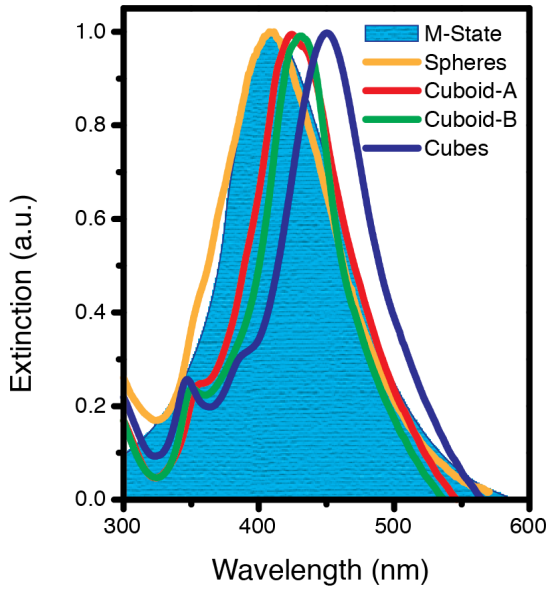

Figure 50: Extinction spectra of 40 nm silver spheres (pink), cuboids (red, green), and cubes (blue) capped with 55k MW PVP showing decreasing spectral overlap with the M intermediate of bR (shaded cyan) with increasing sharpness of cube corners.

dramatically, reaching a maximum after 100 s that was maintained over the course of the 1000 s exposure interval with no change in solution temperature (0.1 ^{o}C). Cuboid-A, with highly rounded corners, reached a maximum photocurrent density of 103.6 nA/cm^3 after 100 s, a stark contrast to the ca. 36 nA/cm^3 photocurrent density observed over the 1.2 s time scale experiments. The highest photocurrent density achieved in these experiments was for bR enhanced by cuboid-B, which produced a photocurrent of 0.2 μA/cm^3. This value is 50 times higher than pure bR in our wet electrochemical system (4.64 nA/ cm^3) and 8 times higher than our previous report using silver nanospheres and a porous membrane system (25 nA/cm^3). [58] The large enhancement intensity results from the much stronger field associated with cuboid shapes compared to spheres, though the mechanism of the slower rise in photocurrent density is yet to be elucidated.

Interestingly, despite their even stronger field intensity, perfect cubes displayed less enhancement of the bR photocurrent than did cuboid-B. The absorption profile

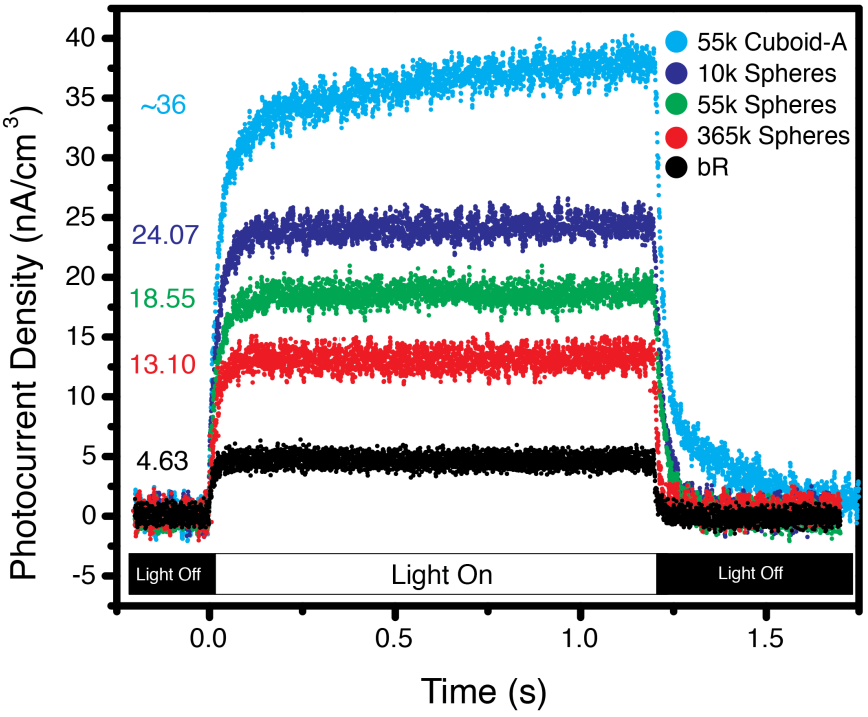

Figure 51: Bacteriorhodopsin native photocurrent generation (black), bR photocurrent generation under enhancement by 40 nm silver nanospheres capped with PVP of MW 10k (blue), 55k (green), and 365k (red) and initial, short-time scale observation of enhancement using 40 nm edge length silver cuboid-A capped with 55k MW PVP (cyan).

of these silver nanoparticles (Figure 50) provides the reason for this decrease. The degree of spectral overlap with the M intermediate, which is necessary for the blue light effect to occur, decreases significantly as the shape changes from cuboid-B to perfect cubes. As we have shown previously, a higher degree of spectral overlap between the plasmonic particle and the M absorption results in a higher photocurrent density. These results and contributing factors are rendered visually in Figure 53, where the peak in photocurrent density (black) is apparent for the particle that falls nearest the intersection of the plots of field strength (corner integrity, green) and spectral overlap with the M intermediate (blue). The photocurrent density of silver cuboid-enhanced bR is as high as 0.2 μA/cm^3, which is 10 times higher than that of bR enhanced by silver nanospheres (ca. 20 nA/cm^3) and orders of magnitude higher

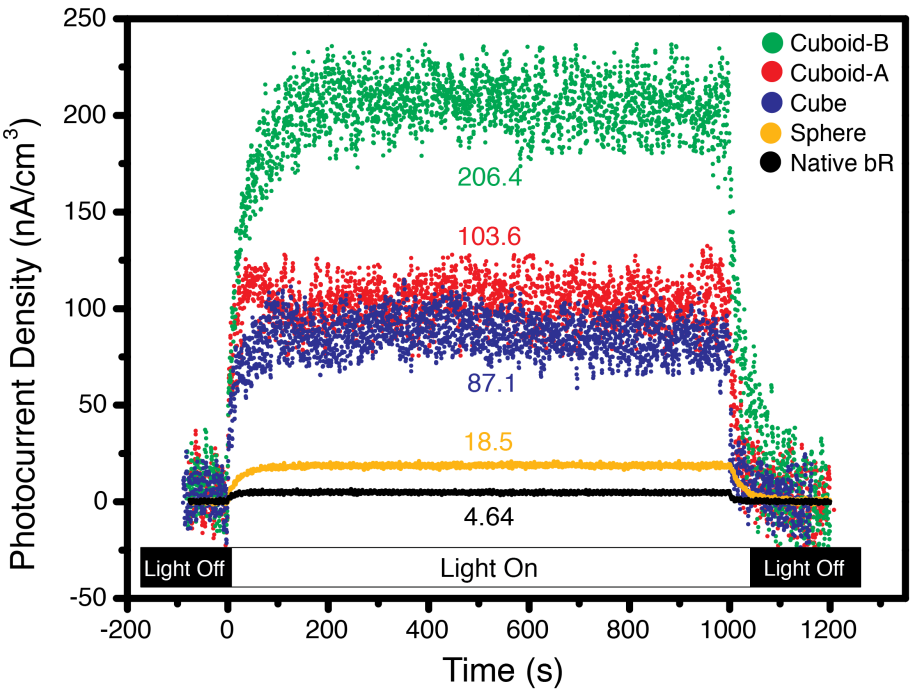

Figure 52: Bacteriorhodopsin photocurrent generation under blue light enhancement from 40 nm silver particles capped with 55k MW PVP. Illustrates photocurrent enhancement of native bR (black) using spheres (yellow), cuboid-A with highly truncated corners (red), cuboid-B with slightly truncated corners (green), and perfect cubes (blue).

(ca. 5,000 times higher) than the best published results for thin film electrodes. This high photocurrent density was found to be stable for up to 6 consecutive hours of continuous irradiation, demonstrating the utility of specifically tailoring surface plasmons to the task at hand.

4.5 Concluding Remarks

By making use of our knowledge of plasmonics, we were able to greatly enhance the photocurrent of the bacteriorhodopsin system. We first replaced the traditional thin film system, which can trap charge carriers, with a solution-based cell that requires no bias. We then used a cation-selective membrane to increase the proton polarization, demonstrating the need for highly selective membranes for maximum current

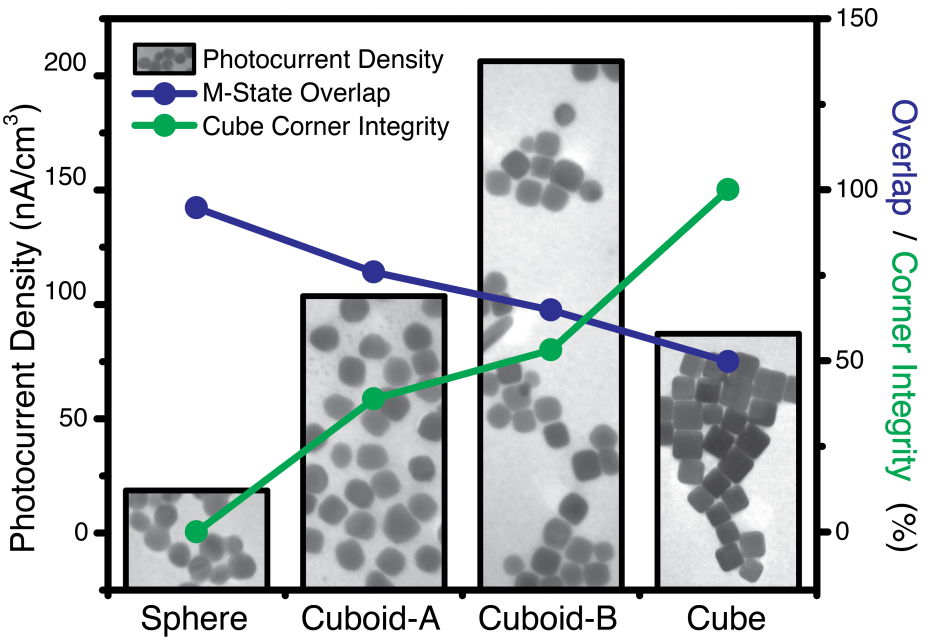

Figure 53: Photocurrent density of bR for each shape (black bars), spectral overlap between the surface plasmon resonance band of the nanoparticle and the M intermediate absorption (blue), and the cube corner integrity (green) as an indicator of field strength. Relative overlap percentage was determined via integration of the normalized curves, and relative corner integrity was measured using the radius of curvature from TEM images (full explanation in Appendix C). This figure illustrates that the largest enhancement in photocurrent density results from the particle that falls nearest the intersection of spectral overlap and field strength, the 40 nm cuboid-B capped with 55k MW PVP.

enhancement. In this work, we have illustrated the need for both maximum particle field strength and plasmonic spectral overlap with the blue-light-absorbing M intermediate in plasmonic-enhanced bR electrochemical cells. The number of plasmonic nanoparticles with different field strengths and plasmon wavelengths is always increasing. Finding a new particle that has a stronger electromagnetic field, better spectral overlap with the M intermediate, and a small capping shell is quite possible and will lead to maximum photocurrent enhancement.

4.6 REFERENCES

[1] Birge, R. R., Gillespie, N. B., Izaguirre, E. W., Kusnetzow, A., Lawrence, A. F., Singh, D., Song, Q. W., Schmidt, E., Stuart, J. A., Seetharaman, S., and Wise, K. J., "Biomolecular electronics: Protein-based associative processors and volumetric memories," *The Journal of Physical Chemistry B*, vol. 103, no. 49, pp. 10746–10766, 1999. doi: 10.1021/jp991883n.

[2] Bogomolni, R. and others, "Light energy conservation processes in halobacterium halobium cells.," in *Federation proceedings*, vol. 36, p. 1833, 1977.

[3] Brack, T. and Atkinson, G., "Vibrationally excited retinal in the bacteriorhodopsin photocycle: picosecond time-resolved anti-stokes resonance raman scattering," *The Journal of Physical Chemistry*, vol. 95, no. 6, pp. 2351–2356, 1991.

[4] Braiman, M. and Mathies, R., "Resonance raman spectra of bacteriorhodopsin's primary photoproduct: evidence for a distorted 13-cis retinal chromophore," *Proceedings of the National Academy of Sciences*, vol. 79, no. 2, pp. 403–407, 1982.

[5] Cao, Y., Varo, G., Chang, M., Ni, B., Needleman, R., and Lanyi, J., "Water is required for proton transfer from aspartate-96 to the bacteriorhodopsin schiff base," *Biochemistry*, vol. 30, no. 45, pp. 10972–10979, 1991.

[6] Chu, L. K., Yen, C. W., and El-Sayed, M. A., "Bacteriorhodopsin-based photo-electrochemical cell," *Biosensors and Bioelectronics*, vol. 26, no. 2, pp. 620–626, 2010. Chu, Li-Kang Yen, Chun-Wan El-Sayed, Mostafa A.

[7] Chu, L. K., Yen, C. W., and El-Sayed, M. A., "On the mechanism of the plasmonic field enhancement of the solar-to-electric energy conversion by the other photosynthetic system in nature (bacteriorhodopsin): Kinetic and spectroscopic study," *Journal of Physical Chemistry C*, vol. 114, no. 36, pp. 15358–15363, 2010. ISI Document Delivery No.: 644TQ Times Cited: 0 Cited Reference Count: 29 Chu, Li-Kang Yen, Chun-Wan El-Sayed, Mostafa A. U.S. Department of Energy, Office of Basic Energy [DE-FG02-97-ER 14799] We would like to thank the U.S. Department of Energy, Office of Basic Energy Grant No. DE-FG02-97-ER 14799. We also thank Mrs. Rachel Near for her carefully revising this manuscript. Amer chemical soc Washington.

[8] Daniel, M.-C. and Astruc, D., "Gold nanoparticles: assembly, supramolecular chemistry, quantum-size-related properties, and applications toward biology, catalysis, and nanotechnology," *Chemical Reviews*, vol. 104, no. a213219e-00c4-fad2-5f23-8c11dc845d91, pp. 293–639, 2004. 10.1021/cr030698+.

[9] Dioumaev, A., Richter, H., Brown, L., Tanio, M., Tuzi, S., Saitô, H., Kimura, Y., Needleman, R., and Lanyi, J., "Existence of a proton transfer chain in bacteriorhodopsin: participation of glu-194 in the release of protons to the extracellular surface," *Biochemistry*, vol. 37, no. 8, pp. 2496–2506, 1998.

[10] Doig, S., Reid, P., and Mathies, R., "Picosecond time-resolved resonance raman spectroscopy of bacteriorhodopsin's j, k, and kl intermediates," *The Journal of Physical Chemistry*, vol. 95, no. 16, pp. 6372–6379, 1991.

[11] Draine, B. T. and Flatau, P. J., "Discrete-dipole approximation for scattering calculations," *Journal of the Optical Society of America a-Optics Image Science and Vision*, vol. 11, no. 4, pp. 1491–1499, 1994. ISI Document Delivery No.: NE243 Times Cited: 612 Cited Reference Count: 69.

[12] Draine, B. T. and Flatau, P. J., "Ddscat 6.1," 2005.

[13] Edman, K., Nollert, P., Royant, A., Belrhali, H., Pebay-Peyroula, E., Hajdu, J., Neutze, R., and Landau, E. M., "High-resolution x-ray structure of an early intermediate in the bacteriorhodopsin photocycle," *Nature*, vol. 401, no. 6755, pp. 822–826, 1999.

[14] Essen, L. O., Siegert, R., Lehmann, W. D., and Oesterhelt, D., "Lipid patches in membrane protein oligomers: Crystal structure of the bacteriorhodopsin-lipid complex," *Proceedings of the National Academy of Sciences of the United States of America*, vol. 95, no. 20, pp. 11673–11678, 1998.

[15] Garavelli, M., Vreven, T., Celani, P., Bernardi, F., Robb, M., and Olivucci, M., "Photoisomerization path for a realistic retinal chromophore model: the nonatetraeniminium cation," *Journal of the American Chemical Society*, vol. 120, no. 6, pp. 1285–1288, 1998.

[16] Gerwert, K., Hess, B., Soppa, J., and Oesterhelt, D., "Role of aspartate-96 in proton translocation by bacteriorhodopsin," *Proceedings of the National Academy of Sciences*, vol. 86, no. 13, pp. 4943–4947, 1989.

[17] Granick, S., "Motions and relaxations of confined liquids," *Science*, vol. 253, no. 5026, pp. 1374–1379, 1991. ISI Document Delivery No.: GF851 Times Cited: 526 Cited Reference Count: 76 Amer assoc advancement science Washington.

[18] Hampp, N., "Bacteriorhodopsin: mutating a biomaterial into an optoelectronic material," *Applied microbiology and biotechnology*, vol. 53, no. 6, pp. 633–639, 2000.

[19] Hayden, S. C., Allam, N. K., and El-Sayed, M. A., "Tio(2) nanotube/cds hybrid electrodes: Extraordinary enhancement in the inactivation of escherichia

coli," *Journal of the American Chemical Society*, vol. 132, no. 41, pp. 14406–14408, 2010. Hayden, Steven C. Allam, Nageh K. El-Sayed, Mostafa A.

[20] Henderson, R., Unwin, P., and others, "Three-dimensional model of purple membrane obtained by electron microscopy," *Nature*, vol. 257, no. 5521, p. 28, 1975.

[21] Herbst, J., Heyne, K., and Diller, R., "Femtosecond infrared spectroscopy of bacteriorhodopsin chromophore isomerization," *Science*, vol. 297, no. 5582, pp. 822–825, 2002.

[22] Hessling, B., Herbst, J., Rammelsberg, R., and Gerwert, K., "Fourier transform infrared double-flash experiments resolve bacteriorhodopsin's m1 to m2 transition," *Biophysical journal*, vol. 73, no. 4, pp. 2071–2080, 1997.

[23] Horn, C. and Steinem, C., "Photocurrents generated by bacteriorhodopsin adsorbed on nano-black lipid membranes," *Biophysical Journal*, vol. 89, no. 2, pp. 1046–1054, 2005. ISI Document Delivery No.: 949XM Times Cited: 20 Cited Reference Count: 41 Biophysical society Bethesda.

[24] Jarrell, K., Bayley, D., and Kostyukova, A., "The archaeal flagellum: a unique motility structure.," *Journal of bacteriology*, vol. 178, no. 17, p. 5057, 1996.

[25] Jin, Y. D., Honig, T., Ron, I., Friedman, N., Sheves, M., and Cahen, D., "Bacteriorhodopsin as an electronic conduction medium for biomolecular electronics," *Chemical Society Reviews*, vol. 37, no. 11, pp. 2422–2432, 2008. ISI Document Delivery No.: 364AV Times Cited: 11 Cited Reference Count: 57 Jin, Yongdong Honig, Tal Ron, Izhar Friedman, Noga Sheves, Mordechai Cahen, David Feinberg Graduate School of the Weizmann Institute We thank the Ilse Katz Centre for Materials Research (MS, DC), the Helen and Milton A.

Kimmelman Center for Biomolecular Structure and Assembly (MS), the Nancy and Stephen Grand Centre for Sensors and Security (DC, YJ, IR), the Gerhard Schmidt Minerva Centre for Supramolecular Architecture (DC, YJ) and the historic generosity of the Perlman family. YJ thanks the Feinberg Graduate School of the Weizmann Institute for a postdoctoral fellowship. MS holds the Katzir-Makineni Chair in Chemistry. DC holds the Rowland and Sylvia Schaefer Chair in Energy Research. Royal soc chemistry Cambridge.

[26] Kelly, K., Coronado, E., Zhao, L., and Schatz, G., "The optical properties of metal nanoparticles: the influence of size, shape, and dielectric environment," *The Journal of Physical Chemistry B*, vol. 107, no. 3, pp. 668–677, 2003.

[27] Kuhlbrandt, W., "Bacteriorhodopsin - the movie," *Nature*, vol. 406, no. 6796, pp. 569–570, 2000.

[28] Kupper, J., Marwan, W., Typke, D., Grünberg, H., Uwer, U., Gluch, M., and Oesterhelt, D., "The flagellar bundle of halobacterium salinarium is inserted into a distinct polar cap structure.," *Journal of bacteriology*, vol. 176, no. 16, pp. 5184–5187, 1994.

[29] Kushner, D., Bayley, S., Boring, J., Kates, M., and Gibbons, N., "Morphological and chemical properties of cell envelopes of the extreme halophile, halobacterium cutirubrum," *Canadian journal of microbiology*, vol. 10, no. 3, pp. 483–497, 1964.

[30] Lanyi, J., "Bacteriorhodopsin," *Annu. Rev. Physiol.*, vol. 66, pp. 665–688, 2004.

[31] Lin, S. and Mathies, R., "Orientation of the protonated retinal schiff base group in bacteriorhodopsin from absorption linear dichroism.," *Biophysical journal*, vol. 56, no. 4, p. 653, 1989.

[32] Luecke, H. and others, "Atomic resolution structures of bacteriorhodopsin photocycle intermediates: the role of discrete water molecules in the function of this light-driven ion pump," *Biochimica Et Biophysica Acta-Bioenergetics*, vol. 1460, no. 1, pp. 133–156, 2000.

[33] Luecke, H., Richter, H. T., and Lanyi, J. K., "Proton transfer pathways in bacteriorhodopsin at 2.3 angstrom resolution," *Science*, vol. 280, no. 5371, pp. 1934–1937, 1998.

[34] Luecke, H., Schobert, B., Richter, H. T., Cartailler, J. P., and Lanyi, J. K., "Structural changes in bacteriorhodopsin during ion transport at 2 angstrom resolution," *Science*, vol. 286, no. 5438, pp. 255–260, 1999.

[35] Luecke, H., Schobert, B., Richter, H. T., Cartailler, J. P., and Lanyi, J. K., "Structure of bacteriorhodopsin at 1.55 angstrom resolution," *Journal of Molecular Biology*, vol. 291, no. 4, pp. 899–911, 1999.

[36] Mitchell, P., "Coupling of phosphorylation to electron and hydrogen transfer by a chemi-osmotic type of mechanism," *Nature*, vol. 191, no. 478, pp. 144–and, 1961.

[37] Nagy, K., "Photoelectric activity of dried, oriented layers of purple membrane from halobacterium halobium," *Biochemical and biophysical research communications*, vol. 85, no. 1, pp. 383–390, 1978.

[38] Nelson, D. and Cox, M., *Lehninger principles of biochemistry*. Wh Freeman, 2008.

[39] Neutze, R., Pebay-Peyroula, E., Edman, K., Royant, A., Navarro, J., and Landau, E. M., "Bacteriorhodopsin: a high-resolution structural view of vectorial proton transport," *Biochimica Et Biophysica Acta-Biomembranes*, vol. 1565, no. 2, pp. 144–167, 2002.

[40] Oesterhelt, D. and Stoeckenius, W., "Rhodopsin-like protein from the purple membrane of halobacterium halobium," *Nature*, vol. 233, no. 39, pp. 149–152, 1971.

[41] Oesterhelt, D. and Tittor, J., "Two pumps, one principle: light-driven ion transport in halobacteria," *Trends in biochemical sciences*, vol. 14, no. 2, pp. 57–61, 1989.

[42] Oetjen, H. F., Schmidt, V. M., Stimming, U., and Trila, F., "Performance data of a proton exchange membrane fuel cell using h-2/co as fuel gas," *Journal of the Electrochemical Society*, vol. 143, no. 12, pp. 3838–3842, 1996. ISI Document Delivery No.: VZ933 Times Cited: 289 Cited Reference Count: 17 Electrochemical soc inc Pennington.

[43] Ormos, P., Fábián, L., Oroszi, L., Wolff, E., Ramsden, J., and Dér, A., "Protein-based integrated optical switching and modulation," *Applied physics letters*, vol. 80, no. 21, pp. 4060–4062, 2002.

[44] PebayPeyroula, E., Rummel, G., Rosenbusch, J. P., and Landau, E. M., "X-ray structure of bacteriorhodopsin at 2.5 angstroms from microcrystals grown in lipidic cubic phases," *Science*, vol. 277, no. 5332, pp. 1676–1681, 1997.

[45] Rouhani, S., Cartailler, J., Facciotti, M., Walian, P., Needleman, R., Lanyi, J., Glaeser, R., and Luecke, H., "Crystal structure of the d85s mutant of bacteriorhodopsin: model of an o-like photocycle intermediate," *Journal of Molecular Biology*, vol. 313, no. 3, pp. 615–628, 2001.

[46] Roux, B., Nina, M., Pomès, R., and Smith, J., "Thermodynamic stability of water molecules in the bacteriorhodopsin proton channel: a molecular dynamics

free energy perturbation study," *Biophysical journal*, vol. 71, no. 2, pp. 670–681, 1996.

[47] Schobert, B., Cupp-Vickery, J., Hornak, V., Smith, S., Lanyi, J., and others, "Crystallographic structure of the k intermediate of bacteriorhodopsin: conservation of free energy after photoisomerization of the retinal," *Journal of molecular biology*, vol. 321, no. 4, pp. 715–726, 2002.

[48] Singhal, G., *Concepts in photobiology: photosynthesis and photomorphogenesis*. Springer, 1999.

[49] Smith, S., Courtin, J., Van den Berg, E., Winkel, C., Lugtenburg, J., Herzfeld, J., and Griffin, R., "Solid-state carbon-13 nmr of the retinal chromophore in photointermediates of bacteriorhodopsin: characterization of two forms of m," *Biochemistry*, vol. 28, no. 1, pp. 237–243, 1989.

[50] Song, L. and El-Sayed, M., "Primary step in bacteriorhodopsin photosynthesis: Land stretch rather than angle twist of its retinal excited-state structure," *Journal of the American Chemical Society*, vol. 120, no. 34, pp. 8889–8890, 1998.

[51] Sun, Y. and Xia, Y., "Shape-controlled synthesis of gold and silver nanoparticles," *Science*, vol. 298, no. 5601, pp. 2176–2179, 2002.

[52] Varo, G. and Lanyi, J., "Effects of the crystalline structure of purple membrane on the kinetics and energetics of the bacteriorhodopsin photocycle," *Biochemistry*, vol. 30, no. 29, pp. 7165–7171, 1991.

[53] Varo, G. and Lanyi, J., "Effects of hydrostatic pressure on the kinetics reveal a volume increase during the bacteriorhodopsin photocycle," *Biochemistry*, vol. 34, no. 38, pp. 12161–12169, 1995.

[54] Vogel, R. and Siebert, F., "Conformation and stability of alpha-helical membrane proteins. 2. influence of ph and salts on stability and unfolding of rhodopsin," *Biochemistry*, vol. 41, no. 11, pp. 3536–3545, 2002. ISI Document Delivery No.: 532JR Times Cited: 20 Cited Reference Count: 51 Amer chemical soc Washington.

[55] Vreven, T., Bernardi, F., Garavelli, M., Olivucci, M., Robb, M., and Schlegel, H., "Ab initio photoisomerization dynamics of a simple retinal chromophore model," *Journal of the American Chemical Society*, vol. 119, no. 51, pp. 12687–12688, 1997.

[56] Walter, J. M., Greenfield, D., and Liphardt, J., "Potential of light-harvesting proton pumps for bioenergy applications," *Current Opinion in Biotechnology*, vol. 21, no. 3, pp. 265–270, 2010. Walter, Jessica M. Greenfield, Derek Liphardt, Jan.

[57] Windle, W., "Neuropathology of certain forms of mental retardation," *Developmental Deficiencies: A Comparative Approach*, vol. 1, p. 75, 1973.

[58] Yen, C. W., Chu, L. K., and El-Sayed, M. A., "Plasmonic field enhancement of the bacteriorhodopsin photocurrent during its proton pump photocycle," *Journal of the American Chemical Society*, vol. 132, no. 21, pp. 7250–+, 2010. Yen, Chun-Wan Chu, Li-Kang El-Sayed, Mostafa A.

[59] Yen, C., Hayden, S., Dreaden, E., Szymanski, P., and El-Sayed, M., "Tailoring plasmonic and electrostatic field effects to maximize solar energy conversion by bacteriorhodopsin, the other natural photosynthetic system," *Nano letters*, vol. 11, no. 9, pp. 3821–3826, 2011.

[60] Zawodzinski, T. A., Derouin, C., Radzinski, S., Sherman, R. J., Smith, V. T., Springer, T. E., and Gottesfeld, S., "Water-uptake by and transport through nafion(r) 117 membranes," *Journal of the Electrochemical Society*, vol. 140, no. 4, pp. 1041–1047, 1993. ISI Document Delivery No.: KY388 Times Cited: 646 Cited Reference Count: 36 Electrochemical soc inc Pennington.

[61] Zhong, Q., Ruhman, S., Ottolenghi, M., Sheves, M., Friedman, N., Atkinson, G., and Delaney, J., "Reexamining the primary light-induced events in bacteriorhodopsin using a synthetic c-13= c-14-locked chromophore," *Journal of the American Chemical Society*, vol. 118, no. 50, pp. 12828–12829, 1996.

[62] Zhou, F., Windemuth, A., and Schulten, K., "Molecular dynamics study of the proton pump cycle of bacteriorhodopsin," *Biochemistry*, vol. 32, no. 9, pp. 2291–2306, 1993.

[63] Zimanyi, L., Varo, G., Chang, M., Ni, B., Needleman, R., and Lanyi, J., "Pathways of proton release in the bacteriorhodopsin photocycle," *Biochemistry*, vol. 31, no. 36, pp. 8535–8543, 1992.

CHAPTER V

PLASMONIC NANOPARTICLES IN THE PHOTODYNAMIC THERAPY OF CANCERS

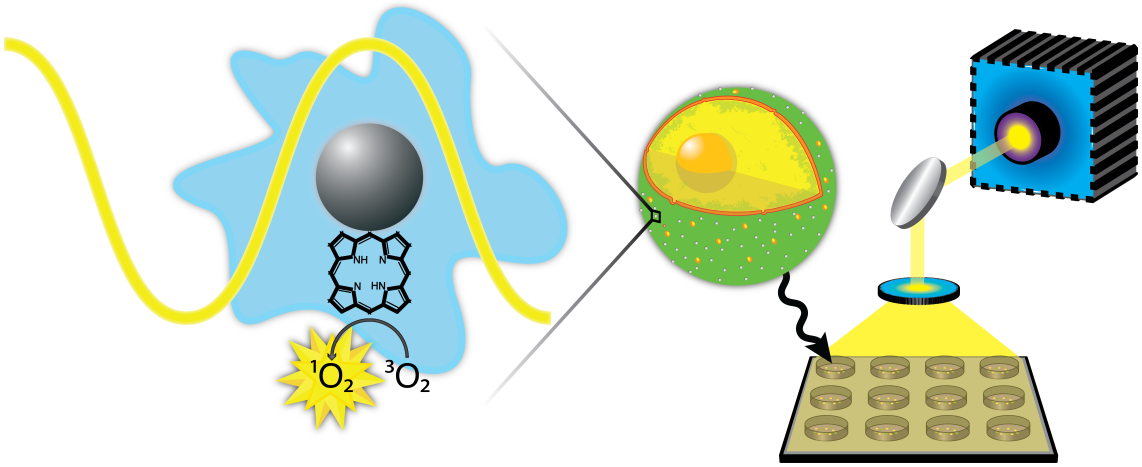

Figure 54: Schematic diagram of silver nanosphere, plasmon-enhanced porphyrin photosensitizer for photodynamic cancer cell therapy.

5.1 Chapter Summary

Photodynamic therapy has become a widespread treatment for a variety of cancers. The technique combines three non-toxic species - light, oxygen, and a photosensitizer (PS) - to excite molecular oxygen to its highly cytotoxic electronically excited singlet state. We demonstrate great enhancement of the in vitro efficacy of a model PS drug, protoporphyrin IX (PpIX), using plasmonic nanoparticles (NPs) both to deliver the drug and to plasmonically enhance the photo-processes involved. The role of plasmonic enhancement as well as unfavorable effects - such as d-band absorption, and radiative and non-radiative quenching - are investigated by controlling the overlap of the plasmon resonance with PpIX absorption bands using silver nanospheres, gold nanospheres, and gold nanorods.

All NP-PpIX complexes, including silver nanospheres, are shown to be non-toxic in the dark due to the lack of endocytosis. We decrease the amount of drug needed to provide significant cancer cell death by two orders of magnitude using silver nanospheres, whose plasmon resonance overlaps heavily with the main PpIX absorbance peak. Gold nanospheres, whose plasmon overlaps much more weakly with PpIX absorbance, decrease the amount of drug needed by one order of magnitude. Gold nanorods show negligible effect on drug activity; their plasmon overlaps spectrally with PpIX emission. Additionally, we vary the method of attachment of the drug to the nanoparticle using both reversible (electrostatic) and covalent attachment. Maximum enhancement of drug activity is shown to require the drug to remain bound close to the nanoparticle surface, where the electromagnetic field strength is highest. This plasmonic enhancement effect on drug activity is shown to surpass the amount of increase in efficacy seen when the nanoparticle ise used as a delivery vehicle, unloading the drug into the cell membrane. This NP delivery system illustrates an important application of nanotechnology to medicine, providing for reduced drug doses, reduced systemic toxicity, and a reduction in the amount of time the patient must spend in the dark following treatment.

5.2 History, Mechanism, and Uses of Photodynamic Therapy

Photodynamic therapy (PDT), in which light and molecular photosensitizers are used to treat cancers, has come to the forefront of cancer therapeutic options. This type of therapy offers a minimally invasive alternative to procedures like chemotherapy, radiation, and surgery, though it can also be used in conjunction with these [20]. PDT results in less cosmetic damage and less damage to underlying functional structures than other cancer therapeutic techniques, making it ideal [2] and currently prevalent [29] for cancers of the skin, head, and neck. The advent of endoscopic delivery of light has rendered PDT a successful method of treatment for internal cancers as well, such

as the bladder, lungs [29] and gastrointestinal tract [20].

First employed in ancient Egypt [14], the modern-day version of the technique was established in the early 1900s [2], when it was observed that large macrocyclic organic compounds, or photosensitizers, were capable of producing highly cytotoxic effects under low levels of visible radiation [45]. The reactive species responsible for this effect was later shown to be singlet oxygen ($^1O_2$) [12], an unstable electronic excited state of molecular oxygen in the same quantum state as most ground state molecules [44]. This renders it highly reactive and thus highly destructive in a cellular environment. However, power has limits; the lifetime of this excited state is quite short in solution - less than 40 ns [7]. This limits the diffusion pathlength to only 20 nm, an applicative boon for PDT, as it effectively confines the reactive oxygen species to the local area where the PS is sequestered [19]. Further, macrocycles commonly used for PDT have very little cytotoxicity in the dark, which allows for clinicians to further localize photodynamic treatment via selective delivery of light. [20, 29]

5.3 Macrocycles as PDT Drugs

Porphyrins, phthalocyanines, and related compounds have become the most studied class of molecules for application as photosensitizers in the photodynamic therapy of cancers [45, 46]. These compounds provide a simple and controllable method of $^1O_2$ production that requires only: oxygen, the PS molecule, and light of an appropriate wavelength to excite the PS (Figure 55) [12]. The reaction of $^1O_2$ with allylic olefins, such as tryptophan [1], histadine [1], and unsaturated fatty acids [41], to generate an allylic hydroperoxide is of particular interest due to the prevalence of these compounds in biological systems [12]. Desireable properties in a PS include: high triplet state quantum yield and lifetime, high $^1O_2$ quantum yield, high specificity for the target tissue, and good water solubility [37].

Photosensitizer selection is also based on the region of treatment. The so-called

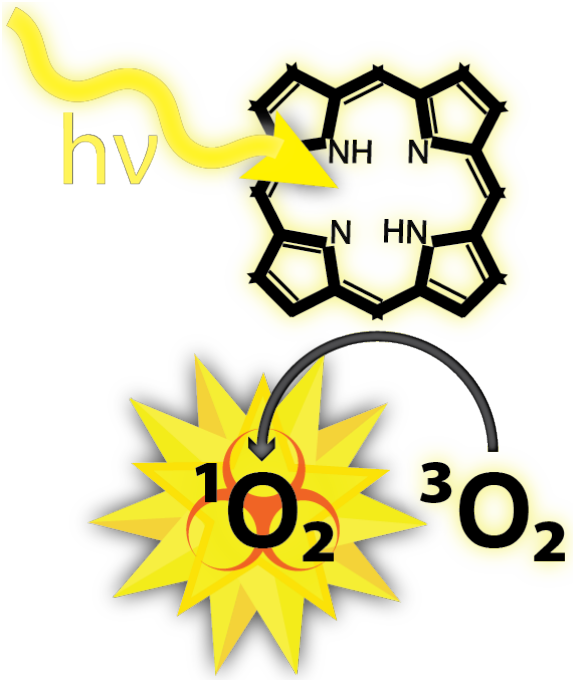

Figure 55: Schematic rendering of $^1O_2$ production mechanism by a porphyrin photosensitizer under irradiation.

therapeutic window (ca. 600 - 900 nm) results from the fact that hemoglobin, water, and other tissue components have relatively strong extinction cross sections for blue light and relatively weak extinction cross sections in the NIR (Figure 56). [6] This means that blue light shows only shallow tissue penetration, whereas red light can penetrate several centimeters into tissues. Thus, blue light absorbers are useful for epithelial-depth and post-surgical PDT [20, 29, 28], and NIR absorbers are useful for deep tissue and solid tumor PDT [15, 14, 46].

While porphyrins and phthalocyanines have excellent triplet state quantum yields and lifetimes as well as high $^1O_2$ quantum yields, these large macrocycles suffer from inherent hydrophobia. This trait is beneficial in that it leads these molecules to sequester in the lipophilic membranes of cells, where they are most effective [20]. However, this hydrophobia is a major limitation to the circulation half-lives and activities of these drugs [4], as they aggregate relatively quickly in biological serum [46]. Yet another limitation to the use of these drugs is their dependence on passive

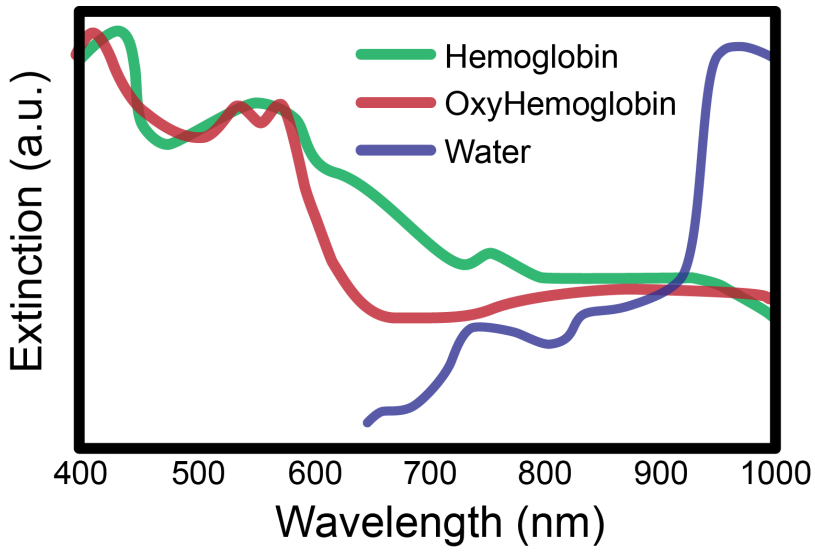

Figure 56: Extinction profile of hemoglobin (green), oxy-hemoglobin (red), and water (blue). Illustrates the increased permeability of tissues to red light (600 - 900 nm).

targeting; when administered systemically, they accumulate in tumors merely due to the enlarged vasculature and lack of lymphatic drainage therein [14].

5.4 Platforms for PDT Drug Delivery

Significant attention has been given to PDT drug administration platforms. Of these, polymeric particles [4], liposomes [23, 13], and metal nanoparticles (NP) are the most promising.

5.4.1 Polymeric Particles and Liposomes in PDT

Polymeric particles and liposomes are both useful for extending the circulating half-lives of PDT drugs in serum [42, 39], and both have shown enhanced efficacy in cancer therapy via selective delivery of PDT drugs to tumor tissue through ligand targeting [30, 48] or through temperature, light, or pH sensitivity [13, 4]. Conferring cancer-cell-specific targeting ability on PDT drugs greatly reduces their systemic toxicity as well as decreases their required dosage [4]. Polymeric particles and liposomes also greatly increase the activity of these drugs by increasing their overall solubility in serum [4]. However, beyond regio-specific drug transport, these administration platforms have

little effect on the activity of the drugs.

5.4.2 Plasmonic Nanoparticles in PDT

Plasmonic nanoparticles provide all of the listed benefits of polymeric particles and liposomes [8], and they also possess the ability to increase the absorption - and therefore anticarcinogenic activity - of photosensitizer drugs [17]. Plasmonic enhancement of PS activity results from favorable overlap between the localized surface plasmon resonance extinction band and the PS absorption band [38]. This enhancement should allow for either: 1) the administration of smaller doses of drug, which will further reduce systemic toxicity, or 2) for less intense or shorter periods of light exposure, a major concern during post-surgical PDT when the patient is anesthetized [31].

Nanoparticles have received a great deal of attention for use as drug delivery systems [8]. With the first pthalocyanine (P_c) stabilized synthesis and characterization of gold nanoparticles, Hone et al. observed an increase in singlet oxygen quantum yield for the permanently-bound gold-P_c complex versus free P_c [16]. Cheng et al. investigated a modified version of this system that exploited both 1) polyethylene glycol to increase biocompatibility by decreasing protein adsorption and 2) attachment of the PS to the NP surface using weaker, electrostatic interations [10]. This electrostatic association of PS to NP provided for passive release of the drug directly into the lipophilic environment of the cell membrane and showed increased efficacy *in vitro* versus free P_c.

One added asset of plasmonic nanoparticles versus other platforms is the potential for photothermal therapy (PTT) provided by the introduction of the nanoparticle. [21, 22] This was recently addressed by Jang et al. using a gold nanorod-photosensitizer complex to provide a combination of photodynamic and photothermal therapies. [27] This system exploited the plasmon resonance of the gold nanorods to

keep the photosensitizer drug quenched during delivery. After incubation and subsequent diffusion of the drug off the AuNR surface, the drug was again active. Subsequent irradiation with light exploited the photodyanmic therapeutic effects of the photosensitizer as well as the photothermal therapy provided by the gold nanorod delivery vehicles to achive greater cancer cell death than either treatment provided alone. This PDT/PTT combination system is important conceptually in that it further exploits the delivery vector to provide direct therapy.

Plasmonic particles are unparalleled in their ability to harvest light energy [11, 25]. However, the constructive use of this light-harvesting ability to enhance radiative processes in adjacent systems (e.g. photosensitizers) is strongly dependent on the particle characteristics (e.g. size, shape, composition), as these determine the optical properties of the nanoparticle [24]. In most studies that employ a plasmonic nanoparticle as the delivery platform, the neccessity of dissociation of the PS from the nanoparticle surface is emphasized [10, 27], as these particles generally have plasmon resonances in the region where photosensitizers emit. This leads to quenching of PS activity [38, 43, 40]. Very recently, Khaing et al. examined a system employing gold nanospheres and protoporphyrin IX (PpIX) [32]. These nanoparticles possess a plasmon resonance that overlaps partially with the PS absorbance and not with its emission; an increase in singlet oxygen generation (SOG) was observed with increasing particle plasmon strength.

Absorption of light by a metal nanoparticle occurs either by excitation of d orbital transitions, called the interband transitions, or through interaction with the plasmon resonance. This is discussed in detail in Chapter 1. Briefly, absorption by the interband invariably results in thermal or other non-radiative relaxations and is thus non-advantageous for this system. Interband transitions are a property of the metal; they cannot be adjusted by changing particle size or shape. All gold particles will therefore show some degree of competitive filtering of UV to green light, as their

interband transitions are in this region, whereas silver interband transitions are in the UV. Excitation of the plasmon, on the other hand, should increase the absorption - and therefore emission and SOG - of photosensitizers on the particle surface, given spectral overlap between the plasmon and the PS absorption. The ability to tune the plasmonic resonance of nanoparticles throughout the visible energy spectrum is a defining and highly important characteristic of these systems and is an area our lab has explored in depth [36, 5, 34, 24, 35, 25, 26, 49]. Given that plasmon resonance results in such a strong interaction with incident photons, it follows that proper manipulation of the plasmon energy will allow for unparalled enhancement of photosensitizers within the NP plasmonic field [38, 9, 17].

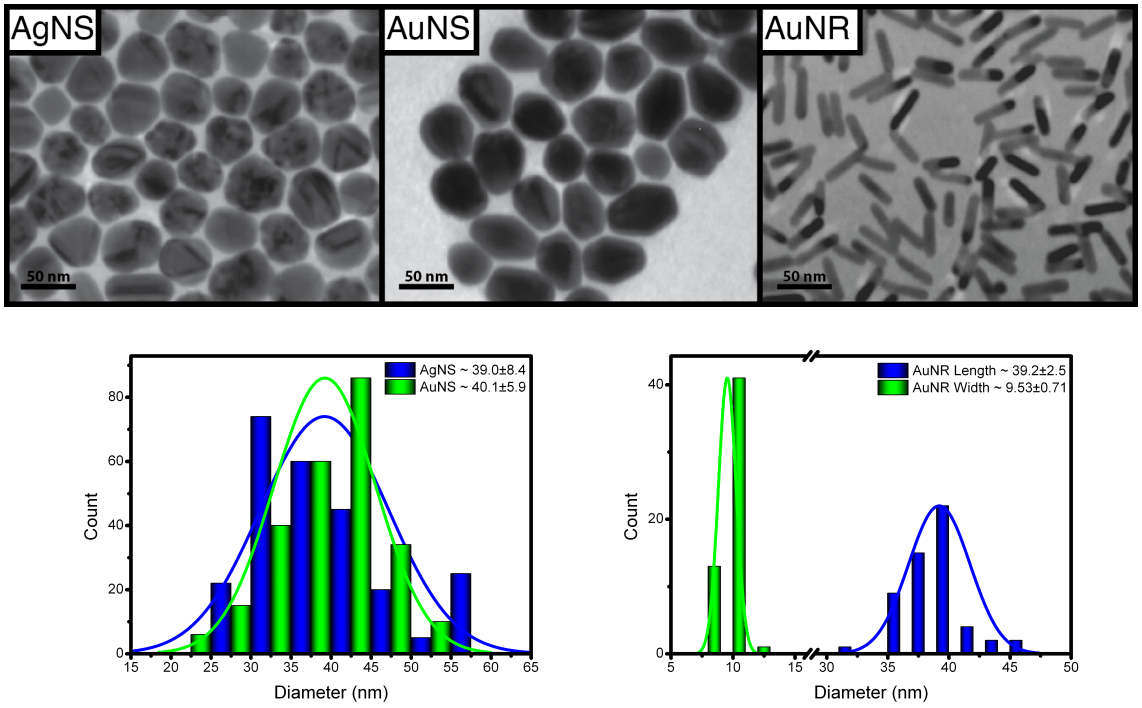

Figure 57: TEM micrographs of AgNS, AuNS, AuNR (top) and their corresponding histograms of particle dimensions measured via TEM for AgNS (bottom left, blue), AuNS (bottom left, green), and AuNR legnth (bottom right, blue) and width (bottom left, green).

In the following sections, we systematically examine the role of overlap between the energy of the plasmon and the absorption and emission of a model porphyrin

photosensitizer (Protoporphyrin IX, PpIX, Figure 58) using silver nanospheres (40 nm diameter, AgNS), gold nanospheres (40 nm diameter, AuNS), and gold nanorods (40 nm length, 10 nm width, AuNR). The micrographs and histograms for these particles are shown in Figure 57.

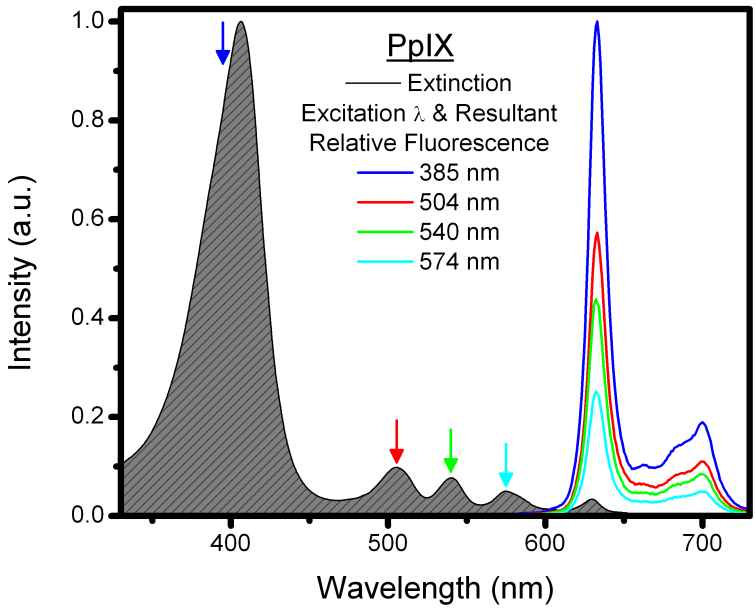

Figure 58: Absorption (grey) and emission of PpIX when excited at 385 nm (blue), 504 nm (red), 540 nm (green), and 574 nm (cyan). Relatively weaker absorption cross-sections result in correspondingly weaker emissions.

The combination of these systems, depicted in Figure 59, provides a cohesive survey of plasmonic enhancement, competitive filtering, and emission quenching of this model PS by these characteristic plasmonic nanoparticles. In addition, we vary the nature of PpIX association with the particle surface to illustrate both the unloading ability generally presented in the literature using electrostatic complexes and the plasmonic effect on PpIX activity using rigid surface attachment. Further, we vary the distance between the porphyrin and the particle surface in our covalently-attached complexes to judge the effect of non-radiative energy transfer processes for each of our three nanoparticle types.

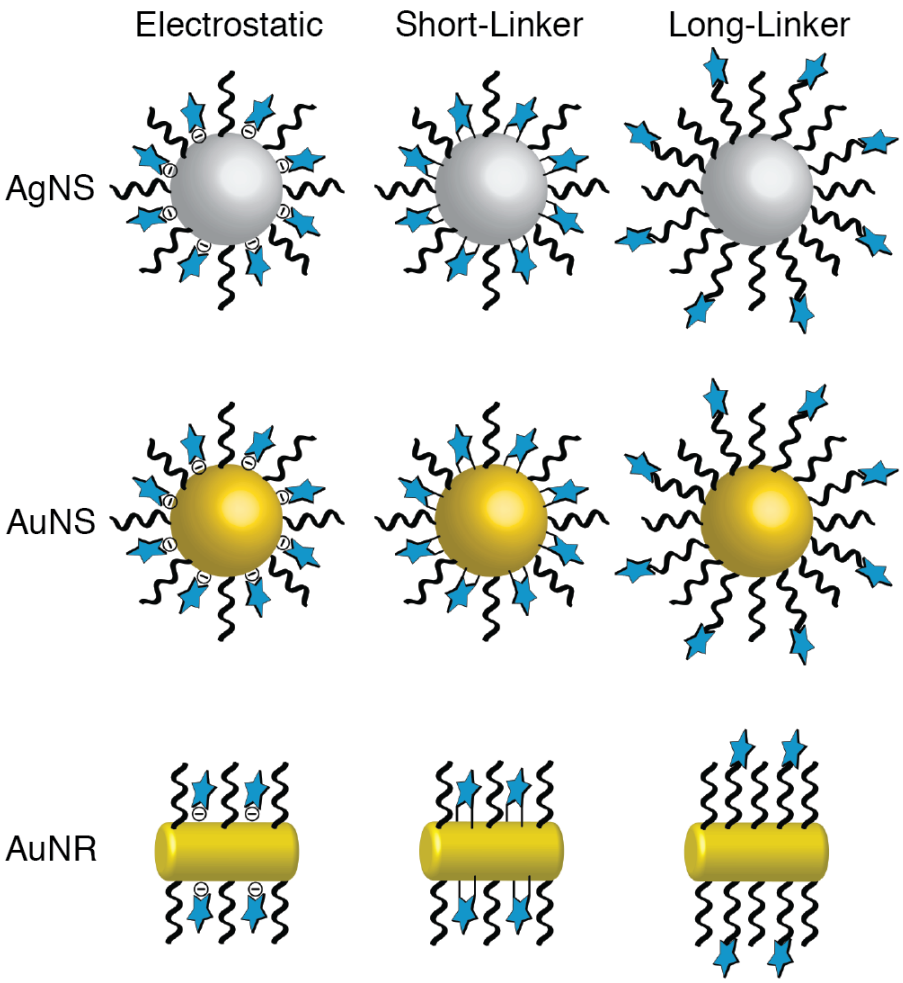

Figure 59: Schematic diagram of AgNS, AuNS, and AuNR complexes with PpIX (blue star) showing the three conjugation methods used. PEG is represented in black.

5.5 Modification of Protoporphyrin IX for Complexation with Plasmonic NPs

PpIX is easily modified through a series of peptide bond couplings to generate thiol-functionalized derivatives of the drug without compromising its spectral characteristics or photodynamic activity (Figure 60 &63, Appendix D). The addition of this thiol modality allows for the facile, stable attachment of PpIX to a gold or silver nanoparticle surface due to the relatively strong nature of gold-thiol and silver-thiol bonds.

We first examined the unmodified PpIX in an electrostatic complex with NPs. In

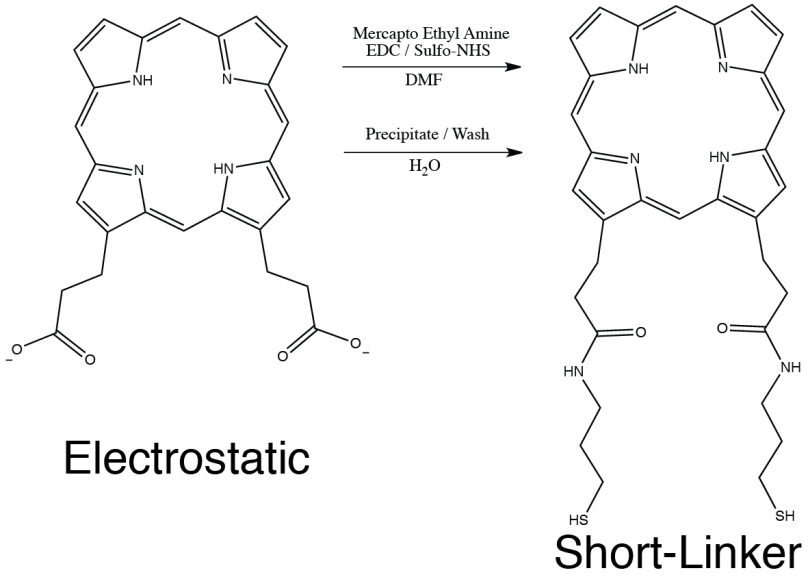

Figure 60: Synthesis of HS-PpIX used to generate Short-Linker NP-PpIX complexes.

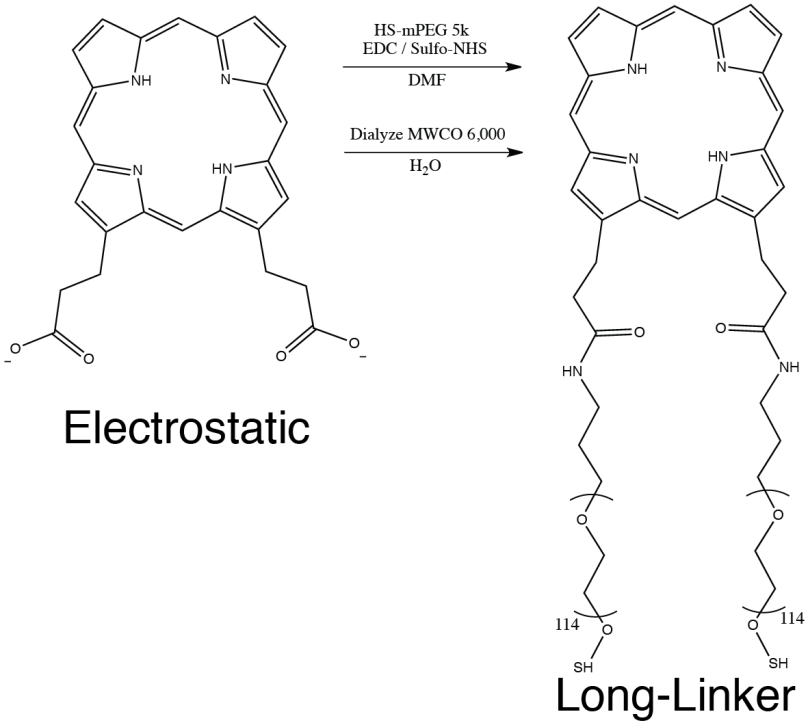

Figure 61: Synthesis of HS-PEG-PpIX used to generate Long-Linker NP-PpIX complexes.

the second case, we modified PpIX with a peptide bond to yield Short-Linker PpIX with a thiol terminus (Figure 60). In the third, we functionalized PpIX with a PEG-thiol to generate Long-Linker PpIX, with a larger distance between the fluorophore

and the NP surface (Figure 61). Figure 63 shows the spectral extinction characteristics of stable complexes between PpIX (grey) and AgNS (blue), AuNS (green), and AuNR (red), and schematic renderings of these are presented in Figure 59.

5.6 Nanoparticle Selection: Achieving Maximum Spectral Overlap between Plasmon Resonance and Drug Absorption

Three types of plasmonic nanoparticles were chosen to investigate the effect of these on singlet oxygen generation (SOG) and cancer cell death by protoporphyrin IX (PpIX): AgNS, AuNS, and AuNR (Figure 57). We maintained similar hydrodynamic radii (Figure 62) to eliminate error from differences in cellular uptake.

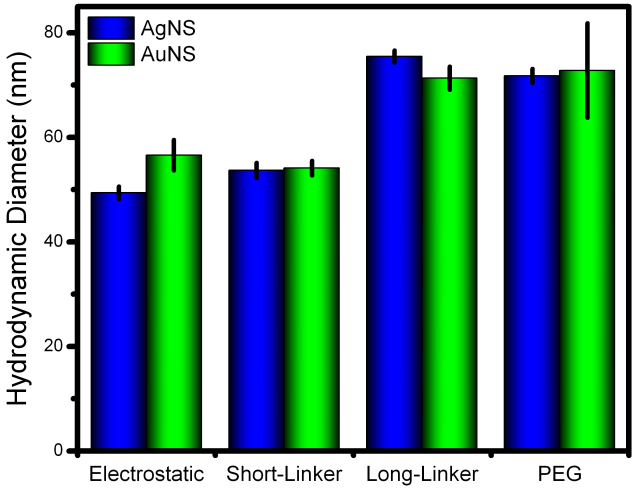

Figure 62: Hydrodynamic diameter of AgNS (blue) and AuNS (green) Electrostatic, Short-Linker, Long-Linker, and PEG-conjugated complexes as determined via dynamic light scattering.

5.6.1 Silver Nanosphere Complexes with PpIX

Plasmon resonance interacts constructively to yield an increase in PpIX absorption, given proper spectral overlap between the plasmon resonance and the PpIX

absorbance. AgNS have a strong plasmon resonance in the blue wavelength region (ca. 400 nm) where the Soret band absorbance of the PpIX lies (Figure 63, blue).

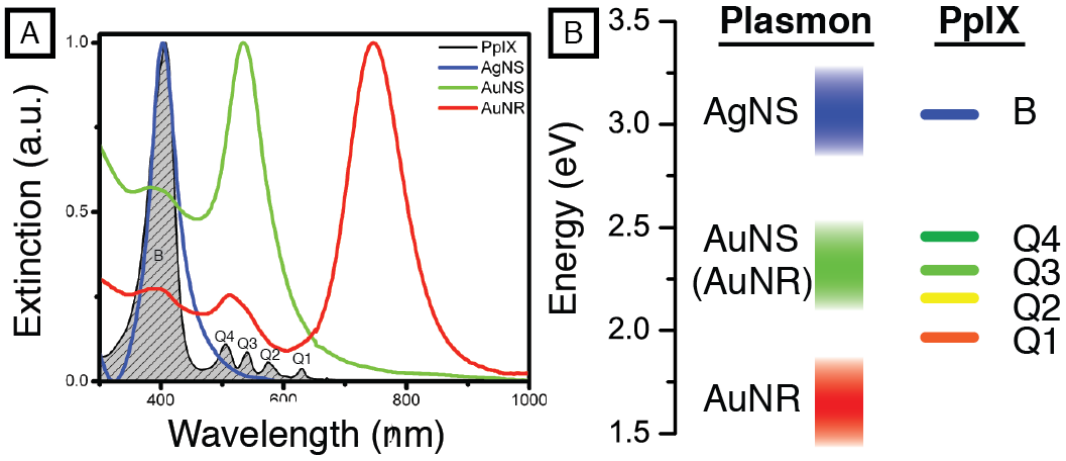

Figure 63: NP and PpIX physical and energetic characteristics. (A) Extinction spectrum of PpIX (shaded grey), AgNS (blue), AuNS (green), and AuNR (red). (B) Jablonski diagram of plasmon resonances for each particle and the Q and B excitation bands of PpIX, illustrating the overlap between the various plasmon resonances and these PpIX excitation energies. Note that the energy of the transverse plasmon mode arising in AuNR gives this resonance a degree of overlap with the Q band excitation energies similar to - but weaker than - that seen in AuNS.

The interband transitions of silver are in the ultraviolet and are therefore moot in this visible-light system. These AgNS particles should therefore show the strongest enhancement of PpIX absorption with no competitive filtering by d-d transitions.

5.6.2 Gold Nanosphere Complexes with PpIX

In contrast to silver, the gold interband absorbs from the UV into the green spectral region and will thus function as a competitive filter of the incident excitation energy in this region. AuNS possess a plasmon resonance that overlaps with the Q band absorptions in PpIX (ca. 530 nm, Figure 63, green). This resonance is weaker in intensity than that seen in AgNS (Figure 64) but will still lead to enhancement of said absorptions. Excitation of these transitions also results in emission and singlet oxygen production, though the emission is correspondingly weaker (Figure 58).

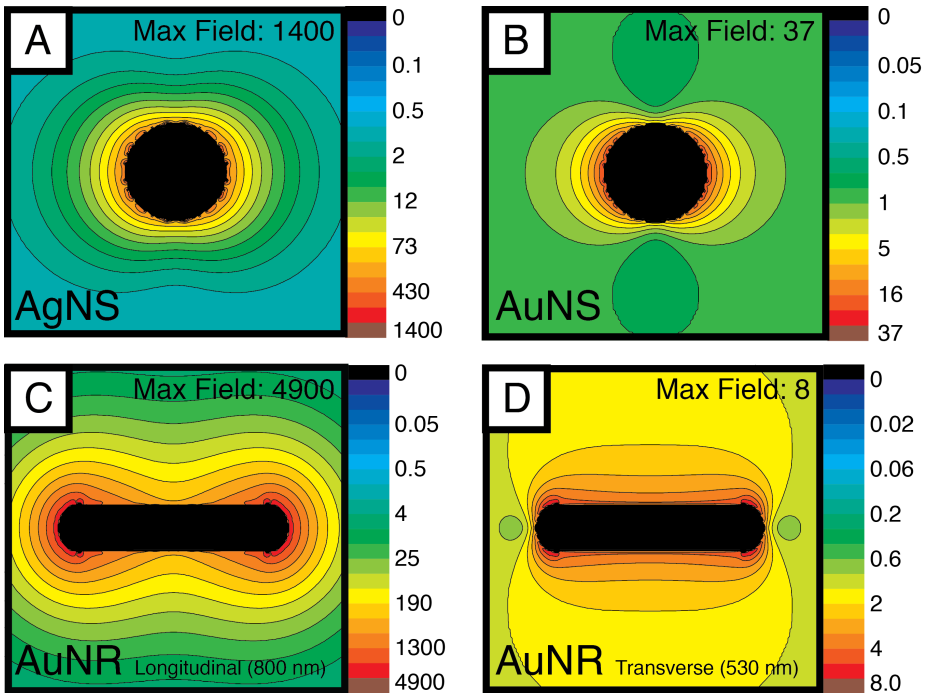

Figure 64: Discrete dipole approximation electric field plots for (A) AgNS at 412 nm, (B) AuNS at 530 nm, and AuNR for both the (C) longitudinal plasmon mode at 800 nm and (D) the transverse plasmon mode at 530 nm. Maximum field strengths are indicated for each resonance.

5.6.3 Gold Nanorod Complexes with PpIX

Gold nanorods have a strong longitudinal plasmon resonance in the therapeutic window (800 nm, Figure 63, red, Figure 64C). However, the emission of most photosensitizers is also in this region, and this leads to quenching of the emission and SOG of bound photosensitizers. [27] AuNR also show a weak surface plasmon resonance in the green, corresponding to the excitation of their transverse plasmon mode (ca. 530 nm, Figure 64); the energy of this oscillation will provide some enhancement of PS molecules along the sides of the rod.

In summary, we observe: 1) plasmonic enhancement of PpIX absorption for AgNS-PpIX complexes; 2) competitive interband filtering of PpIX Soret band excitation energy and plasmonic enhancement of PpIX absorption in the case of AuNS-PpIX complexes; and 3) interband filtering, plasmonic enhancement of PpIX absorption,

and emission quenching in the case of AuNR-PpIX complexes. All of these complexes have the advantage that they will increase the solubility of PpIX in biological media. Each of these was prepared at a constant concentration of NPs and varied concentrations of PpIX.

5.7 Enhanced Photoexcitation Allows for the Use of 200 Times Less Drug

5.7.1 Cytoxicity of PpIX and NPs Independently

We treated human oral squamous carcinoma cells (HSC-3) with NPs alone and with PpIX alone over a wide range to concentrations in order to determine the concentration at which each became toxic to the cells on their own. For the NPs, this was ca. 1 nM, and for the PpIX, this was ca. 20 μM. Thus, we proceeded forward with NP-PpIX complexes in which the concentration of each species was at least an order of magnitude lower than these toxic concentrations (0.1 nM NPs and 0.2 - 2.0 μM PpIX). Figure 66 shows the lack of toxicity of the PEG-passivated NPs at these concentrations, and Figures 66 (top) show the lack of toxicity for PpIX at 0.2 μM (left) and 2.0 μM (right).

5.7.2 Cytoxicity of Short-Linker NP-PpIX Complexes

Whereas PpIX began to show some cytotoxic effect (ca. 30% cell death) at a concentration of around 20 μM (Figure 67, black), plasmon-enhanced, Short-Linker AgNS-PpIX began to show show cytotoxicity at as low as 0.2 μM under the same exposure and treatment conditions (Figure 67, blue). This represents a factor of 200 less drug than PpIX alone. Further, the AgNS-PpIX complexes yield significantly higher cell death at this concentration (60% cell death, Figure 67, blue). Short-Linker AuNS complexes show activity at 2 μM (Figure 67, green), still an order of magnitude lower than the free drug.

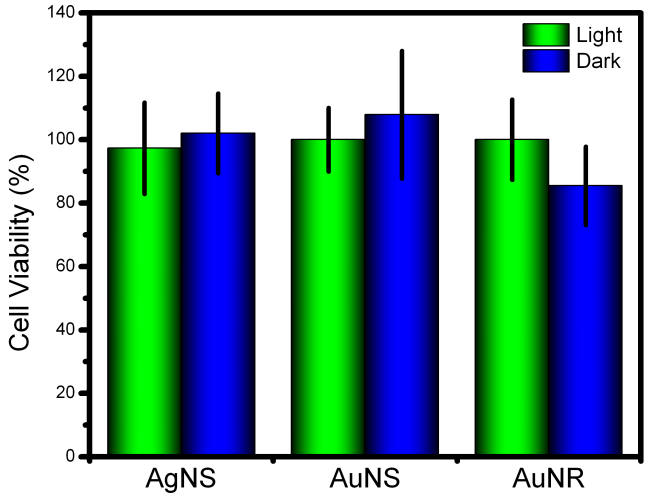

Figure 65: Viability of cells treated with mPEG-conjugated 0.1 nM AgNS, AuNS, and AuNR alone in the absence of PpIX for cells that received photodynamic treatment (green) and cells left in the dark (blue). This concentration of NPs caused no cell death on its own with or without light treatment, and no dark toxicity of the complexes was observed.

5.7.3 Cytoxicity of Electrostatic NP-PpIX Complexes

We observed decreased activity for the Electrostatic NP-PpIX complexes relative to the Short-Linker complexes, which corroborates the *in situ* results presented forthwith. Electrostatic AgNS-PpIX showed ca. 12% less activity compared to their Short-Linker counterparts, whereas Electrostatic AuNS-PpIX showed negligible activity versus Short-Linker AuNS-PpIX. This is a result of unloading of the drug from the NP surface during the 24-hour incubation period of cells with the complexes, [10, 27] as ions in the biological medium destabilize the electrostatic association between the PS and NP. This effect is more pronounced in gold complexes versus silver because PpIX is electrostatically coordinated to the NP surface through its carboxylic acid groups, and the strength of metal-carboxylic acid interaction is stronger for silver than for gold. [18, 47] Thus, PpIX unloads more readily from gold than from silver, and the AgNS-PpIX Electrostatic complexes retain more plasmonic enhancement and

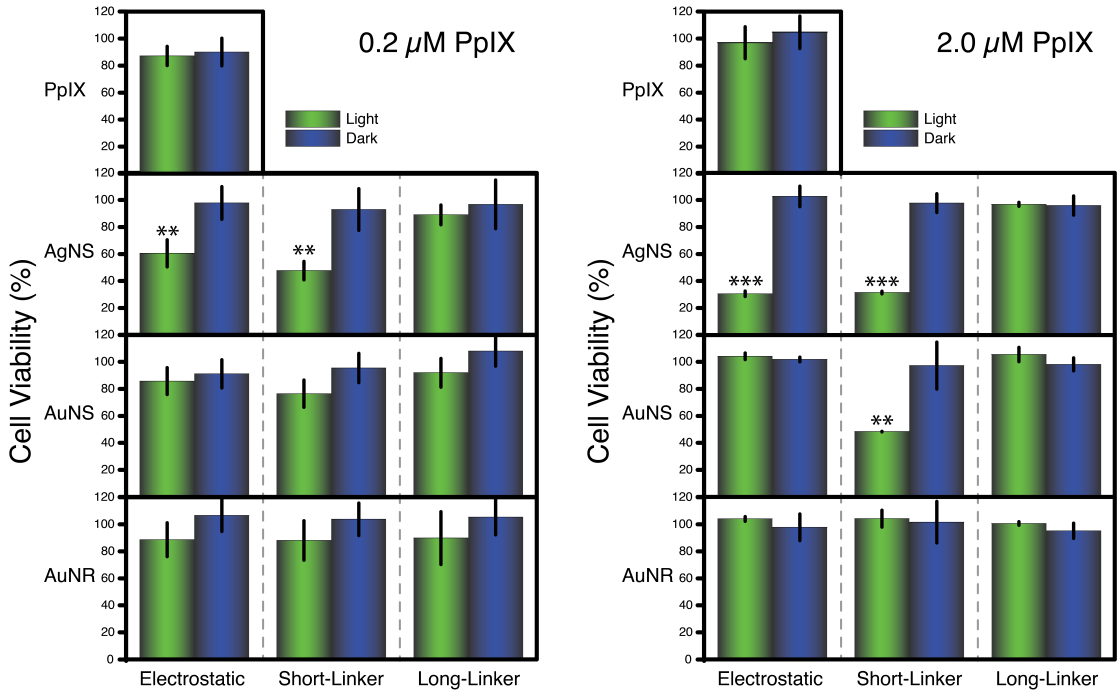

Figure 66: Cell viability of HSC-3 cancer cells treated with free PpIX and PpIX conjugated to AgNS, AuNS, and AuNR via Electrostatic, Short-Linker, and Long-Linker conjugation at 0.2 μM (left) and 2.0 μM (right) PpIX concentration in cells that received photodynamic treatment (green) and cells that were kept in the dark (blue). Illustrates the lack of NP-PpIX toxicity in the dark.

cause more cell death from residual drug left on the NP surface relative to AuNS-PpIX Electrostatic complexes. *In situ* experiments monitoring the diffusion of PpIX drug from NP-PpIX Electrostatic complexes in water into toluene[10] confirm that almost all of the drug is unloaded from the gold surface compared to only ca. 10% unloaded from silver (Figure 68).

Unloading of the drug is advantageous from a solubility standpoint, as the particle helps transport the PpIX close to the cell membrane where the drug sequesters in the lipophilic membrane. [20] However, these delivery and solubility benefits do not outstrip the enhancement effect seen in the Short-Linker complexes, as these maintain plasmonic enhancement of the drug.

5.7.4 Cytoxicity of Long-Linker NP-PpIX Complexes

Toxicity was not observed for Long-Linker NP-PpIX complexes (Figure 67) due to the decreased plasmon field strength away from the NP surface. In all of these experiments, we observed a leveling-off of cell death percentage even with further increased concentrations of PpIX. We attribute this to an exhaustion of the available oxygen in the cell medium under these conditions, an issue that could be easily resolved in a clinical setting by maintaining an oxygen flow over the treatment area.

5.8 NP-PpIX Complexes Remain in the Extracellular Environment; AgNS-PpIX Show Surprising Lack of Dark Toxicity

Without a ligand that triggers endocytosis, these NP-PpIX complexes remain in the extracellular environment. This is likely due to their size - ca. 60 - 70 nm hydrodynamic diameter (Figure 62). Dark field analysis of cells following 24h incubation with our NP-PpIX complexes shows negligible internalization of the particles (Figure 69), suggesting that cell death is induced by cell membrane damage. [33] Furthermore, HSC-3 cells display morphological signs of apoptosis following treatment with light and our NP-PpIX complexes; visible cell shrinkage is apparent when compared to NPs conjugated with PEG.

5.9 In situ Quantification of NP-PpIX Photodynamic Potential

Singlet oxygen generation was measured using a scavenger molecule, 9,10 - Anthracenediyl - bis(methylene) dimalonic acid (ABDA), whose absorbance shifts from the visible to the UV upon reaction with $^1O_2$ (Figure 70).

As AMBA photobleaches fairly rapidly when irradiated with light of < 400 nm, a long-pass filter was used to block this region of the spectrum (Figure 71). SOG rate constants were determined for each modified PpIX alone and for each AuNS-PpIX

and AuNR-PpIX complex. All NP-PpIX complexes showed enhanced SOG relative to PpIX alone, with the Short-Linker method of attachment (Figure 5, green) providing the best enhancement for both AuNS and AuNR.

Overall, the results from the *in situ* and *in vitro* studies are mutually reinforcing. Electrostatic AuNS-PpIX complexes showed significantly less overall enhancement relative to their Short-Linker counterparts (Figure 72, red), a likely result of PpIX detachment from the particle surface over the course of the experiment. This was demonstrated previously in Figure 68 and illustrates that the increased activity for the Electrostatic NP-PpIX complexes observed in the cell studies is due largely to vectorial transport of PpIX to the cell membrane by the NP rather than plasmonic enhancement of the porphyrin. Greater enhancement of SOG is seen in AuNS-PpIX versus AuNR-PpIX for Short-Linker and Electrostatic conjugations.

5.9.1 Generation of Silver Plasmon Resonance is Precluded by the Filter

AgNS-PpIX showed comparable activity to free PpIX due to the filter used in this experiment, which keeps the detector molecule from photobleaching but also prevents excitation of the AgNS plasmon. This illustrates the role of plasmon resonance in enhancement.

5.9.2 Singlet Oxygen Generation by AuNS-PpIX Complexes

For AuNS in complex with PpIX, the greatest enhancement is seen for the Short-Linker complexes, where the PpIX is bound close to the NP surface. Long-Linker AuNS-PpIX complexes show the least enhancement of SOG relative to the other complexes (Figure 72) due to the distance between the particle surface and the PpIX, as the electromagnetic field becomes exponentially weaker farther out from the NP surface.

5.9.3 Singlet Oxygen Generation by AuNR-PpIX Complexes

Interestingly, Long-Linker AuNR-PpIX complexes showed increased activity relative to AuNS-PpIX particles with the same conjugation. We postulate that this effect arises from the arrangement of this PEG-modified PpIX on the surface of the particle. Thiol groups favor attachment to the crystal surface located at the ends of gold nanorods versus those along the sides. [32] This allows for these PpIX, at the end of a relatively long, malleable polymer chain, to locate preferentially along the sides of the rod, though their thiol tails are attached to the nanorod ends. As illustrated in Figure 63, the plasmon band resulting from the transverse plasmon oscillation corresponds to the peak at ca. 530 nm, and this oscillation would show similar plasmon enhancement of PpIX activity as that seen in gold spheres, though its intensity is much weaker than that of a gold sphere (Figure 64). Thus, slight enhancement of PpIX activity results here from localization of the actual PpIX moiety away from the unfavorable, emission-quenching longitudinal plasmon resonance and closer to the favorable, transverse plasmon oscillation.

5.10 Concluding Remarks

We have used the photo-enhancement properties of plasmonic nanoparticles to concentrate the exciting light locally, allowing for a reduction in the amount of PS drug needed for PDT. The ability of plasmonic nanoparticles to enhance the singlet oxygen generation of this model PS drug is greatly dependent on the extent of spectral overlap between the drug absorption and the NP plasmon resonance band. These important concepts will be essential to the design and use of NP conjugates as platforms for the delivery and enhancement of PS drugs in cancer treatment applications.

We found that the strongest enhancement of photosensitizer activity occurs when the drug is covalently bound close to the spherical nanoparticle surface, where the strong plasmonic field maximizes the drug excitation process. Results from *in vitro*

experiments show that the amount of drug needed to achieve significant cancer cell death is reduced by two orders of magnitude for silver nanosphere-drug complexes and by one order of magnitude for gold nanosphere-drug complexes. The use of a NP platform both increases the solubility of the photosensitizer and enhances its quantum efficiency. The NP platform also provides the opportunity to introduce targeting ligands to the system, an advantage that our lab is now exploring. This will greatly increase the specificity of these complexes to target cancerous cells preferentially over healthy cells.

We postulate that the NPs either increase the overall absorption efficiency of PpIX or that the NPs transfer energy to the PS molecules. The NP-PS complex thereby increases the quantum yield of singlet oxygen production by the PS drug. These complexes are not endocytosed by the cell; this allows for the use of silver NPs without the toxicity that has been observed in other studies when silver NPs are endocytosed. [3] This further suggests that the complexes could be removed easily if used for surface treatment. However, should future *in vivo* experiments reveal dark toxicity of silver NP-PS complexes, gold NP-PS complexes, known for their lack of *in vivo* toxicity, could be used instead. This opens the door for the use of other nanoparticle shapes, such as cubes, which are known to have stronger fields and may therefore yield even greater enhancement of PS activity. The shape-dependence of this enhancement is now being explored in our lab.

A limitation to the use of these NP complexes in the body arises from the poor tissue penetration depth of the visible light needed to excite these silver or gold nanospheres, which could limit the use of these complexes to surface treatments. Tissue penetration depth in the red is quite high, but NPs with plasmon resonance in the red quench the emission and activity of PS molecules bound to their surface, as this emission is also in the red. Further, the energy required to generate singlet oxygen precludes both direct excitation of molecular oxygen[47] and the use of a drug

with an absorbance in the red, as this might bathochromically shift the energy of the PS triplet state below that needed to generate singlet oxygen (unless a drug could be designed with small singlet-triplet separation). However, currently used drugs and silver or gold nanospheres could potentially be employed for PDT in deeper tissues through the use of a red pulsed laser doubled at the cancer location[18] to provide the visible light needed to excite the drug-nanoparticle complexes in the tumor.

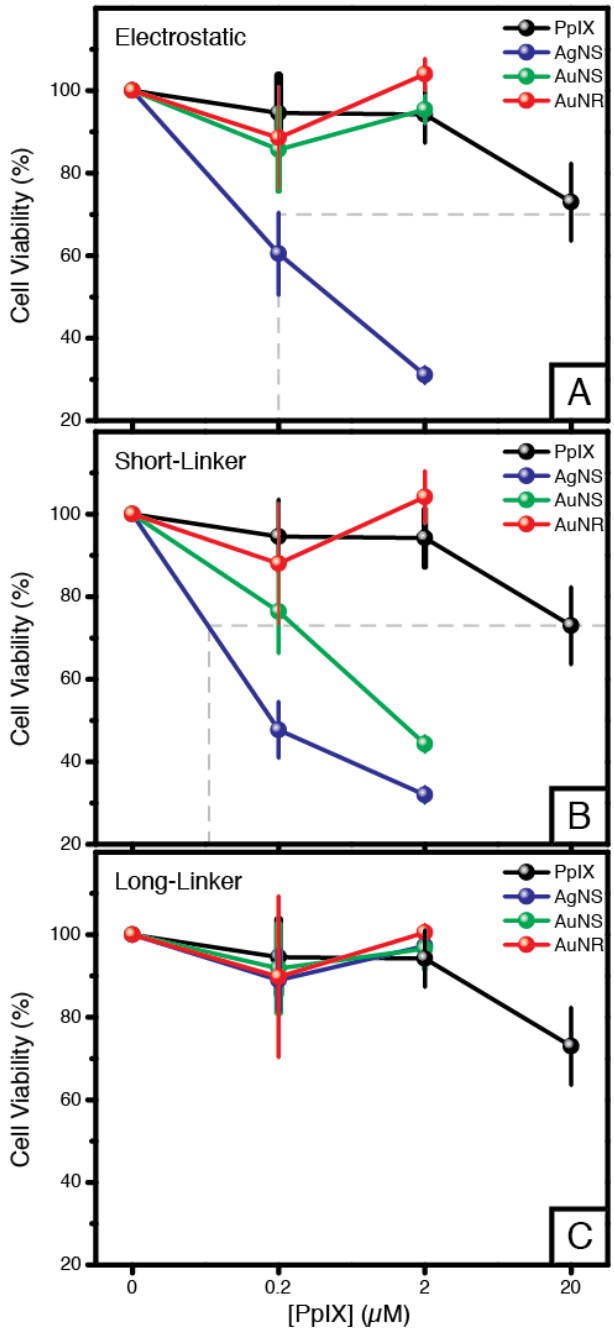

Figure 67: Cell viability data of HSC-3 cancer cells treated with free PpIX (black) and PpIX conjugated via Electrostatic, Short-Linker, and Long-Linker to AgNS (blue), AuNS (green), and AuNR (red). Short-Linker AgNS-PpIX show a statistically significant decrease in cell viability at only 0.2 μM PpIX. Short-Linker AuNS-PpIX show a statistically significant decrease in cell viability at 2 μM PpIX. AuNR-PpIX show no statistically significant change in cell viability when compared to PpIX alone at these concentrations. Error bars indicate $\pm$ one standard deviation of three independent experiments with p-value < 0.05.

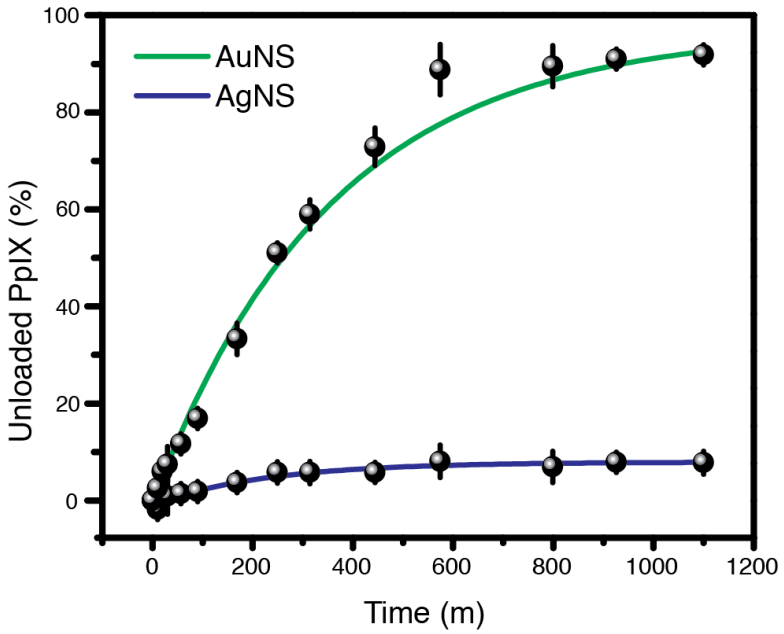

Figure 68: Diffusion of PpIX drug from AgNS-PpIX (blue) and AuNS-PpIX (green) Electrostatic complexes from water into toluene over time. AuNS-PpIX Electrostatic complexes unload ca. 95% of the drug after 24 hours, whereas AgNS-PpIX complexes unload only ca. 10% of the PpIX coordinated to the AgNS surface. This illustrates the relative strength of the silver-carboxyl interaction relative to the gold-carboxl interaction and explains why AgNS-PpIX Electrostatic complexes show similar activity to AgNS-PpIX Short-Linker complexes; with the majority of the drug left on the AgNS surface, plasmonic enhancement of drug activity still occurs.

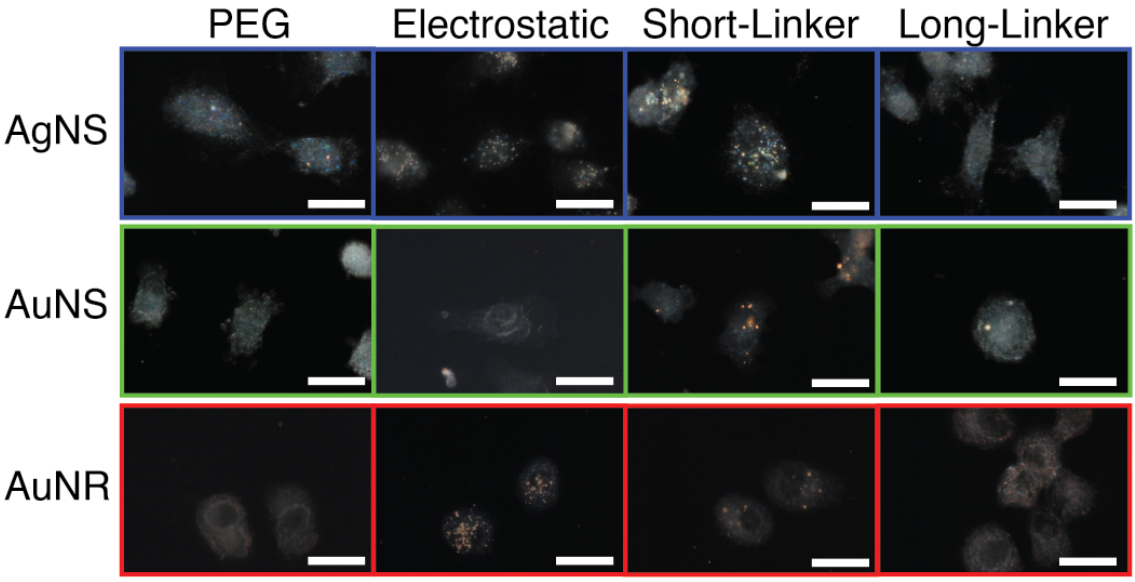

Figure 69: Dark field microscopy images of HSC-3 cells after 24 hours of incubation with NP-PpIX complexes. All NP-PpIX conjugates and PEG-NPs showed minimal uptake, which is indicated by the lack of localized light scattering within the cells. Scale bars represent 10 microns.

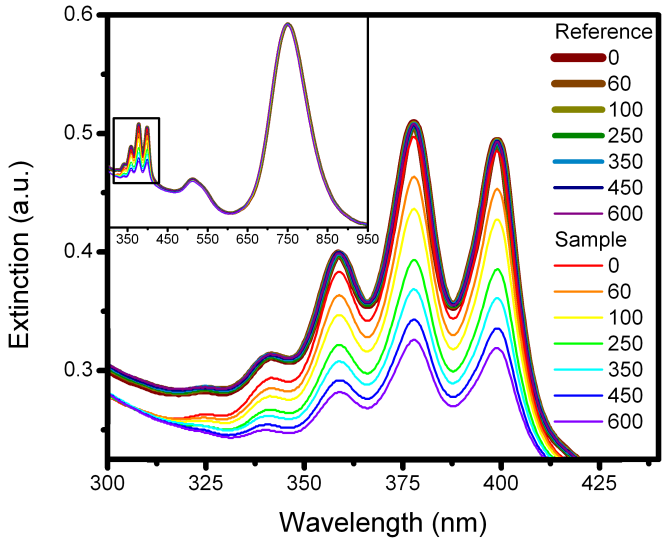

Figure 70: Extinction spectrum of an example SOG experiment with AuNR-PpIX and the ABDA scavenger. Inset shows full spectrum, while the main graph shows the ABDA peaks in the irradiated sample shrinking relative to the reference cuvette in the dark.

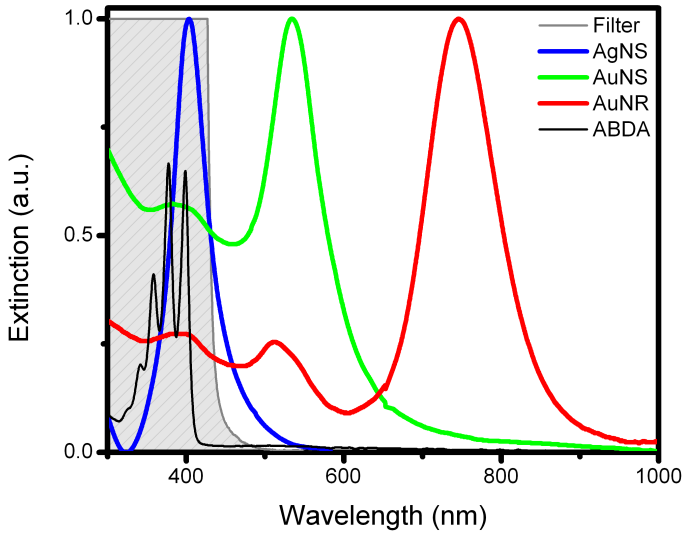

Figure 71: Extinction spectrum of AgNS-PpIX, AuNS-PpIX, AuNR-PpIX, ABDA SOG detector molecule, and the filter used for SOG experiments. Illustrates that the plasmon of the silver complexes is not excited, as the long-pass filter is necessary to keep ABDA from photobleaching.

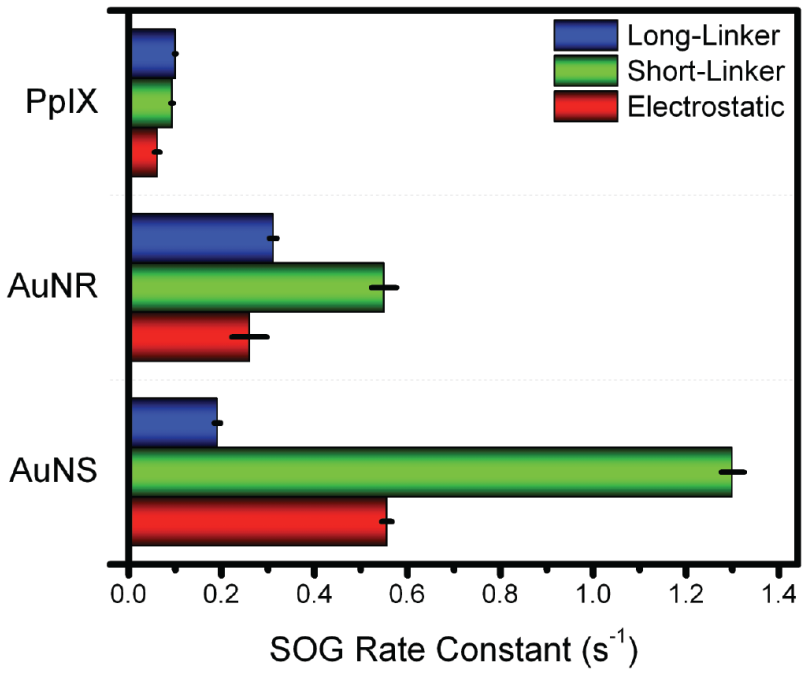

Figure 72: Singlet oxygen generation rate constants for PpIX, AuNS-PpIX, and AuNR-PpIX under Electrostatic (red), Short-Linker (green), and Long-Linker (red) conjugation. AgNS-PpIX showed comparable activity to free PpIX due to the filter used in this experiment, which keeps the detector molecule from photobleaching but also prevents excitation of the AgNS plasmon. This illustrates the role of plasmon resonance in enhancment. Greated enhancement of SOG is seen in AuNS-PpIX complexes versus AuNR-PpIX complexes for Short-Linker and Electrostatic conjugations. Within each NP group, the greatest enhancement is seen for the Short-Linker complexes, where the PpIX is bound close to the NP surface. Electrostatic complexes show decreased SOG as a result of PpIX unloading from the NP surface during te experiment. Long-Linker AuNS complexes show the least activity due to the distance between the particle surface and the PpIX molecule. AuNR-PpIX complexes show decreased SOG relative to AuNS-PpIX complexes due to quenching of PpIX emission by the longitudinal plasmon resonance and the very limited enhancement of PpIX absorption via the transverse plasmon resonance. AuNR-PpIX Long-Linker complexes show greater activity versus AuNS-PpIX Long-Linker due to preferential attachment of the thiol linker to the ends of the rods and the resultant ability of the PpIX to lie along the sides of the rod, where favorable plasmon resonance occurs. Error bars indicate one standard deviation of three or more independent experiments.

5.11 REFERENCES

[1] Adams, G. E. and Willson, R. L., "Pulse radiolysis studies on oxidation of organic radicals in aqueous solution," *Transactions of the Faraday Society*, vol. 65, no. 563P, pp. 2981–and, 1969. ISI Document Delivery No.: E9224 Times Cited: 264 Cited Reference Count: 18 Adams, ge willson, rl Royal soc chemistry Cambridge.

[2] Alexander, C. K., "Photodynamic therapy," *Medical Laser Application*, vol. 20, no. ed070ffe-e347-95f7-9375-c733a41ef1c3, 2005. 10.1016/j.mla.2005.02.001.

[3] Austin, L., Kang, B., Yen, C.-W., and El-Sayed, M., "Nuclear targeted silver nanospheres perturb the cancer cell cycle differently than those of nanogold," *Bioconjugate Chemistry*, vol. 22, no. c0db4233-d260-284c-32d0-2dd05e13e02e, pp. 2324–2355, 2011. 10.1021/bc200386m.

[4] Bechet, D., Couleaud, P., Frochot, C., Viriot, M.-L., Guillemin, F., and Barberi-Heyob, M., "Nanoparticles as vehicles for delivery of photodynamic therapy agents," *Trends in biotechnology*, vol. 26, no. a7a20a11-1f02-69d0-585f-c78734c0e274, pp. 612–633, 2008. 10.1016/j.tibtech.2008.07.007.

[5] Burda, C., Chen, X. B., Narayanan, R., and El-Sayed, M. A., "Chemistry and properties of nanocrystals of different shapes," *Chemical Reviews*, vol. 105, no. 4, pp. 1025–1102, 2005. Burda, C Chen, XB Narayanan, R El-Sayed, MA.

[6] Burger, C. B., Goerres, G. G., Schoenes, S. S., Buck, A. B., Lonn, A. L., and von Schulthess, G. v. S., "Pet attenuation coefficients from ct

images: experimental evaluation of the transformation of ct into pet 511-kev attenuation coefficients," *European Journal of Nuclear Medicine and Molecular Imaging*, vol. 29, no. 7, pp. 922–927, 2002.

[7] Castano, A. P., Demidova, T. N., and Hamblin, M. R., "Mechanisms in photodynamic therapy: part one—photosensitizers, photochemistry and cellular localization," *Photodiagnosis and Photodynamic Therapy*, vol. 1, no. 4, pp. 279–293, 2004.

[8] Chatterjee, D., Fong, L., and Zhang, Y., "Nanoparticles in photodynamic therapy: an emerging paradigm," *Advanced drug delivery reviews*, vol. 60, no. 1b229b4e-b52c-9fc9-6fd3-c78734f68546, pp. 1627–1664, 2008. 10.1016/j.addr.2008.08.003.

[9] Chen, Y., Munechika, K., and Ginger, D., "Dependence of fluorescence intensity on the spectral overlap between fluorophores and plasmon resonant single silver nanoparticles," *Nano Letters*, vol. 7, no. 1a42b626-2332-32c5-c072-ebbec0e5f80b, pp. 690–696, 2007. 10.1021/nl062795z.

[10] Cheng, Y., C, A., and Meyers, J., "Highly efficient drug delivery with gold nanoparticle vectors for in vivo photodynamic therapy of cancer," *Journal of the ...*, no. 87396d63-c4d5-9682-e7cf-8c11e083226f, 2008.

[11] Daniel, M.-C. and Astruc, D., "Gold nanoparticles: assembly, supramolecular chemistry, quantum-size-related properties, and applications toward biology, catalysis, and nanotechnology," *Chemical Reviews*, vol. 104, no. a213219e-00c4-fad2-5f23-8c11dc845d91, pp. 293–639, 2004. 10.1021/cr030698+.

[12] DeRosa, M. C. and Crutchley, R. J., "Photosensitized singlet oxygen and its applications," *Coordination Chemistry Reviews*, vol. 233–234, no. 0, pp. 351–371, 2002.

[13] Derycke, A., "Liposomes for photodynamic therapy," *Advanced drug delivery reviews*, vol. 56, no. 7a6f9219-49ea-1b87-dc04-e147cb08887e, 2004. 10.1016/j.addr.2003.07.014.

[14] Dolmans, D., Fukumura, D., and Jain, R. K., "Photodynamic therapy for cancer," *Nature Reviews Cancer*, vol. 3, no. 5, pp. 380–387, 2003. Dolmans, DEJGJ Fukumura, D Jain, RK.

[15] Dougherty, T., Kaufman, J., Goldfarb, A., Weishaupt, K., Boyle, D., and Mittleman, A., "Photoradiation therapy for the treatment of malignant tumors," *Cancer Research*, vol. 38, no. 5a50b002-2e56-b25f-441c-e147cb08aa80, pp. 2628–2663, 1978.

[16] Duncan, C. H., Peter, I. W., Richard, E.-G., Simon, F., Andrew, B., Isabelle, C., Michael, J. C., and David, A. R., "Generation of cytotoxic singlet oxygen via phthalocyanine-stabilized gold nanoparticles: A potential delivery vehicle for photodynamic therapy," *Langmuir*, vol. 18, no. 51335216-c4ba-d527-1532-8c11d7cf3dfb, 2002. 10.1021/la0256230.

[17] Fu, Y., Zhang, J., and Lakowicz, J., "Plasmonic enhancement of single-molecule fluorescence near a silver nanoparticle," *Journal of Fluorescence*, vol. 17, no. 7da275a2-ae7b-b621-f6b1-ebbec0e6cf3a, pp. 811–817, 2007. 10.1007/s10895-007-0259-0.

[18] Grodzicki, A., Łakomska, I., Piszczek, P., Szymańska, I., and Szłyk, E., "Copper (i), silver (i) and gold (i) carboxylate complexes as precursors in chemical vapour deposition of thin metallic films," *Coordination chemistry reviews*, vol. 249, no. 21, pp. 2232–2258, 2005.

[19] Henderson, B. W. and Dougherty, T. J., "How does photodynamic therapy work?," *Photochemistry and Photobiology*, vol. 55, no. 1, pp. 145–157, 1992.

[20] Hopper, C., "Photodynamic therapy: a clinical reality in the treatment of cancer," *The lancet oncology*, vol. 1, no. 4, pp. 212–219, 2000.

[21] Huang, X. H., Jain, P. K., El-Sayed, I. H., and El-Sayed, M. A., "Gold nanoparticles: interesting optical properties and recent applications in cancer diagnostic and therapy," *Nanomedicine*, vol. 2, no. 5, pp. 681–693, 2007. Huang, Xiaohua Jain, Prashant K. El-Sayed, Ivan H. El-Sayed, Mostafa A.

[22] Huang, X. H., Jain, P. K., El-Sayed, I. H., and El-Sayed, M. A., "Plasmonic photothermal therapy (pptt) using gold nanoparticles," *Lasers in Medical Science*, vol. 23, no. 3, pp. 217–228, 2008. Huang, Xiaohua Jain, Prashant K. El-Sayed, Ivan H. El-Sayed, Mostafa A.

[23] Igarashi, A., Konno, H., Tanaka, T., Nakamura, S., Sadzuka, Y., Hirano, T., and Fujise, Y., "Liposomal photofrin enhances therapeutic efficacy of photodynamic therapy against the human gastric cancer," *Toxicology letters*, vol. 145, no. 2, pp. 133–141, 2003.

[24] Jain, P. K., Eustis, S., and El-Sayed, M. A., "Plasmon coupling in nanorod assemblies: Optical absorption, discrete dipole approximation simulation, and exciton-coupling model," *Journal of Physical Chemistry B*, vol. 110, no. 37, pp. 18243–18253, 2006. Jain, Prashant K. Eustis, Susie El-Sayed, Mostafa A.

[25] Jain, P. K., Huang, X. H., El-Sayed, I. H., and El-Sayed, M. A., "Noble metals on the nanoscale: Optical and photothermal properties and some applications in imaging, sensing, biology, and medicine," *Accounts of Chemical Research*, vol. 41, no. 12, pp. 1578–1586, 2008. Jain, Prashant K. Huang, Xiaohua El-Sayed, Ivan H. El-Sayed, Mostafa A.

[26] Jain, P. K. and El-Sayed, M. A., "Surface plasmon coupling and its universal size scaling in metal nanostructures of complex geometry: Elongated particle

pairs and nanosphere trimers," *The Journal of Physical Chemistry C*, vol. 112, no. 13, pp. 4954–4960, 2008. doi: 10.1021/jp7120356.

[27] Jang, B., Park, J.-Y., Tung, C.-H., Kim, I.-H., and Choi, Y., "Gold nanorod-photosensitizer complex for near-infrared fluorescence imaging and photodynamic/photothermal therapy in vivo," *Acs Nano*, vol. 5, no. 022f35e5-834f-f059-58f0-8c11daa10f53, pp. 1086–1180, 2011. 10.1021/nn102722z.

[28] Jeffes, E., McCullough, J., Weinstein, G., Kaplan, R., Glazer, S., and Taylor, J., "Photodynamic therapy of actinic keratoses with topical aminolevulinic acid hydrochloride and fluorescent blue light," *Journal of the American Academy of Dermatology*, vol. 45, no. af66ced4-b367-b90e-3e66-e147cb08bf6d, pp. 96–200, 2001. 10.1067/mjd.2001.114288.

[29] Kalka, K., Merk, H., and Mukhtar, H., "Photodynamic therapy in dermatology," *Journal of the American Academy of Dermatology*, vol. 42, no. eb369ca5-e756-5a68-c0a1-c787352a0b7d, p. 389, 2000.

[30] Kanae, I., Tomoya, H., Noriyuki, M., Sei, Y., Yoshito, T., Tomohiro, A., Yukihiro, N., and Naoto, O., "Antiangiogenic photodynamic therapy (pdt) by using long-circulating liposomes modified with peptide specific to angiogenic vessels," *Biochimica et Biophysica Acta (BBA) - Biomembranes*, vol. 1669, 2005.

[31] Kennedy, J., Pottier, R., and Pross, D., "Photodynamic therapy with endogenous protoporphyrin ix: basic principles and present clinical experience," *Journal of photochemistry and photobiology. B, Biology*, vol. 6, no. 0d0f52b5-bab7-ab78-7179-284786bfaab0, pp. 143–151, 1990.

[32] Khaing Oo, M., Yang, Y., Hu, Y., Gomez, M., Du, H., and Wang, H., "Gold nanoparticle-enhanced and size-dependent generation of reactive oxygen species from protoporphyrin ix," *ACS nano*, vol. 6, no. 3, pp. 1939–1947, 2012.

[33] Kuvzelova, K., Grebevnova, D., Pluskalova, M., Marinov, I., and Hrkal, Z., "Early apoptotic features of k562 cell death induced by 5-aminolaevulinic acid-based photodynamic therapy," *Journal of Photochemistry and Photobiology B: Biology*, vol. 73, no. 1, pp. 67–78, 2004.

[34] Lee, K. S. and El-Sayed, M. A., "Dependence of the enhanced optical scattering efficiency relative to that of absorption for gold metal nanorods on aspect ratio, size, end-cap shape, and medium refractive index," *Journal of Physical Chemistry B*, vol. 109, no. 43, pp. 20331–20338, 2005. Lee, KS El-Sayed, MA.

[35] Lee, K. and El-Sayed, M., "Gold and silver nanoparticles in sensing and imaging: sensitivity of plasmon response to size, shape, and metal composition," *The Journal of Physical Chemistry B*, vol. 110, no. 39, pp. 19220–19225, 2006.

[36] Link, S. and El-Sayed, M. A., "Shape and size dependence of radiative, non-radiative and photothermal properties of gold nanocrystals," *International Reviews in Physical Chemistry*, vol. 19, no. 3, pp. 409–453, 2000. Link, S El-Sayed, MA.

[37] Lubart, R., Lavie, R., and Friedman, H., "The penetration of white light through human tissue," *Photomedicine and Laser Surgery*, vol. 23, no. 4, pp. 435–436, 2005. ISI Document Delivery No.: 967CN Times Cited: 0 Cited Reference Count: 7 Lubart, R Lavie, R Friedman, H Mary ann liebert inc New rochelle.

[38] Ondrej, S., Robert, N., Colette, M., and Brian, D. M., "Optimization of nanoparticle size for plasmonic enhancement of fluorescence," *Plasmonics*, vol. 2, no. 13ba6251-9fa7-6d2a-c480-ebbec0e52866, 2006. 10.1007/s11468-006-9020-9.

[39] Peer, D., Karp, J., Hong, S., Farokhzad, O., Margalit, R., and Langer, R., "Nanocarriers as an emerging platform for cancer therapy," *Nature Nanotechnology*, vol. 2, no. 3eab5637-8ba6-b50f-7220-e16f5c8f95e4, pp. 751–811, 2007. 10.1038/nnano.2007.387.

[40] Phillips, R. L., Miranda, O. R., You, C. C., Rotello, V. M., and Bunz, U. H. F., "Rapid and efficient identification of bacteria using gold-nanoparticle - poly(para-phenyleneethynylene) constructs," *Angewandte Chemie-International Edition*, vol. 47, no. 14, pp. 2590–2594, 2008. Phillips, Ronnie L. Miranda, Oscar R. You, Chang-Cheng Rotello, Vincent M. Bunz, Uwe H. F.

[41] Rawls, H. R. and Vansante.Pj, "Singlet oxygen and initiation of fatty acid autoxidation," *Tetrahedron Letters*, no. 14, pp. 1675–and, 1968. Rawls, hr vansante.pj.

[42] Reddi, E., "Role of delivery vehicles for photosensitizers in the photodynamic therapy of tumours," *Journal of photochemistry and photobiology. B, Biology*, vol. 37, no. 98261572-c1f6-886c-7a6a-e16643b2d7bc, pp. 189–284, 1997.

[43] Sapsford, K. E., Berti, L., and Medintz, I. L., "Materials for fluorescence resonance energy transfer analysis: Beyond traditional donor–acceptor combinations," *Angewandte Chemie International Edition*, vol. 45, no. f6466c20-0626-f03f-4b70-8c11dd006829, 2006. 10.1002/anie.200503873.

[44] Schweitzer, C. and Schmidt, R., "Physical mechanisms of generation and deactivation of singlet oxygen," *Chemical Reviews*, vol. 103, no. d71145f7-0605-21d7-fb15-c7ad90436a01, pp. 1685–2442, 2003. 10.1021/cr010371d.

[45] Silva, E. F., Serpa, C., Dabrowski, J., Monteiro, C., Formosinho, S., Stochel, G., Urbanska, K., Simões, S., Pereira, M., and Arnaut, L., "Mechanisms of singlet-oxygen and superoxide-ion generation by porphyrins

and bacteriochlorins and their implications in photodynamic therapy," *Chemistry (Weinheim an der Bergstrasse, Germany)*, vol. 16, no. b07267e5-a03f-a457-6cd6-c71e7e40ffae, pp. 9273–9359, 2010. 10.1002/chem.201000111.

[46] Tebello, N., "Desired properties of new phthalocyanines for photodynamic therapy," *Pure and Applied Chemistry*, vol. 83, no. 57c712ad-3a64-f04c-d1a1-8c11e14c0bfa, 2011. 10.1351/PAC-CON-10-11-22.

[47] Tuchscherer, A., Schaarschmidt, D., Schulze, S., Hietschold, M., and Lang, H., "Gold nanoparticles generated by thermolysis of ìall-in-oneî gold (i) carboxylate complexes," *Dalton Transactions*, vol. 41, no. 9, pp. 2738–2746, 2012.

[48] van Vlerken, L. and Amiji, M., "Multi-functional polymeric nanoparticles for tumour-targeted drug delivery," *Expert opinion on drug delivery*, vol. 3, no. 4d824540-cf51-e6f9-8921-e16f5c8fe1e0, pp. 205–221, 2006. 10.1517/17425247.3.2.205.

[49] Yen, C., Hayden, S., Dreaden, E., Szymanski, P., and El-Sayed, M., "Tailoring plasmonic and electrostatic field effects to maximize solar energy conversion by bacteriorhodopsin, the other natural photosynthetic system," *Nano letters*, vol. 11, no. 9, pp. 3821–3826, 2011.

CHAPTER VI

SYNTHESIS AND CHARACTERIZATION OF SELECTED NANOMATERIALS

6.1 Chapter Summary

The synthesis of nanomaterials has been the focus of intense research over the past few decades. This first began as scientists developed methods to synthesize and characterize homogenous solutions and arrays of nanoparticles of a variety of sizes, [18, 16, 21] shapes (spheres, [38, 5] rods, [12, 19, 30, 17] hollow spheres, [32, 3, 36] cubes, [36, 35, 33] cages, [37, 23] etc.), and compositions (gold, [14, 40, 42] silver, [41, 22] copper, [8, 11] platinum, [2, 1, 26, 31] paladium, [34] semiconductor, [10, 25] etc.). What followed was some very intense work surrounding the elucidation of the properties of nanoscale materials, which was itself followed by an explosion of work revolving around applications of nanotechnology. Still, though this work began in ernest more than three decades ago, new synthetic techniques are still being developed, and new properties of nanomaterials are still being discovered.

Nanoparticles are traditionally prepared by either top-down or bottom-up procedures. [13, 6, 7] Top-down methods normally involve the use of lithography, where one starts with a bulk material and removes the bulk that is not desired, leaving the nanoparticle. Bottom-up methods build nanoparticles atom-by-atom, normally from a metal or semiconductor salt. The salt is reduced with a reducing agent, generating ground-state atoms that nucleate and begin to form a particle. This is performed in the presence of a surface ligand - called the capping agent - which passivates the surface of the particle. As this is all in dynamic equilibrium, the capping agent to salt ratio generally determines the size of the resulting particle. Conventionally, as

in this thesis, specific nanoparticles can be abbreviated as metal, shape, and capping agent (e.g. silver nanospheres capped with citrate, AgNS@Citrate).

In some cases, such as the gold nanosphere citrate reduction, [9] the capping and reducing agent are the same; the citrate both reduces the gold salt and passivates the resulting nanoparticle surface by electrostatically isolating the NPs from one another in solution. Other variations of this method employ the use of a metallic seed particle (< 2 nm) to reduce a metal salt in solution without the need for a separate reducing agent. [36, 29, 24, 27] These seeding growth syntheses can direct the crystallinity of the resulting nanoparticle. [36, 23] Anisotropic particles, such as rods, are generally synthesized using a capping agent that binds preferentially to one crystal surface over another, thereby restricting growth in that dimension. [29, 28]

This thesis work focuses almost entirely on the latter method of preparation; thus, the syntheses presented herein are colloidal, bottom-up synthetic techniques. The synthesis and characterization of a variety of plasmonic metal nanoparticles, semiconductor quantum dot nanoparticles, and titanium dioxide nanostructures, are presented, many of which have had their applications discussed in the previous chapters. Several other nanoparticle syntheses are also included - despite their absence from the preceeding chapters - in hopes that their syntheses will find use in the experiments of future nanoscientists. Also included are some relationships governing extinction coefficients and capping agent-to-metal salt ratio that may be useful for the colloidal preparation of some nanoparticles.

6.2 Colloidal Syntheses of Selected Gold and Silver Nanoparticles

6.2.1 Silver Nanospheres (AgNS)

6.2.1.1 AgNS@Citrate

Silver nanospheres of approximately 10 nm diameter were prepared by first injecting silver nitrate (1.5 mL, 1 wt.%) and sodium citrate (1.2 mL, 38.8 mM) into boiling

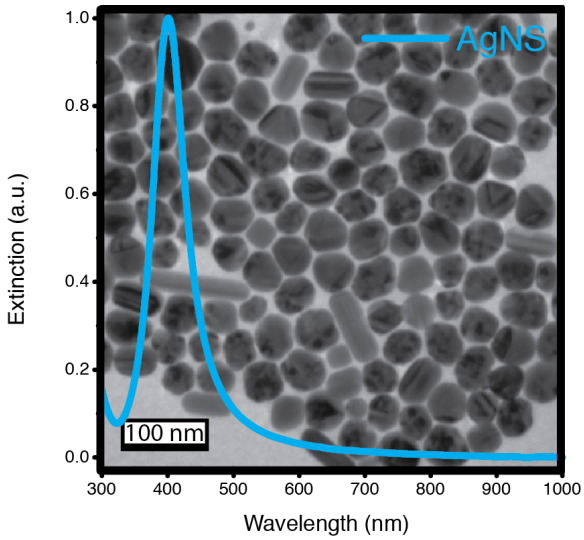

Figure 73: Transmission electron micrograph of silver nanospheres (40 nm) capped with citrate.

deionized water (150 mL). Sodium borohydride (1.8 mL, 0.01 M, cold) was then injected quickly, the heat was removed, and stirring was continued until the solution reached room temperature. Particles were then stored in the dark.

Silver nanospheres of approximately 40 nm diameter were prepared by adding $AgNO_3$ (25 mL, 1 wt.%) to boiling water (deionized, 175 mL) in a covered (watch glass), trace-clean, 250 mL Erlenmeyer flask at a stir speed of 500 rpm. At reboil, the watch glass cover was removed, and citrate solution (8 mL, 38.8 mM) was added to the flask. The stir speed was increased to 1000 rpm, and sodium borohydride (2.4 mL, 0.1 M) was injected quickly and all at once. The stir speed was then reduced to 500 rpm as the solution turned black. The heat was turned off, and the solution was allowed to stir for 5 mins. The resulting creamy, light-green solution was covered and placed in the dark overnight to allow the particles to ripen (Figure 73).

6.2.1.2 AgNS@PVP

Ethylene glycol (EG, 25 mL) was heated to 150 ^{o}C and maintained at this temperature for 1 h. Polyvinyl pyrrolidone (PVP, 0.28 g) was dissolved in EG (10 mL) and added to the flask under stirring at 900 rpm. When the temperature restabilized at 150 ^{o}C,

$AgNO_3$ (0.12 g) in EG (2.5 mL) was added, immediately followed by $Na_2S \bullet 4H_2O$ in EG (0.4 mL, 3 mM). The silver was reduced after 15 mins, at which point the flask was removed from heat and allowed to cool slowly. Particles were diluted 1:1 with water and centrifuged. They were then redispersed in water and centrifuged a second time.

6.2.1.3 Hollow AgNS@Glutathione

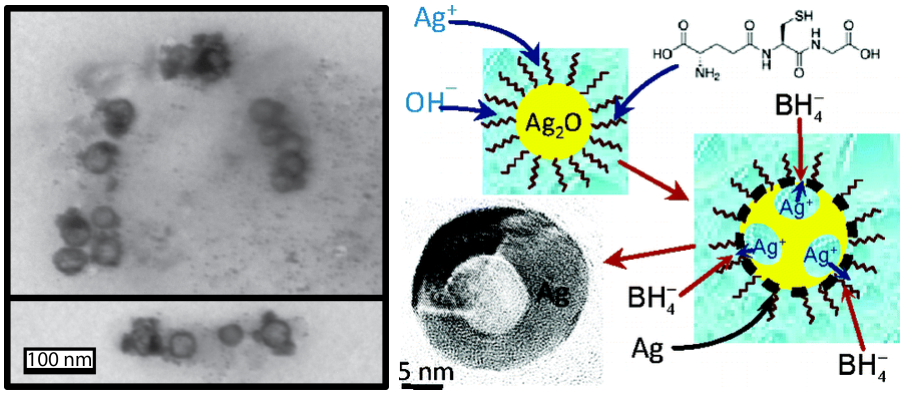

Figure 74: Transmission electron micrograph of hollow silver nanospheres (ca. 30 nm) capped with glutathione (left) and schematic representation of the mechanism of formation of hollow silver nanospheres as illustrated in Ben et. al (right). [4]

Silver nitrate (1.5 mL, 10 mM) and glutathione (180 μL, 10 mM) were added to water (25 mL) in an ice bath. Sodium hydroxide (5.0 mL, 0.1 M) was added under vigorous stirring to bring the pH to 12. The resulting solution of silver oxide template nanospheres was pale yellow in color. Sodium borohydride (1.8 mL, 10 mM) was injected all at once, and the solution turned red. The mechanism for the formation of these particles is rendered in Figure 74 with their TEM image. [4]

6.2.2 Silver Nanocubes and Nanocuboids (AgNC, AgNCuboid)

6.2.2.1 AgNC@PVP

Ethylene glycol (EG, 25 mL) was heated to 150 °C and maintained at this temperature for 1 h. Polyvinyl pyrrolidone (PVP, 0.28 g) was dissolved in EG (10 mL) and added to the flask with gentle stirring. When the temperature restabilized to 150 ^{o}C, $AgNO_3$

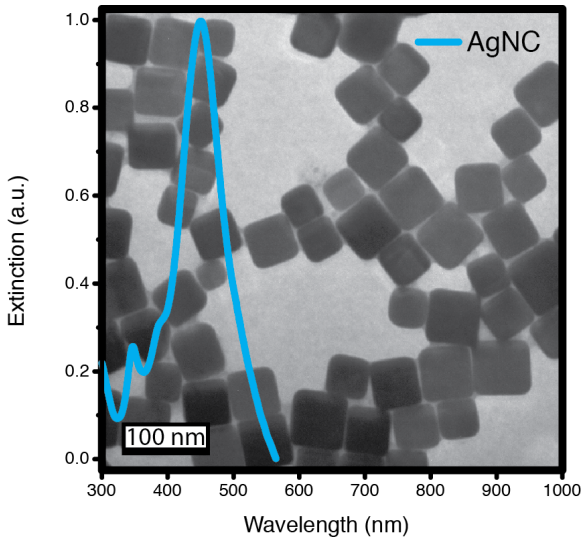

Figure 75: Transmission electron micrograph of silver nanocubes (ca. 40 nm) capped with PVP.

(0.12 g) in EG (2.5 mL) was added, immediately followed by $Na_2S \bullet 4H_2O$ (3 mM) in EG (0.4 mL). The silver was reduced after 15 mins, at which point the flask was removed from heat and allowed to cool slowly. Particles were diluted 1:1 with water and centrifuged. They were then redispersed in water and centrifuged a second time, producing the silver cubes seen in Figure 75).

6.2.2.2 AgNCuboid@PVP

Ethylene glycol (EG, 25 mL) was heated to 150 ^{o}C and maintained at this temperature for 1 h. Polyvinyl pyrrolidone (PVP, 0.28 g) was dissolved in EG (10 mL) and added to the flask under stirring at 400-600 rpm. Stir speed here controls the degree of truncation of cube corners. When the temperature restabilized to 150 ^{o}C, $AgNO_3$ (0.12 g) in EG (2.5 mL) was added, immediately followed by $Na_2S \bullet 4H_2O$ (3 mM) in EG (0.4 mL). The silver was reduced after 15 mins, at which point the flask was removed from heat and allowed to cool slowly. Particles were diluted 1:1 with water and centrifuged. They were then redispersed in water and centrifuged a second time.

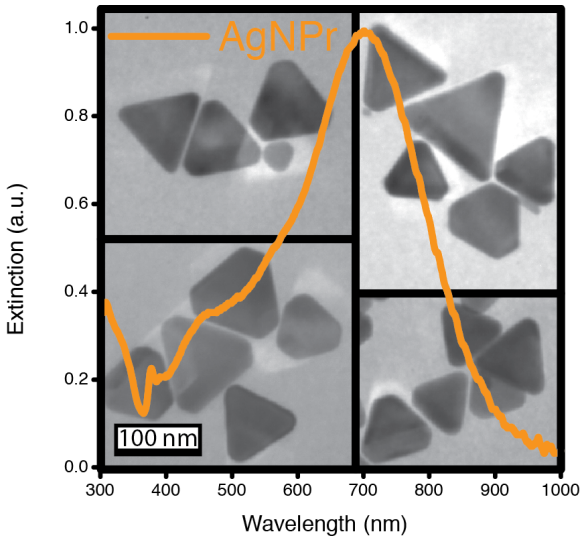

Figure 76: Transmission electron micrograph of silver nanoprisms (ca. 60 nm edge length) capped with PVP.

6.2.3 Silver Nanoprisms (AgNPr)

6.2.3.1 AgNPr@PVP

Silver nitrate (14 mL, 0.59 mM), sodium citrate (35 mL, 43.9 mM), and polyvinylpyrrolidone (10.5 mL, 0.36 mM, MW 55K) were added in succession to boiling deionized water (70 mL) in a 500 mL round bottom flask. Sodium borohydride (5.6 mL, 99.1 mM) was injected, and the solution turned yellow. The solution was heated for 5 additional minutes, and the flask was removed from heat and irradiated for 5 hours with a 250 W tungsten lamp. Particles were cleaned twice via centrifugation yielding the ca. 60 nm edge length silver nanoprisms pictured in Figure 76.

6.2.4 Gold Nanospheres (AuNS)

6.2.4.1 AuNS@Citrate

Gold nanospheres (ca. 10 nm diameter) were prepared by first heating hydrogen tetrachloroaurate trihydrate (50 mL, 1.0 mM) to boiling in a 250 mL Erlenmeyer flask with a watch glass cover under vigorous stirring. Sodium citrate solution (5 mL, 38.8 mM) was injected rapidly, and the solution color changed from yellow to colorless

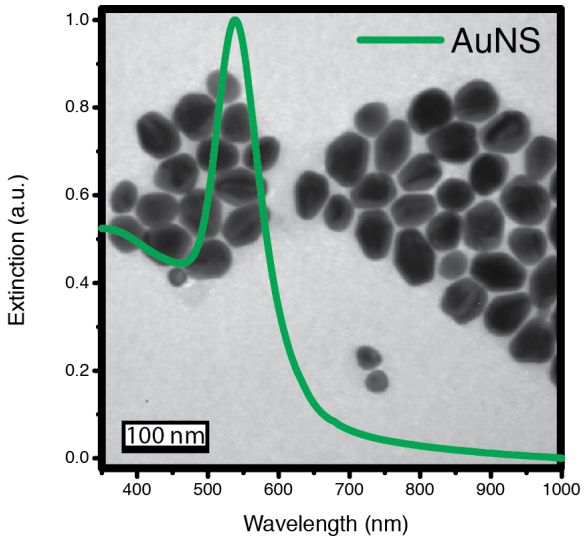

Figure 77: Transmission electron micrograph of gold nanospheres (ca. 40 nm diameter) capped with CTAB.

to black to brilliant red within 1 minute. Stirring and heating were continued for 15 minutes, and the solution was cooled to room temperature.

Gold nanospheres of ca. 40 nm diameter were prepared following the above procedure but injecting less citrate solution (350 μL, 0.01 mM).

The relationship between citrate concentration and gold concentration is presented in Figure 78, and these data were fitted with an exponential decay,

$$y = y_0 + Ae^{-x/t} \tag{9}$$

in order to generate the equations presented therein.

These fits were used to generate Tables 5 and 6, which present some example AuNS@citrate sizes, plasmon peak positions, and the ratios of gold to citrate required to produce these characteristics experimentally. These values are derived from the following equations (10, 11) governing the relationship that plasmon peak position and nanosphere diameter have to the gold to citrate ratio used in their synthesis:

$$\frac{citrate}{gold} = -0.0305 * ln\frac{Desired\ Plasmon\ Peak\ Position\ (nm) - 515.9}{42.7} \tag{10}$$

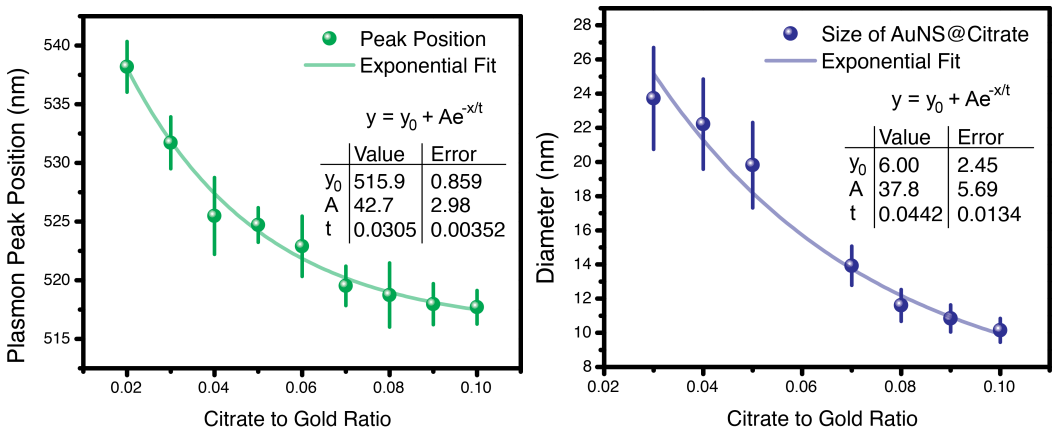

Figure 78: Plasmon peak position (left, green) and gold nanosphere diameter (right, blue) as a function of citrate to gold ratio used in the reduction/passification of AuNS@Citrate.

$$\frac{citrate}{gold} = -0.0442 * ln\frac{Desired\ Diameter\ (nm) - 6.00}{37.8} \tag{11}$$

Table 5: Some example gold to citrate ratios and the size of the corresponding AuNS@Citrate produced.

Size (nm)	Gold/Citrate Ratio	Error on Ratio
10	0.0992	0.0498
15	0.0634	0.0388
20	0.0439	0.0280
25	0.0304	0.0217
30	0.0201	0.0173
35	0.0117	0.0140
40	0.0047	0.0113

Table 6: Some example gold to citrate ratios and the plasmon peak position of the corresponding AuNS@Citrate produced.

Plasmon Peak Position (nm)	Gold/Citrate Ratio	Error on Ratio
516	0.1800	0.0799
520	0.0714	0.0169
525	0.0471	0.0105
530	0.0338	0.0079
535	0.0245	0.0063
540	0.0174	0.0052
545	0.0117	0.0044
550	0.0068	0.0037
555	0.0027	0.0031

6.2.4.2 AuNS@CTAB

Gold nanospheres (ca. 40 nm diameter) were synthesized using a modified seed-mediated gold nanorod synthesis. [15]

The seed solution was first prepared by dissolving CTAB (0.273 g) in water (deionized, 7.5 mL) with mild stirring and slight heating. Hydrogen tetrachloroaurate trihydrate (250 μL, 10 mM) was added, and then the gold was reduced with sodium borohydride (600 μL, 0.1 M). The seed solution was stirred for 5 mins before use.

The growth solution was prepared by dissolving CTAB (15.49 g) in water (deionized 425 mL) with mild stirring and slight heating. Tetrachloroaurate trihydrate (20 mL, 10 mM) was then added, yielding a clear, bronze-colored solution. The gold was then reduced with ascorbic acid (11.6 mL, 79 mM), yielding a clear, colorless solution.

Seed solution (350 μL) was then injected to the growth solution, which was allowed to stir (400 rpm) for 3 hours. The amount of seed solution added determines the size of the resulting nanospheres. The nanoparticles were cleaned via 2x successive centrifugation, yielding the gold nanospheres depicted in Figure 77.

6.2.4.3 AuNS@DDT

Gold nanospheres (ca. 2 nm diameter), were synthesized by combining hydrogen tetrachloroaurate trihydrate (aq, 30 mL, 30 mM) with tetraoctylammonium bromide transfer reagent (toluene, 80 mL, 50 mM). The two-phase system was stirred vigorously until all of the gold chloride was transferred to the organic layer. Dodecanethiol (170 mg) was added, followed by the slow addition of aqueous sodium borohydride (25 mL, 0.4 M). Stirring was continued for 3 hours, and the aqueous phase was removed and discarded. The organic phase was concentrated to approximately 10 mL using a rotary evaporator, and ethanol was added (400 mL). The solution was kept at -18 °C for 4 hours. The precipitate was filtered, washed with ethanol, redissolved in toluene (10 mL), and reprecipitated with ethanol (400 mL). The resulting dark brown precipitate was filtered again, washed with ethanol, and characterized by UV-Vis and TEM.

6.2.5 Gold Nanorods (AuNR)

6.2.5.1 AuNR@CTAB

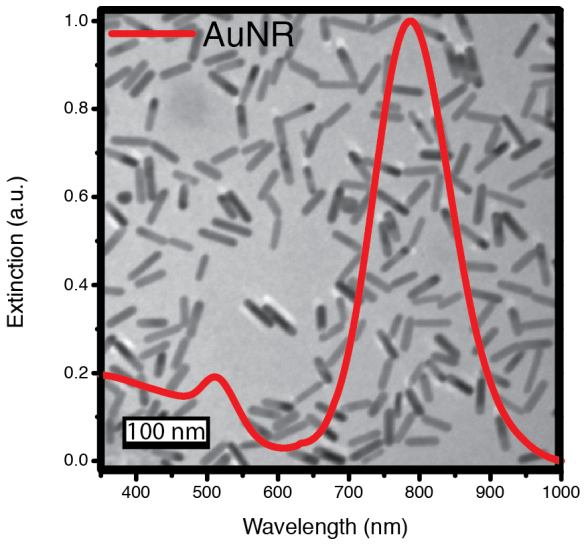

Figure 79: Transmission electron micrograph of gold nanorods (ca. 10 x 40 nm) capped with CTAB.

Gold nanorods (10 nm diameter, 40 nm length) were synthesized using a seed-mediated approach. [15]

The seed solution was first prepared by dissolving cetyl-trimethylammonium bromide (CTAB, 0.273 g) in water (deionized, 7.5 mL) with mild stirring and slight heating. Hydrogen tetrachloroaurate trihydrate (250 μL, 10 mM) was added, and the gold was reduced with sodium borohydride (600 μL, 0.1 M). The solution was stirred for 5 mins before use.

The growth solution was prepared by dissolving CTAB (15.49g) in water (deionized 425 mL) with mild stirring and slight heating. Tetrachloroaurate trihydrate (20 mL, 10 mM) was then added, yielding a clear, bronze-colored solution. Silver nitrate (8.5 mL, 4 mM) was added, and then the gold was reduced with ascorbic acid (11.6 mL, 79 mM), yielding a clear, colorless solution. Seed solution (960 μ L) was injected, and the solution was left undisturbed overnight. The nanoparticles were cleaned via 2x successive centrifugation, yielding the gold nanorods depicted in Figure 79.

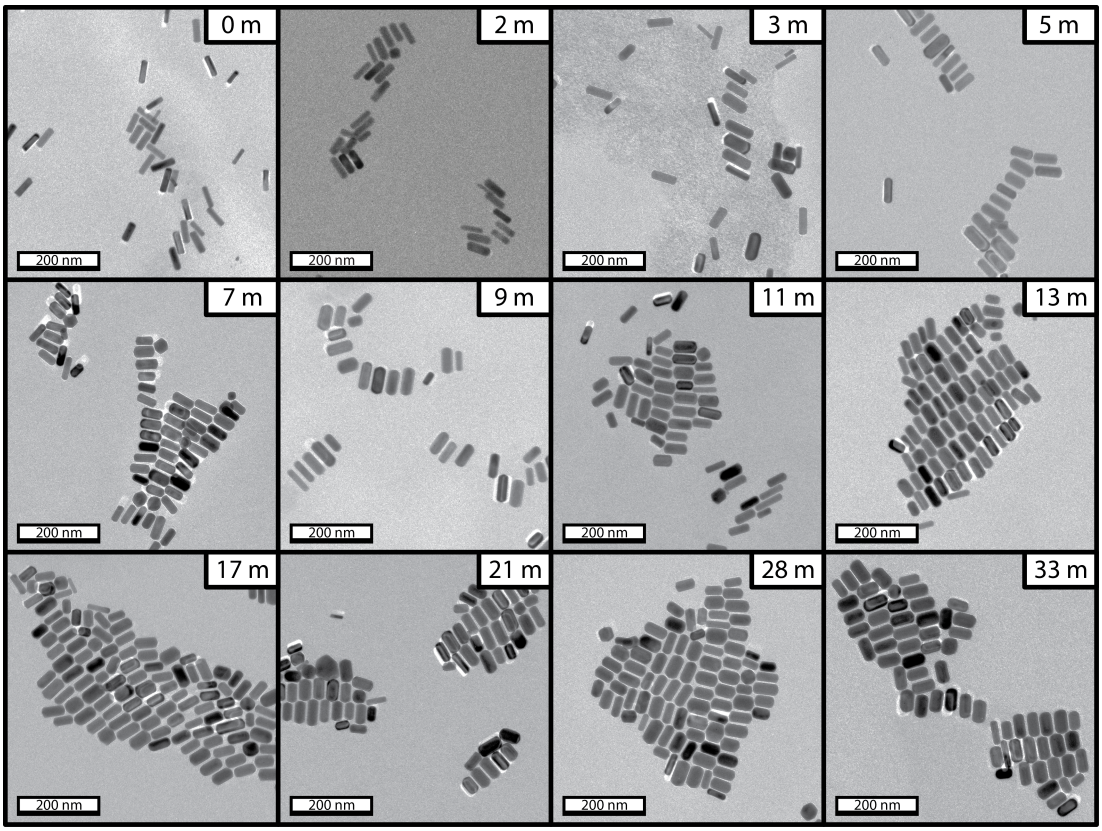

Figure 80: TEM micrographs showing progression from gold nanorods through gold nanonubs. The amount of time exposed to heat is indicated in each panel.

6.2.6 Gold Nanonubs (AuNN@CTAB)

Our lab has previously reported the photothermal reshaping of gold nanorods into spherical particles via laser ablation. [19] When the nanorods are excited by a high-powered laser, the plasmon resonance is generated, and the nanorods melt from the inside out. [20] Conversely, when gold nanorods are heat-treated at low concentration and in the presence of excess CTAB, they melt the same as a bulk material - from the outside in. Moreover, this process is slower and occurs in all particles in the solution at once, rather than just the particles in the path of the laser beam. This slower timescale allows for the reaction to be arrested at any point during the melting, producing gold nanonubs (Figure 80).

Gold nanonubs were synthesized via controlled thermal melting of AuNR@CTAB

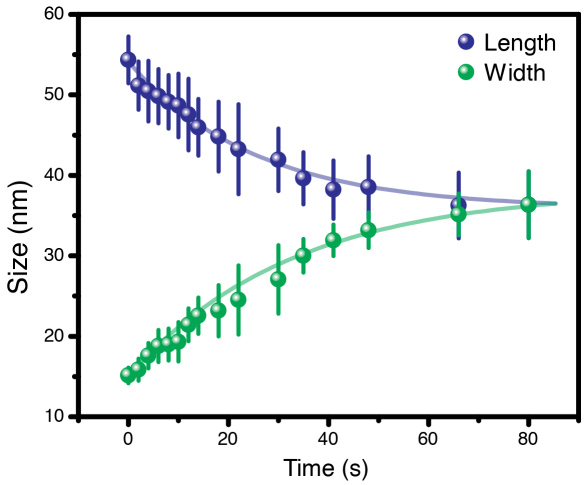

Figure 81: Length and width of gold nanonubs over time. These nanorods become shorter and fatter as they thermally melt, finally producing nanospheres.

prepared as described in 6.2.5. A solution of CTAB (0.31g, 100 mL) was prepared and heated to a gentle boil under gentle stirring (400 rpm) in a 250 mL trace-clean Erlenmeyer flask. The as-prepared AuNR@CTAB solution (25 mL) was injected, and heating/stirring was continued until the desired aspect ratio was achieved. The change in aspect ratio was monitored through observation of the longitudinal plasmon resonance peak (ca. 800 nm), which moved exponentially slowly toward the transverse plasmon resonance peak (ca. 530 nm). Evidence of this change is apparent in the color of the solution, which progresses from brown to purple to blue/green to red over the course of the rod-to-sphere transformation. AuNN appear blue/green in color. The resulting nanoparticles were cleaned via 2x centrifugation with water.

We observed this thermal reshaping of nanorods over time via UV-vis and TEM. The progression produces increasingly shorter and fatter rods, or nubs, until spheres are finally formed. This shape progression is shown visually in Figure 80, and the dimensions of the rods formed are given in Figure 81.

Optically, the longitudinal plasmon band blue-shifts significantly as the rod length shortens. The transverse plasmon resonance concurrently red-shifts to a much lesser degree. This effect is seen in the experimental extinction spectra in Figure 82 and

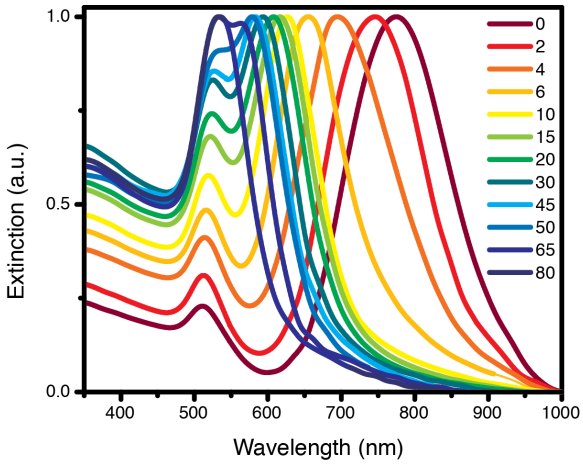

Figure 82: Extinction spectra showing thermal transition from gold nanorods through gold nanonubs to gold nanospheres. The longitudinal plasmon resonance blue-shifts while the transverse plasmon resonance red-shifts slightly.

reproduced in the theoretical DDA spectra in Figure 83, which were calculated for the specific dimensions observed in the TEM experiments.

If each particle simply reformed into a spherical shape independently of other particles in the solution, the starting gold nanorods would produce ca. 18 nm gold nanospheres. However, the TEM results indicate the formation of particles of increasingly larger volume; the final nanospheres are ca. 36 nm in diameter. This indicates Ostwald ripening-type behavior [39] in the thermal melting process; some nanoparticles are shrinking and some growing in volume as atoms move from one nanoparticle into solution and nucleate onto another particle. The smaller, shrinking rods are apparent in the TEM images (Figure 80), though there are far more growing nubs than shrinking nubs, as reflected in the error bars on the length/width over time plot in Figure 81. We monitored the thermal melting of gold nanorods at various temperatures in order to calculate an activation energy for this Ostwald reshaping process. The Arrhenius plot is given in Figure 84, indicating an activation energy of 29.78 J.

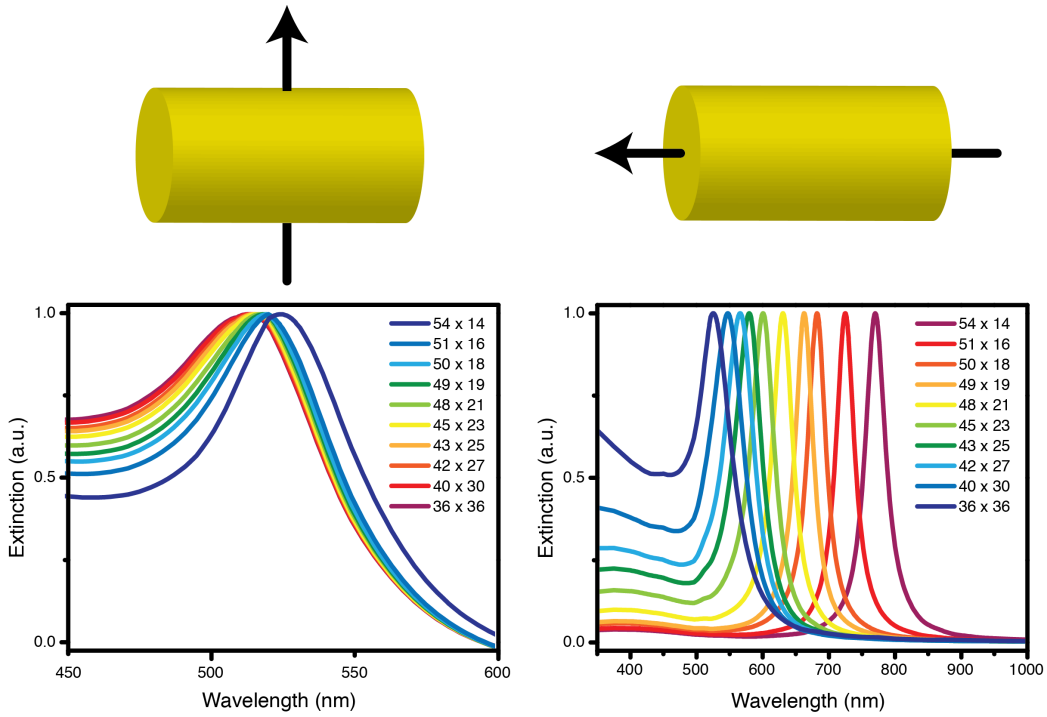

Figure 83: Calculated DDA spectra of the transverse (left) and longitudinal (right) plasmon resonance for gold nanorods of the indicated dimensions. Transvers and longitudinal polarization modes are indicated with black arrows on the schematic rods over each plot. The longitudinal plasmon band blue-shifts significantly while the transverse plasmon band red-shifts slightly. Thus, the experimental and theoretical results are mutually reinforcing.

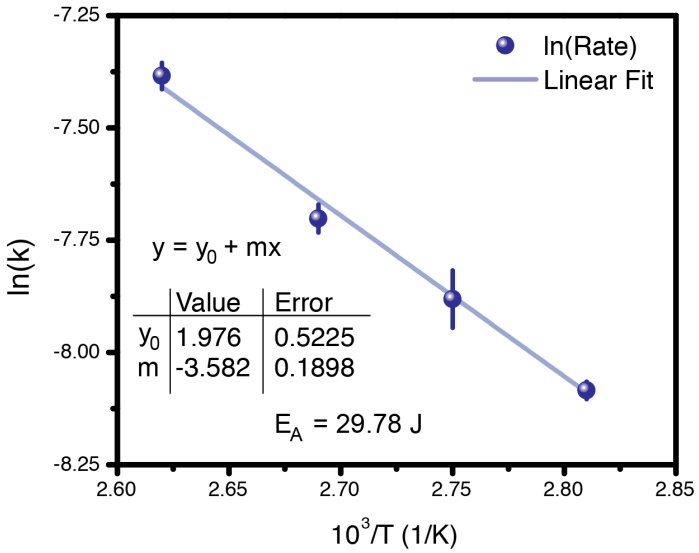

Figure 84: Arrhenius plot of the logged rate constant versus temperature. Rate constant attained from peak shift over time for thermally melted gold nanorods. Indicates an activation energy of 29.78 J for the Ostwald ripening process responsible for the thermal, outside-in reshaping of gold nanorods into gold nanospheres.

6.2.7 Gold Nanoframes (AuNF)

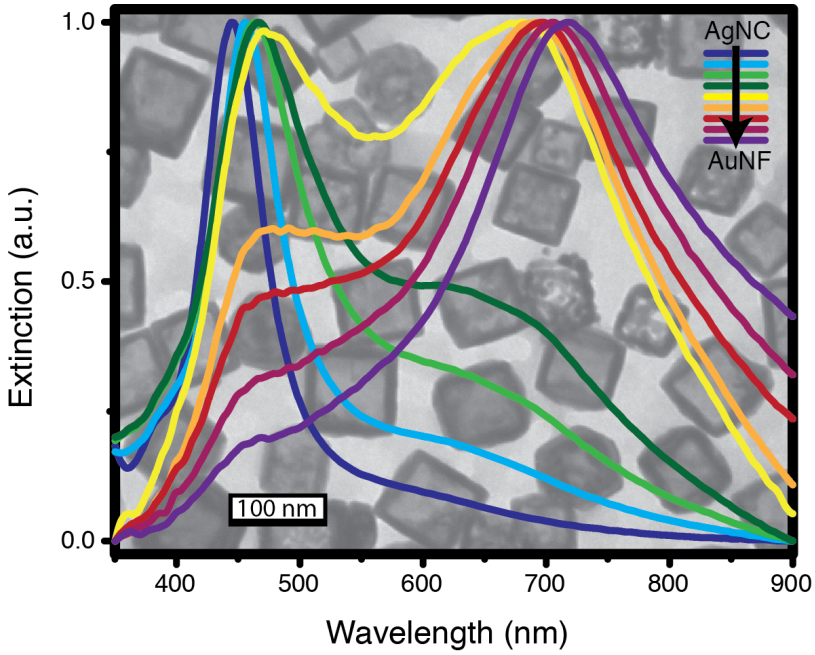

Figure 85: Transmission electron micrograph of gold nanoframes (ca. 40 nm) capped with PVP.

6.2.7.1 AuNF@PVP

Gold nanoframes (ca. 40 nm edge length) were prepared using the silver nanocubes whose synthesis is described in Section 6.2.2 as templates for this galvanic replacement reaction. The AgNC template nanoparticles were first cleaned of excess PVP via dispersion in water (1:1), centrifugation into a pellet, redispersion to the original volume in water, and recentrifugation. The resulting pellets were collected and dispersed in water (ca. 100 mL) in a three-necked round-bottom flask. The reaction vessel was heated in an oil bath at 150 °C with stirring, and tetrachloroaurate solution (ca. 1 wt.%) was added drop-wise. The growth of these gold nanoframes was monitored after each addition of gold solution and is witnessed by the spectral shift of the plasmon peak from ca. 430 nm (AgNC) to ca. 800 nm (AuNF, Figure 85).

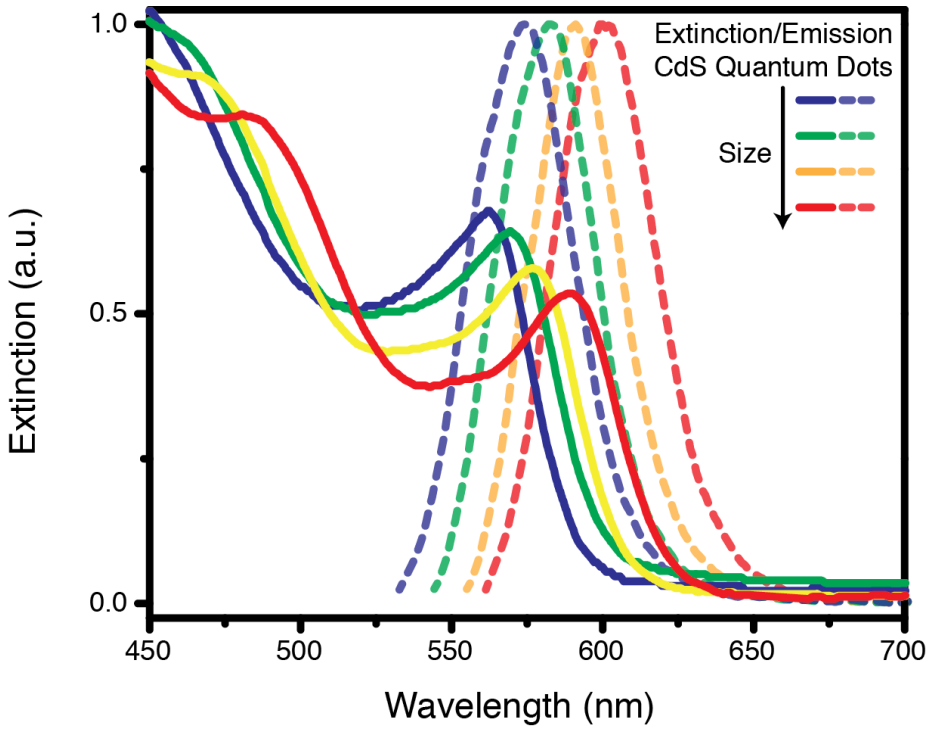

Figure 86: Extinction (solid lines) and corresponding emission (dashed lines) spectra for CdS quantum dots of increasing size. Emission red-shifts with increasing particle size.

6.2.8 Nanoparticle Analysis

Nanoparticles onto carbon-coated copper TEM grids via the vertical drying method. They were then imaged at a magnification of 100,000x using a JEOL 100-CX TEM operated at an acceleration voltage of 100 kV and equipped with a CCD camera. UV-vis exctinction spectra were collected with an Ocean Optics HR4000CG-UV-NIR.

6.3 Colloidal Syntheses of Selected Quantum Dots

6.3.1 Cadmium Selenide and Zinc Sulfide Shell QDs

6.3.1.1 CdSe@TOPO

Cadmium selenide quantum dot nanoparticles were synthesized by first dissolving cadmium oxide (0.3 g) in stearic acid (2.0 g) in inert atmosphere to form an opaque rust-red colored solution. This solution was heated in a three-necked round-bottom flask to 180 °C, at which point it became clear and nearly colorless. Trioctyl-phosphine

oxide (TOPO, 2.0 g) and hexadecylamine (2.0 g) were added, and the reaction mixture was heated to 200 °C. In a separate vial, selenium powder (0.3 g) was added to trioctylphosphine (3-4 mL) and heated until dissolution. The selenium solution was then injected all at once into the reaction vessel. Aliquots of solution were removed and dispersed in toluene (ca. 8 mL) at regular intervals to quench growth. Longer growth times yield quantum dots with a more red-shifted absorption edge and emission wavelength. Methanol (ca. 2 mL) was added to each aliquot until the quantum dots began to precipitate, and the solutions were centrifuged. The supernatant was discarded, and the quantum dots were redispersed in either toluene (for storage) or trioctylphosphine (TOP, for subsequent coating with zinc sulfide).

6.3.1.2 CdSe/ZnS@TOPO

A zinc sulfide shell was added to CdSe quantum dots described in the previous subsection to improve their quantum efficiency. Sulfur powder (0.05 g) was combined with TOP (3 mL) and mixed until dissolution was achieved. This sulfur solution was set to the side. Next, zinc acetate was prepared by combining zinc salt with acetile acetone, refluxing, isolating with methanol, and decanting. In a separate reaction vessel, zinc acetate (0.05 g) was dissolved in oleic acid (3 mL) and heated to 170 °C. TOPO (1.0 g) and CdSe quantum dots were added to the reaction vessel followed by the drop-wise addition of the previously-prepared sulfur solution. Aliquots were removed periodically and injected into toluene (ca. 8 mL) to quench their growth.

6.3.2 QD Analysis

The vertical drying method was used to deposit the quantum dots onto carbon-coated copper TEM grids, which were then screened at a magnification of 100,000x using a JEOL 100-CX TEM operated at an acceleration voltage of 100 kV and equipped with a CCD camera. Optical characterization was performed as follows: UV-vis xctinction spectra were collected with an Ocean Optics HR4000CG-UV-NIR, and

steady state photoluminescence data were collected using a Shimadzu Fluorimeter model RF-5301PC.

6.4 TiO_2 Photoanode Fabrication and Modification

6.4.1 Electrochemical Anodization of TiO_2 Nanotubes

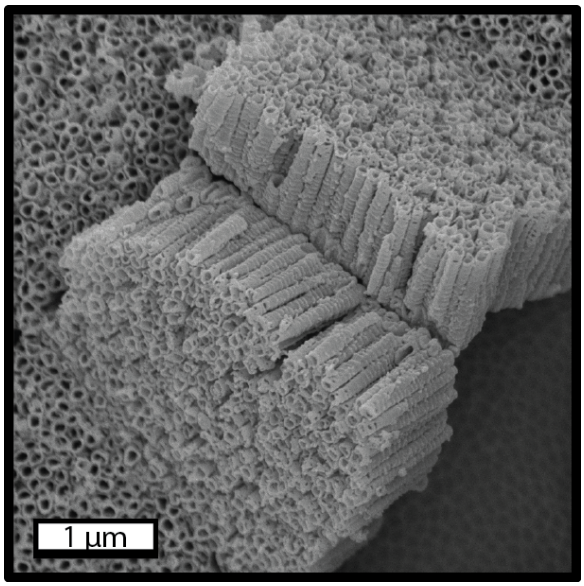

Figure 87: SEM image of TiO_2 Nanotubes.

Electrolyte solution was prepared by dissolving ammonium fluoride (0.7 g) and phosphoric (H_3PO_4) acid (3 mL) in water (100 mL) to form a 0.2 wt.% fluoride solution. Here, the ammonium fluoride was first dissolved in ca. 5 mL water and bridged into the main solution. Titanium foil was cleaned via sonication in ethanol (1 hr) followed by sonication in water (1 hr) and drying under N_2. The electrochemical cell was set up with the clean titanium foil as the working (+) electrode and platinum foil as the counter (-) electrode. The voltage across the cell was increased from 0 to 20 V steadily over 30 seconds and held at 20 V for 8 hours. The resulting nanotube arrays were cleaned via sonication (DI water, ca. 3 seconds) followed by an acid soak (HCl, 1.0 M, 1 hr). The NTs were annealed either by oxygen annealing (500 °C) or nitrogen annealing (450 °C) - depending on the desired optical properties - using a

heating and cooling rate of 1 °C/min. An SEM micrograph of the resulting nanotubes is shown in Figure 87.

6.4.2 QD Deposition/Attachment to TiO_2 NT Arrays

CdS was deposited on the crystallized nanotube surfaces by the successive chemical bath deposition (CBD) method. The NT array was immersed in $CdSO_4$ (0.2 M) for 1 min, rinsed with DI water, immersed in Na_2S (0.2 M), then rinsed again with DI water. This process was repeated 1-3 times, resulting in the formation of a layer of CdS crystallites on the nanotube surface.

6.4.3 TiO_2 Photoanode Analysis

The morphology of the samples was examined using a Zeiss SEM Ultra60. X-ray photoelectron spectroscopy (XPS) experiments were performed on the TiO_2 as well as the hybrid films using a Thermo Scientific K-alpha XPS with an Al anode. The optical characterization of the films was performed using a Shimadzu UV-Vis-NIR spectrophotometer UV-3101PC.

6.5 REFERENCES

[1] Ahmadi, T. S., Wang, Z. L., Henglein, A., and ElSayed, M. A., ""cubic" colloidal platinum nanoparticles," *Chemistry of Materials*, vol. 8, no. 6, pp. 1161–and, 1996. Ahmadi, TS Wang, ZL Henglein, A ElSayed, MA.

[2] Ahmadi, T., Wang, Z., Green, T., Henglein, A., El-Sayed, M., and others, "Shape-controlled synthesis of colloidal platinum nanoparticles," *SCIENCE-NEW YORK THEN WASHINGTON-*, pp. 1924–1925, 1996.

[3] Bardhan, R., Grady, N., Cole, J., Joshi, A., and Halas, N., "Fluorescence enhancement by au nanostructures: nanoshells and nanorods," *ACS nano*, vol. 3, no. 3, pp. 744–752, 2009.

[4] Ben Moshe, A. and Markovich, G., "Synthesis of single crystal hollow silver nanoparticles in a fast reaction-diffusion process," *Chemistry of Materials*, vol. 23, no. 5, pp. 1239–1245, 2011.

[5] Brust, M., Walker, M., Bethell, D., Schiffrin, D. J., and Whyman, R., "Synthesis of thiol-derivatized gold nanoparticles in a 2-phase liquid-liquid system," *Journal of the Chemical Society-Chemical Communications*, no. 7, pp. 801–802, 1994.

[6] Cheng, J., Ross, C., Smith, H., and Thomas, E., "Templated self-assembly of block copolymers: Top-down helps bottom-up," *Advanced Materials*, vol. 18, no. 19, pp. 2505–2521, 2006.

[7] Chung, S., Ginger, D., Morales, M., Zhang, Z., Chandrasekhar, V., Ratner, M., and Mirkin, C., "Top-down meets bottom-up: Dip-pen nanolithography and dna-directed assembly of nanoscale electrical circuits," *small*, vol. 1, no. 1, pp. 64–69, 2004.

[8] Ensign, D., Young, M., and Douglas, T., "Photocatalytic synthesis of copper colloids from cu (ii) by the ferrihydrite core of ferritin," *Inorganic chemistry*, vol. 43, no. 11, pp. 3441–3446, 2004.

[9] Freund, P. and Spiro, M., "Colloidal catalysis: the effect of sol size and concentration," *The Journal of Physical Chemistry*, vol. 89, no. 7, pp. 1074–1077, 1985.

[10] Gerion, D., Pinaud, F., Williams, S. C., Parak, W. J., Zanchet, D., Weiss, S., and Alivisatos, A. P., "Synthesis and properties of biocompatible water-soluble silica-coated cdse/zns semiconductor quantum dots," *Journal of Physical Chemistry B*, vol. 105, no. 37, pp. 8861–8871, 2001. ISI Document Delivery No.: 473GR Times Cited: 601 Cited Reference Count: 32 Amer chemical soc Washington.

[11] Giuffrida, S., Costanzo, L., Ventimiglia, G., and Bongiorno, C., "Photochemical synthesis of copper nanoparticles incorporated in poly (vinyl pyrrolidone)," *Journal of Nanoparticle Research*, vol. 10, no. 7, pp. 1183–1192, 2008.

[12] Grzelczak, M., Pérez-Juste, J., Mulvaney, P., and Liz-Marzán, L., "Shape control in gold nanoparticle synthesis," *Chem. Soc. Rev.*, vol. 37, no. 9, pp. 1783–1791, 2008.

[13] Hawker, C. and Russell, T., "Block copolymer lithography: Merging "bottom-up" with "top-down" processes," *MRS bulletin*, vol. 30, no. 12, pp. 952–966, 2005.

[14] Hernández, J., Solla-Gullón, J., Herrero, E., Feliu, J., and Aldaz, A., "In situ surface characterization and oxygen reduction reaction on shape-controlled gold nanoparticles," *Journal of nanoscience and nanotechnology*, vol. 9, no. 4, pp. 2256–2273, 2009.

[15] Huang, X. H., Neretina, S., and El-Sayed, M. A., "Gold nanorods: From synthesis and properties to biological and biomedical applications," *Advanced Materials*, vol. 21, no. 48, pp. 4880–4910, 2009. Huang, Xiaohuo Neretina, Svetiana El-Sayed, Mostafa A.

[16] Jain, P. K. and El-Sayed, M. A., "Surface plasmon coupling and its universal size scaling in metal nanostructures of complex geometry: Elongated particle pairs and nanosphere trimers," *The Journal of Physical Chemistry C*, vol. 112, no. 13, pp. 4954–4960, 2008. doi: 10.1021/jp7120356.

[17] Jana, N., Gearheart, L., Obare, S., and Murphy, C., "Anisotropic chemical reactivity of gold spheroids and nanorods," *Langmuir*, vol. 18, no. 3, pp. 922–927, 2002.

[18] Li, Y., Boone, E., and El-Sayed, M. A., "Size effects of pvp-pd nanoparticles on the catalytic suzuki reactions in aqueous solution," *Langmuir*, vol. 18, no. 12, pp. 4921–4925, 2002. Li, Y Boone, E El-Sayed, MA.

[19] Link, S., Burda, C., Mohamed, M. B., Nikoobakht, B., and El-Sayed, M. A., "Laser photothermal melting and fragmentation of gold nanorods: Energy and laser pulse-width dependence," *Journal of Physical Chemistry A*,

vol. 103, no. 9, pp. 1165–1170, 1999. Link, S Burda, C Mohamed, MB Nikoobakht, B El-Sayed, MA.

[20] Link, S., Burda, C., Nikoobakht, B., and El-Sayed, M., "How long does it take to melt a gold nanorod?: A femtosecond pump–probe absorption spectroscopic study," *Chemical Physics Letters*, vol. 315, no. 1, pp. 12–18, 1999.

[21] Link, S. and El-Sayed, M., "Size and temperature dependence of the plasmon absorption of colloidal gold nanoparticles," *The Journal of Physical Chemistry B*, vol. 103, no. 21, pp. 4212–4217, 1999.

[22] Link, S., Wang, Z. L., and El-Sayed, M. A., "Alloy formation of gold-silver nanoparticles and the dependence of the plasmon absorption on their composition," *Journal of Physical Chemistry B*, vol. 103, no. 18, pp. 3529–3533, 1999. Link, S Wang, ZL El-Sayed, MA.

[23] Mahmoud, M. and El-Sayed, M., "Comparative study of the assemblies and the resulting plasmon fields of langmuir- blodgett assembled monolayers of silver nanocubes and gold nanocages," *The Journal of Physical Chemistry C*, vol. 112, no. 37, pp. 14618–14625, 2008.

[24] Millstone, J., Park, S., Shuford, K., Qin, L., Schatz, G., and Mirkin, C., "Observation of a quadrupole plasmon mode for a colloidal solution of gold nanoprisms," *Journal of the American Chemical Society*, vol. 127, no. 15, pp. 5312–5313, 2005.

[25] Murray, C. B., Norris, D. J., and Bawendi, M. G., "Synthesis and characterization of nearly monodisperse cde (e = s, se, te) semiconductor nanocrystallites," *Journal of the American Chemical Society*, vol. 115, no. 19, pp. 8706–8715, 1993. ISI Document Delivery No.: LZ133 Times Cited: 3354 Cited Reference Count: 48.

[26] Narayanan, R. and El-Sayed, M. A., "Shape-dependent catalytic activity of platinum nanoparticles in colloidal solution," *Nano Letters*, vol. 4, no. 7, pp. 1343–1348, 2004. Narayanan, R El-Sayed, MA.

[27] Niesz, K., Grass, M., and Somorjai, G., "Precise control of the pt nanoparticle size by seeded growth using eo13po30eo13 triblock copolymers as protective agents," *Nano letters*, vol. 5, no. 11, pp. 2238–2240, 2005.

[28] Nikoobakht, B. and El-Sayed, M., "Evidence for bilayer assembly of cationic surfactants on the surface of gold nanorods," *Langmuir*, vol. 17, no. 20, pp. 6368–6374, 2001.

[29] Nikoobakht, B. and El-Sayed, M., "Preparation and growth mechanism of gold nanorods (nrs) using seed-mediated growth method," *Chemistry of Materials*, vol. 15, no. 10, pp. 1957–1962, 2003.

[30] Nikoobakht, B., Wang, Z., and El-Sayed, M., "Self-assembly of gold nanorods," *The Journal of Physical Chemistry B*, vol. 104, no. 36, pp. 8635–8640, 2000.

[31] Petroski, J. M., Wang, Z. L., Green, T. C., and El-Sayed, M. A., "Kinetically controlled growth and shape formation mechanism of platinum nanoparticles," *Journal of Physical Chemistry B*, vol. 102, no. 18, pp. 3316–3320, 1998. Petroski, JM Wang, ZL Green, TC El-Sayed, MA.

[32] Prodan, E., Radloff, C., Halas, N., and Nordlander, P., "A hybridization model for the plasmon response of complex nanostructures," *Science*, vol. 302, no. 5644, pp. 419–422, 2003.

[33] Ren, J. and Tilley, R., "Shape-controlled growth of platinum nanoparticles," *Small*, vol. 3, no. 9, pp. 1508–1512, 2007.

[34] Sawoo, S., Srimani, D., Dutta, P., Lahiri, R., and Sarkar, A., "Size controlled synthesis of pd nanoparticles in water and their catalytic application in c–c coupling reactions," *Tetrahedron*, vol. 65, no. 22, pp. 4367–4374, 2009.

[35] Sherry, L., Chang, S., Schatz, G., Van Duyne, R., Benjamin, J., and Xia, Y., "Localized surface plasmon resonance spectroscopy of single silver nanocubes," *Nano Letters*, vol. 5, no. 10, pp. 2034–2038, 2005.

[36] Sun, Y. and Xia, Y., "Shape-controlled synthesis of gold and silver nanoparticles," *Science*, vol. 298, no. 5601, pp. 2176–2179, 2002.

[37] Thomas, J. and Raja, R., "Nanopore and nanoparticle catalysts," *The Chemical Record*, vol. 1, no. 6, pp. 448–466, 2001.

[38] Turkevich J, Stevenson P, H. J., "A study of the nucleation and growth processes in the synthesis of colloidal gold," *Discuss. Faraday Soc.*, vol. 11, pp. 55–75, 1951.

[39] Voorhees, P., "The theory of ostwald ripening," *Journal of Statistical Physics*, vol. 38, no. 1, pp. 231–252, 1985.

[40] Yong, K., Swihart, M., Ding, H., and Prasad, P., "Preparation of gold nanoparticles and their applications in anisotropic nanoparticle synthesis and bioimaging," *Plasmonics*, vol. 4, no. 2, pp. 79–93, 2009.

[41] Zhang, W., Qiao, X., and Chen, J., "Synthesis of silver nanoparticlesóeffects of concerned parameters in water/oil microemulsion," *Materials Science and Engineering: B*, vol. 142, no. 1, pp. 1–15, 2007.

[42] Zhou, J., Ralston, J., Sedev, R., and Beattie, D., "Functionalized gold nanoparticles: synthesis, structure and colloid stability," *Journal of Colloid and Interface Science*, vol. 331, no. 2, pp. 251–262, 2009.

APPENDIX A

NANOPROBE ANCILLARY MATERIAL

A.1 Synthesis of hexyl-substituted, ammonium-functionalized thiol ligand.

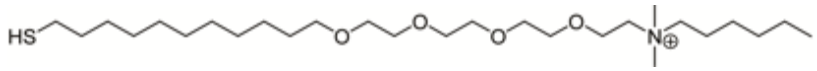

Figure 88: Schematic showing structure of cationic, hydrophobic Ligand 1

The 400 MHz ^{1}H NMR spectra of the above ligand was reported previously. [3] We have employed electrospray ionization mass spectrometry (ESI-MS) to further confirm the purity of the ligand (m/z 492, Figure 89).

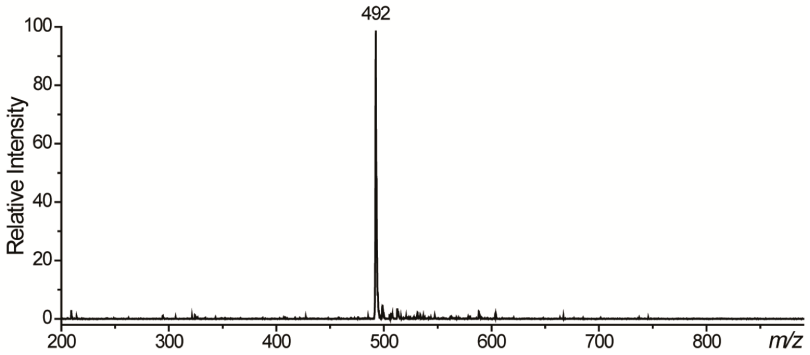

Figure 89: Mass Spectrum of Ligand 1.

A.2 Synthesis of 2 nm metal core cationic gold nanoparticles (NP2)

Pentanethiol-capped gold nanospheres with core diameters of 2 nm were synthesized via the traditional Brust-Schiffrin reduction. [1] Gold (III) chloride trihydrate (1.00 g, 2.54 mmol) was placed in a 1000 mL oven-dried, one-neck round bottom flask and dissolved in deionized water (150 mL) to yield a light yellow solution. Toluene

(150 mL) was added to the mixture and vigorously stirred. Tetraoctylammonium bromide (TOAB, 2.10 g, 3.81 mmol) was added to the two-phase solution and stirred vigorously for 15 min at room temperature, during which the solution turned orange. Pentanethiol (0.323 g, 0.38 mL) was added, and stirring was continued for 5 min. Sodium borohydrate ($NaBH_4$, 1.92 g) was dissolved in cold deionized water (10 mL) and quickly added to the solution. The solution immediately turned from orange to black, and stirring was continued for 5 h. The toluene layer was collected from a separation funnel and evaporated in a rotary evaporator at < 35 °C. A minimum amount of toluene was left in the round bottom flask (ca. 10 mL) and the material was transferred to a 2 L Erlenmeyer flask containing HPLC grade ethanol (1 L). The solution was left in the freezer overnight to allow the gold colloids to precipitate. The colloids were collected by filtration using ethanol as the washing solvent and were dried for ^{1}H NMR characterization. A TEM micrograph was taken to ensure the quality and monodispersity of the nanoparticles.

A place-exchange reaction [2] of ligand 1 (80.0 mg, 0.163 mmol, Figure 88) dissolved in dichloromethane (DCM, 10 mL) with pentanethiol-coated gold nanoparticles (diameter ca. 2 nm, 20 mg) was carried out for 3 days at room temperature. The DCM was then evaporated under reduced pressure. The residue was dissolved in a small amount (ca. 5 mL) of distilled water and dialyzed (membrane molecular weight cutoff (MWCO) = 10,000) to remove excess ligands, acetic acid, and salts present in the nanoparticle solution. After dialysis, the particles were lyophilized to obtain a brownish solid product and redispersed in deionized water (18 MΩ-cm). ^{1}H NMR spectra in D_2O showed substantial broadening of the proton signals, and no free ligands were observed. Nanoparticle quality was ensured with measurements from TEM, dynamic light scattering, zeta potential, mass spectrometry, and UV-vis spectroscopy.

A.3 Synthesis of 6 nm metal core cationic AuNPs (NP1)[1]

Undecanethiol-capped gold nanospheres with core diameters of 6 nm were synthesized via the heat-induced size evolution method. [4] In a 250 mL round bottom flask, TOAB (267 mg) in toluene (50 mL) was combined with gold (III) chloride trihydrate (100 mg) in deionized water (50 mL) and vigorously stirred. Undecanethiol (54 μL) was added, and the two-phase mixture was stirred for 10 min. Sodium borohydride ($NaBH_4$, 93 mg) in cold deionized water (5 mL) was added quickly, and the solution was stirred vigorously for 5 h. The toluene layer was collected and evaporated in a rotary evaporator at less than 35 ^{o}C. A minimum amount of toluene (ca. 5 mL) was left in the 250 mL round bottom flask. The product was transferred to a 25 mL round bottom flask and evaporated to dryness using a rotary evaporator and a high vacuum system overnight. This process yielded a layer of dried material that was evenly distributed on the wall of the flask.

The crude product in the 25 mL round bottom flask was heated to 150 °C using a temperature ramp under argon (10 ^{o}C every 5 min) until 150 ^{o}C was reached and maintained for 30 min. The product was allowed to cool to room temperature (dried thin layer looks golden) and dissolved in a mix of toluene (5 mL) and methanol (500 mL). The solution was put into the freezer overnight to allow the gold colloids to precipitate and to remove excess undecanethiol and TOAB. Isolation of AuNPs was achieved by decanting the methanol, and the colloids were dissolved in a minimal amount of toluene ($<$ 5 mL) for storage. ^{1}H NMR was used to characterize the capping molecule, and TEM was taken to ensure the quality and monodispersity of the nanoparticles.

A place-exchange reaction [2] of Ligand 1 (100 mg, 0.203 mmol, Figure 88) dissolved in DCM (10 mL) with undecanethiol-coated gold nanoparticles (diameter ca. 6 nm, 20 mg) was carried out for 3 days at room temperature. The DCM was evaporated under reduced pressure. The residue was dissolved in a small amount of distilled

water and dialyzed (membrane MWCO = 10,000) to remove excess ligands, acetic acid, and salts present in the nanoparticle solution. After dialysis, the particles were lyophilized to obtain a brownish solid product and redispersed in deionized water (18 MΩ-cm). ^{1}H NMR spectra in D_2O showed substantial broadening of the proton signals, and no signals due to free ligands were observed. TEM, dynamic light scattering, zeta potential, mass spectra, and UV-vis spectra were also taken to ensure the quality of the nanoparticles.

Zeta potentials of **NP1** and **NP2** were measured using a Malvern Zetasizer (Nano series, Malvern Instruments Inc, USA) in 5 mM phosphate buffer (pH=7.4) (Figure 90).

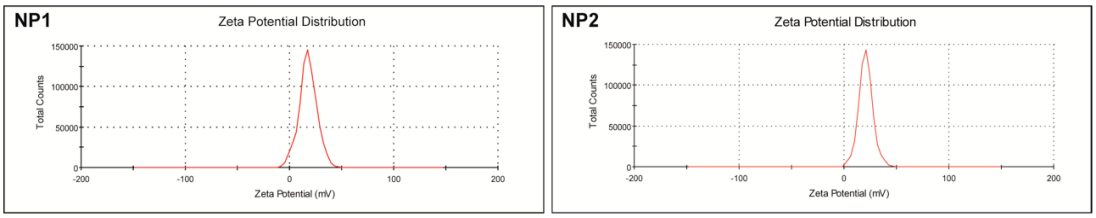

Figure 90: Zeta Potentials of **NP1** and **NP2**.

A.4 Bacteria growth and preparation

Strains of both *Escherichia coli* (*E. coli* XL1 Blue; Gram-negative) and *Bacillus subtilis* (*B. subtilis*; Gram-positive) bacteria were cultured in lysogeny broth (LB) growth medium and successively washed via centrifugation with 5 mM PBS (pH 7.4). Surface protein-denatured bacteria of each strain were prepared by resuspending the washed bacteria back to their original volume in 1% trypsin solution and shaking for 24 hours at 37 ^{o}C. Both the trypsin-treated and untreated samples of each bacteria were adjusted to an OD of 0.33, while the solutions of concentrated nanoparticles were diluted with PBS buffer to a concentration of 0.33 μM. These solutions were used throughout the following experiments.

A.5 Aggregation of AuNPs on the bacterial surface using UV-VIS spectroscopy

In a 5 mL cuvette, a solution containing 6 nm nanoparticles (0.1 mL, 0.33 μM) was added to bacteria stock solution (0.3 mL, $OD_{600nm} = 0.33$) at room temperature and mixed. Timing was begun at injection. A UV-Vis spectrum was recorded every 10 s for 1000 s using an Ocean Optics HR4000CG-UV-NIR, and the shift in the plasmonic peak at ca. 530 nm was monitored as a function of time. A filter was used to eliminate light of wavelengths shorter than 400 nm in an effort to preserve bacterial health for the duration of the experiment.

A.6 TEM Studies

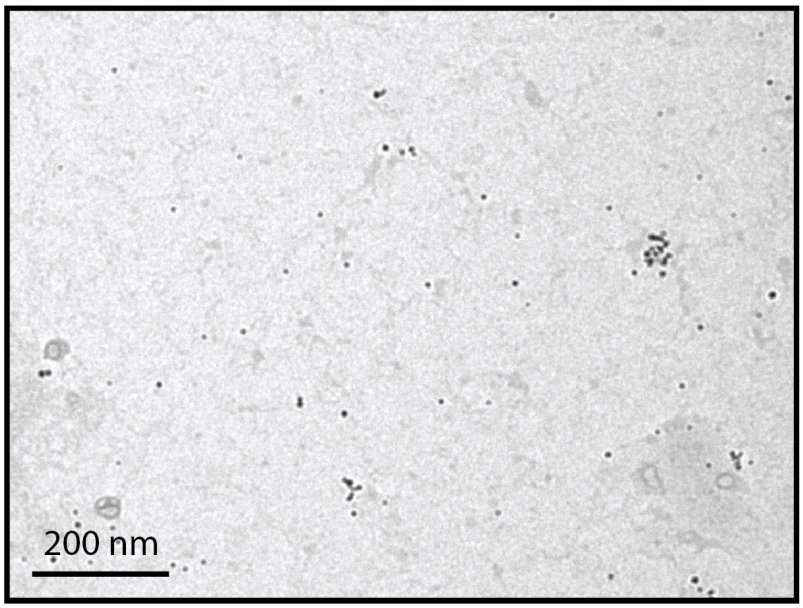

Figure 91: Transmission electron micrograph of AuNPs in fresh growth medium. Crystals are dried salts. No significant aggregation is observed, as corroborated in the spectroscopic studies.

For TEM grid preparation, the bacteria solution (30 μL, $OD_{600nm} = 0.33$) was mixed with nanoparticle solution (10 μL, 0.33 μM) at room temperature. After 20 s, aliquots of the mixture were removed and applied to a carbon-coated Cu grid (400-mesh) at time intervals ranging from 0 to 30 min. Aliquots of 2 μL were allowed

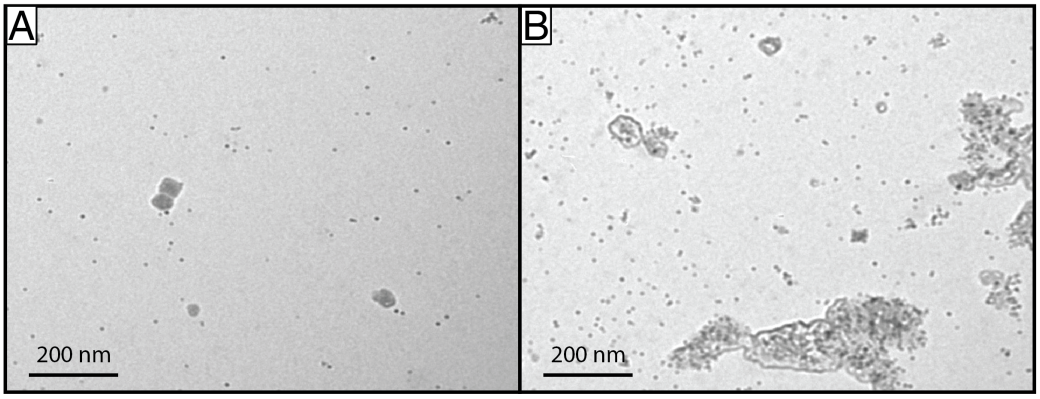

Figure 92: [Transmission electron micrograph of AuNPs in used growth media following centrifugation and removal of the *B. subtilis* (**A**) and *E. coli* (**B**). Crystals are dried salts. No significant aggregation was observed, as corroborated in the spectroscopic studies.

to settle on the grid for 20 s and were then blotted with filter paper (Whatman #4), effectively preserving the system at specific time points. To distinguish the cell membranes, the grids were stained with 2 μL of 1% uranyl acetate for 30 s and then blotted again. To rule out artifacts, a series of control grids were prepared alongside the sample grids with a) cells that were stained, b) only AuNPs in growth media that were stained (Figure 91), c) AuNPs in used growth media after cells had been cultured and removed (Figure 92), and d) the AuNP-bacteria mixture without staining by uranyl acetate. All grids were then screened with a JEOL JEM-1400 TEM operated at an acceleration voltage of 120 kV and equipped with Gatan Orius SC1000 and Ultrascan 1000 CCD cameras. Images were collected at magnifications from 50,000x to 100,000x.

A.7 Cytotoxicity Assays

The extent of membrane damage/release of cytosolic glucose 6-phosphate dehydrogenase was quantified by Vybrant Cytotoxicity Assay Kit (Invitrogen, V-23111) according to manufacturer protocol at room temperature. The experiment includes several groups: PBS only, both *E. coli* and *B. subtilis* (OD_{600}=0.33) in PBS, bacteria with

NP (100 nM, 200 nM and 300 nM), bacteria with lysis buffer, NP only and substrate mixture only for the background correction. These reaction mixtures were incubated for 5 minutes at 37 ^{o}C and the fluorescence was measured in a SpectroMax M2 microplate reader (Molecular Device) for up to 600 seconds with excitation/emission: 563 nm/587 nm. Percentage of lysed cells was calculated taking fully lysed cells as 100% control.

A.8 REFERENCES

[1] Brust, M., Walker, M., Bethell, D., Schiffrin, D. J., and Whyman, R., "Synthesis of thiol-derivatized gold nanoparticles in a 2-phase liquid-liquid system," *Journal of the Chemical Society-Chemical Communications*, no. 7, pp. 801–802, 1994.

[2] Hostetler, M. J., Templeton, A. C., and Murray, R. W., "Dynamics of place-exchange reactions on monolayer-protected gold cluster molecules," *Langmuir*, vol. 15, no. 11, pp. 3782–3789, 1999. ISI Document Delivery No.: 201RY Times Cited: 371 Cited Reference Count: 36 Amer chemical soc Washington.

[3] Miranda, O. R., Chen, H. T., You, C. C., Mortenson, D. E., Yang, X. C., Bunz, U. H. F., and Rotello, V. M., "Enzyme-amplified array sensing of proteins in solution and in biofluids," *Journal of the American Chemical Society*, vol. 132, no. 14, pp. 5285–5289, 2010. ISI Document Delivery No.: 581VS Times Cited: 17 Cited Reference Count: 87 Miranda, Oscar R. Chen, Hung-Ting You, Chang-Cheng Mortenson, David E. Yang, Xiao-Chao Bunz, Uwe H. F. Rotello, Vincent M. NSF[DMI-0531171, CHE-0808945]; NIH[GM077173]; Department of Energy[DE-FG02-04ER46141] This work was supported by the NSF Center for Hierarchical Manufacturing at the University of Massachusetts Nanoscale Science and Engineering Center (NSEC, DMI-0531171), the NSF (V.M.R., CHE-0808945), and the NIH (GM077173). U.H.F.B. thanks the Department of Energy Grant for generous financial support (DE-FG02-04ER46141). Amer chemical soc Washington.

[4] Teranishi, T., Hasegawa, S., Shimizu, T., and Miyake, M., "Heat-induced

size evolution of gold nanoparticles in the solid state," *Advanced Materials*, vol. 13, no. 22, pp. 1699–1701, 2001. ISI Document Delivery No.: 494HY Times Cited: 115 Cited Reference Count: 22 Wiley-v c h verlag gmbh Berlin.

APPENDIX B

TITANIUM DIOXIDE ANCILLARY MATERIAL

B.1 Electrode Fabrication

The TiO_2 thin film electrode was prepared by annealing titanium foil at 500 °C for 6 hours in ambient air with a heating and cooling rate of 1 °C/min. The TiO_2 nanotubes (NTs) were fabricated as previously detailed in Chapter 6. Briefly, pure titanium foil samples were anodized in a two-electrode electrochemical cell with the titanium foil as the working electrode and platinum foil as the counter electrode (7 h, 20 V, ca. 22 °C) in an aqueous electrolyte (0.2 M NH_4F, 0.1 M H_3PO_4). The as-anodized samples were crystallized by oxygen annealing (500 °C) with a heating and cooling rate of 1 °C/min. CdS was deposited on the crystallized nanotube surfaces by the successive chemical bath deposition (CBD) method. [1] Briefly, the NT film was immersed in 0.2 M $CdSO_4$ solution for 1 min, rinsed with DI water and then immersed in 0.2 M Na_2S solution for 1 min and rinsed again with DI water. This process was repeated many times and resulted in the formation of CdS crystallites on the nanotube surface. The degree of surface coverage depends on the number of times the deposition is repeated. The morphology of the samples was examined using a Zeiss SEM Ultra60. The optical characterization of the films was performed using a Shimadzu UV-Vis-NIR spectrophotometer UV-3101PC.

B.2 Bacteria Growth and Analysis

Escherichia coli (*E. coli* XL1 Blue; Gram-negative) was cultured in Lysogeny broth (LB) growth medium (18 h, 37 °C) and then successively washed via centrifugation with 5 mM SO_4^{2-}. Cultures were then diluted to an $OD_{600nm} = 1.0$ with SO_4^{2-}

buffer for injection into the reaction vessel. Final bacteria percent survivability was determined by diluting with buffer and spreading a small amount uniformly onto nutrient agar plates (3 plate repeats per sample). The plates were incubated for 18 h at 37 °C, the colonies were counted, and the initial number of bacteria was calculated.

B.3 XPS Analysis

X-ray photoelectron spectroscopy (XPS) experiments were performed on the studied electrodes using a Thermo Scientific K-alpha XPS with an Al anode.

B.4 REFERENCES

[1] Nair, P., Nair, M., Garcia, V., Arenas, O., Peña, A., Ayala, I., Gomezdaza, O., Sanchez, A., Campos, J., Hu, H., and others, "Semiconductor thin films by chemical bath deposition for solar energy related applications," *Solar Energy Materials and Solar Cells*, vol. 52, no. 3, pp. 313–344, 1998.

APPENDIX C

BIOMIMETIC PHOTOVOLTAICS ANCILLARY MATERIAL

C.1 Bacteriorhodopsin (bR) Preparation

Standard preparation procedures [4] were used to culture bR from strain S9 of Halobacterium salinarium to provide a working concentration of 0.012 mM bR. The concentrated bR was stored at -10 °C until use. Water and citrate buffer (8.8 mM) were mixed appropriately to maintain bR at the same concentration throughout the experiments presented herein, and these mixtures were irradiated with white light prior to use to generate light-adapted bR.

C.2 Silver Nanoparticle Synthesis

All crystalline nanoparticles (spheres, cubes, and cuboids) were synthesized using the same chemicals, reaction vessels, heat settings, capping agents, and cleaning techniques as discussed in Chapter 6.

C.3 Photoelectric Cell Design

The experimental cell was adapted from Horn et al. [4] and has been previously discussed by our research group. [1] Bacteriorhodopsin and citrate buffer (either in the presence or absence of Ag nanoparticles) was deposited into an O-ring on ITO glass and covered with a Nafion membrane (0.09 mm, Alfa Aesar) to serve as the bR cell. Another O-ring was placed on top of the membrane and filled with citrate buffer solution to serve as the reference cell. A second piece of ITO glass over this O-ring completes the circuit and provides an optically transparent means of

sequestering the liquid components of the cell. The citrate buffer maintains the pH of both cells at 7.0 and provides for enhanced charge carrier separation. This effect was statistically significant but not quantified in this paper. The Nafion membrane allows for the movement of protons between the bR and reference cells but forbids bR, silver particle, and anion diffusion between cells. It is important to note here that this design offers the advantage of no needed external bias for polarity definition.

C.4 Photocurrent Measurements

A modulated CW broadband xenon arc lamp (UXL-75X, Ushio) was used as the excitation source (140 mW / cm^2, 10 mm spot size). The lamp was powered externally (LPS-220, PTI), and an optical fiber (long-pass at $\lambda > 380$ nm) was used to introduce the light to the bR cell. An external shutter (04IES001, Melles Griot), actuated electronically (04ISC001, Melles Griot), was used to modulate the light at a 0.83 Hz repetition rate for the short-term (sphere, 1.2 s) photocurrent experiments and at a 6.6 x 10^{-4} Hz repetition rate for the extended (cube, 1000 s) experiments. The experimental set-up is rendered in schematic in Figure 93.

The current signal output was amplified by an external current amplifier (Model-428, Keithley Instruments Inc.). The light-on / light-off signal was generated by collecting scattered light via a photodiode made in our lab, and this information was stored by a 500-MHz transient digitizer (9350A, LeCroy). The instantaneous incident excitation energy was monitored using a power meter (30A, Ophir). Dark incident photocurrent was collected before the addition of bR to eliminate any photoartifacts.

The photocurrent density in the presence of silver nanoparticles capped with different molecular weights of PVP was measured as follows. Bacteriorhodopsin, citrate buffer, and silver nanoparticles were mixed and covered with a Nafion membrane to serve as the bR working cell. On the other side of the membrane, citrate buffer solution served as the reference cell. The citrate buffer maintains the pH of both

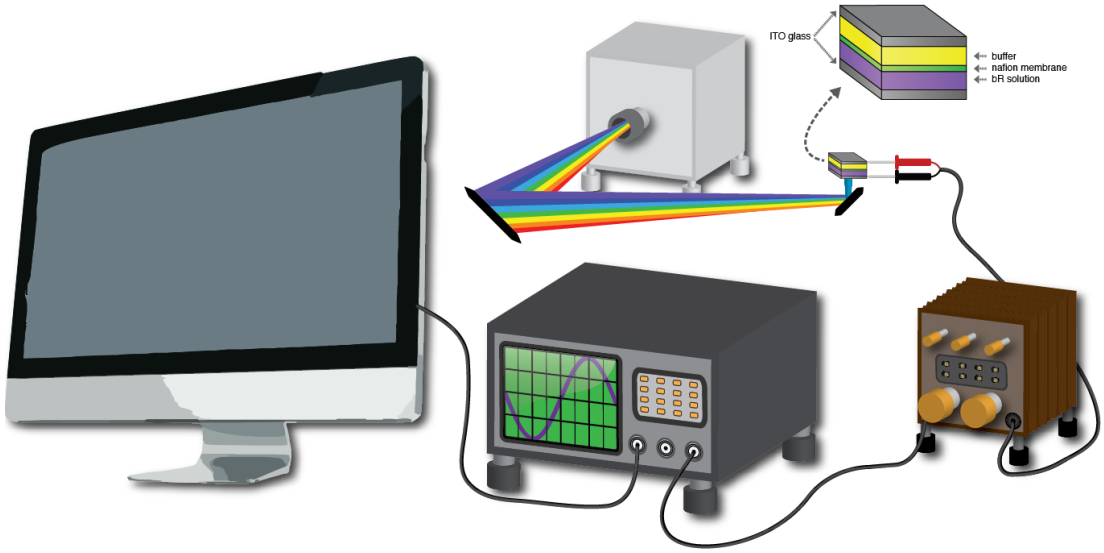

Figure 93: Experimental set-up for bR photocurrent measurements showing the cell, light-source, amplifier, oscilloscope, and computer used to collect data from the oscilloscope.

cells at 7.0 and provides for enhanced charge carrier separation. The photocurrent measurements were carried out under continuous wavelength white light with an external shutter and a signal amplifier. Dark incident photocurrent was collected before the addition of bR to eliminate any photoartifacts. This dark photocurrent density (0.8 nA/cm^3) was subtracted from the induced photocurrent values for bR reported herein.

C.5 Transmission Electron Microscopy

Silver nanoparticles were deposited onto carbon-coated copper TEM grids via the vertical drying method. All grids were then screened with a JEOL 100-CX TEM operated at an acceleration voltage of 100 kV and equipped with a CCD camera. Images were collected at a magnification of 100,000x.

C.6 Dynamic Light Scattering

DLS measurements were taken using a NanoZS Zetasizer particle analyzer (Malvern, 633 nm).

C.7 UV-Vis Spectra

All extinction spectra were acquired using an Ocean Optics HR4000CG-UV-NIR spectrometer.

C.8 Data Analysis

Photocurrent data analysis and spectral overlap integrations were preformed using the Origin Pro 7.0 software. All plots were also generated using this software.

C.9 Corner Integrity

Relative corner integrity of our cuboid structures was determined in ImageJ by fitting circles to the corners of the particles in TEM images. By this method, in spheres, a circle will fit the entire particle (0% integrity), and a circle of infinitely small radius will fit the corner of a perfect cube (100% integrity). For the cuboid shapes, circles with smaller radii will correspond to shapes with better corner integrity (Cuboid-B), and circles with larger radii will correspond to shapes that are more sphere-like (Cuboid-A). The radius of at least 250 circles was measured for Cuboid-A and Cuboid-B. 100 circles were measured for the spheres.

C.10 Discrete Dipole Approximation

DDA calculations were performed by Erik Dreaden in our group as described previously. [3] Briefly, electric field distribution and polarization contour plots were computed using modified FORTRAN codes of DDSCAT6.1 kindly provided by G.C. Schatz (Northwestern University). [2] Calculations were carried out for linearly polarized far-field excitation of Ag nanospheres (40 nm in diameter) or Ag nanocubes (40 nm face length) with equal dipole densities. The complex dielectric function for Ag was interpolated from experimental data and applied for a homogenous aqueous environment. [5]

C.11 REFERENCES

[1] Chu, L. K., Yen, C. W., and El-Sayed, M. A., "Bacteriorhodopsin-based photo-electrochemical cell," *Biosensors and Bioelectronics*, vol. 26, no. 2, pp. 620–626, 2010. Chu, Li-Kang Yen, Chun-Wan El-Sayed, Mostafa A.

[2] Draine, B. T. and Flatau, P. J., "Ddscat 6.1," 2005.

[3] Dreaden, E. C., Neretina, S., Qian, W., El-Sayed, M. A., Hughes, R. A., Preston, J. S., and Mascher, P., "Plasmonic enhancement of non-radiative charge carrier relaxation and proposed effects from enhanced radiative electronic processes in semiconductorâ'gold coreâ'shell nanorod arrays," *The Journal of Physical Chemistry C*, vol. 115, no. 13, pp. 5578–5583, 2011.

[4] Horn, C. and Steinem, C., "Photocurrents generated by bacteriorhodopsin adsorbed on nano-black lipid membranes," *Biophysical Journal*, vol. 89, no. 2, pp. 1046–1054, 2005. ISI Document Delivery No.: 949XM Times Cited: 20 Cited Reference Count: 41 Biophysical society Bethesda.

[5] Johnson, P. B. and Christy, R. W., "Optical constants of noble metals," *Physical Review B*, vol. 6, no. 12, pp. 4370–4379, 1972.

APPENDIX D

PHOTODYNAMIC CANCER THERAPY ANCILLARY MATERIAL

D.1 Nanoparticle Synthesis

All nanoparticles were synthesized according to the methods laid out in Chapter 6.

D.2 NP-PpIX Complex Synthesis

AgNS, AuNS, and AuNR were cleaned via successive centrifugation. Each of these was then combined with PpIX to generate solutions of each particle with each type of PpIX linker functionality: unmodified PpIX, Short-Linker PpIX, and Long-Linker PpIX. The concentration of NPs was maintained at 0.1 nM NPs for all solutions, while solutions of both 0.2 and 2.0 M PpIX were made for each mode of PpIX attachment.

Polyethylene glycol with methoxy and thiol terminii (mPEG-SH) was added to provide approximately 10% NP surface coverage in order to maintain good water solubility and improve biocompatibility. Final DMSO concentration was maintained at 0.2%, and this amount of DMSO showed no effect on cell viability by itself. NP-PpIX complexes were characterized using UV-Vis, TEM, and Dynamic Light Scattering (DLS).

D.3 Transmission Electron Microscopy (TEM)

The vertical drying method was used to deposit nanoparticles onto carbon-coated copper TEM grids, which were then screened at a magnification of 100,000x using a JEOL 100-CX TEM operated at an acceleration voltage of 100 kV and equipped with a CCD camera.

D.4 Discrete Dipole Approximation (DDA)

The optical responses of the various nanoparticles were calculated by Rachel D. Near in our group using the DDA method with the DDSCAT 6.1 code offered publicly by Draine and Flatau. [1] The bulk values of the dielectric constants for gold and silver reported by Johnson and Christy [3] were used, and the medium was assumed to have a refractive index of 1.33 corresponding to that of liquid water. Additionally, the surface field intensities around the particles were calculated using a modified version of the DDSCAT code provided by the Schatz group. [4, 2]

D.5 Singlet Oxygen Measurements

The relative rate of singlet oxygen generation (SOG) in solution was measured for each complex and for PpIX alone using a scavenger (9,10-Anthracenediyl- bis(methylene) dimalonic acid, ABDA). ABDA (1.5 mL, 0.2 mM) was combined with water (deionized, 1 mL) and an aliquot of each sample (1 mL) and then split into two cuvettes. One was placed in the dark to serve as the reference cuvette, and one was irradiated using a Xe arc lamp (1 W) fitted with a water filter to block infrared light (heat) and a long-pass filter (450 nm) to block ultraviolet light and prevent photobleaching of the ABDA itself. The absorbance of both the sample and reference cuvettes was collected periodically over 500 seconds, and the disappearance of the ABDA bands was monitored, plotted as a function of time, and fit with a curve. The relative rate constants of SOG were calculated from the slope of this decay curve.

D.6 Dynamic Light Scattering

DLS measurements were taken using a NanoZS Zetasizer particle analyzer (Malvern, 633 nm).

D.7 Cell Culture

Human oral squamous carcinoma cells (HSC-3), a malignant epithelial cell line, were cultured in Dulbecco's Modified Eagle's Medium (DMEM) (Mediatech) supplemented with 4.5 g/L glucose, sodium pyruvate, 10% v/v fetal bovine serum (FBS) (Mediatech) and 1% antimycotic solution (Mediatech). Cell cultures were kept at 37 °C in a 5% CO_2 humidified incubator.

D.8 Cell PDT Complex Treatment and Light Exposure

HSC-3 cells were grown in 96 well plates for 24 hours and then incubated with the respective NP-PpIX complexes in culture medium (DMEM) for 24 hours. Each nanoparticle concentration was kept constant at 0.1 nM, while PpIX concentrations were varied from 0.0 - 20.0 μM. Cells were then irradiated (10 mW, 30 min) with a Xe arc lamp fitted with a short-pass water filter (heat), a long-pass UV filter (350 nm), a 90° turning mirror, and a 30° light diffuser to ensure equal intensity for every well (Figure 94). Control cells were removed from the incubator along with the sample cells and placed in the dark. Nanoparticles and PpIX were removed and ca. 25% XTT reagent (Sigma) in culture medium (DMEM) was added. Cells were kept at 37 °C in a 5% CO_2 humidified incubator overnight. Absorbance measurements at 450 nm and 690 nm were taken on a Biotek Synergy H4 Multi-Mode Plate Reader.

D.9 Dark Field Imaging

Cells were cultured on 18 mm diameter glass coverslips for 24 hours and incubated with the respective NP-PpIX complexes diluted in culture medium (DMEM) for 24 hours. The nanoparticle and PpIX concentrations were kept constant at 0.1 nM and 0.2 μM, respectively. Particle solutions were removed and coverslips were then washed with DPBS buffer and fixed with 4% paraformaldehyde. Images were obtained with an inverted Olympus IX70 microscope with a dark field condenser (U-DCW).

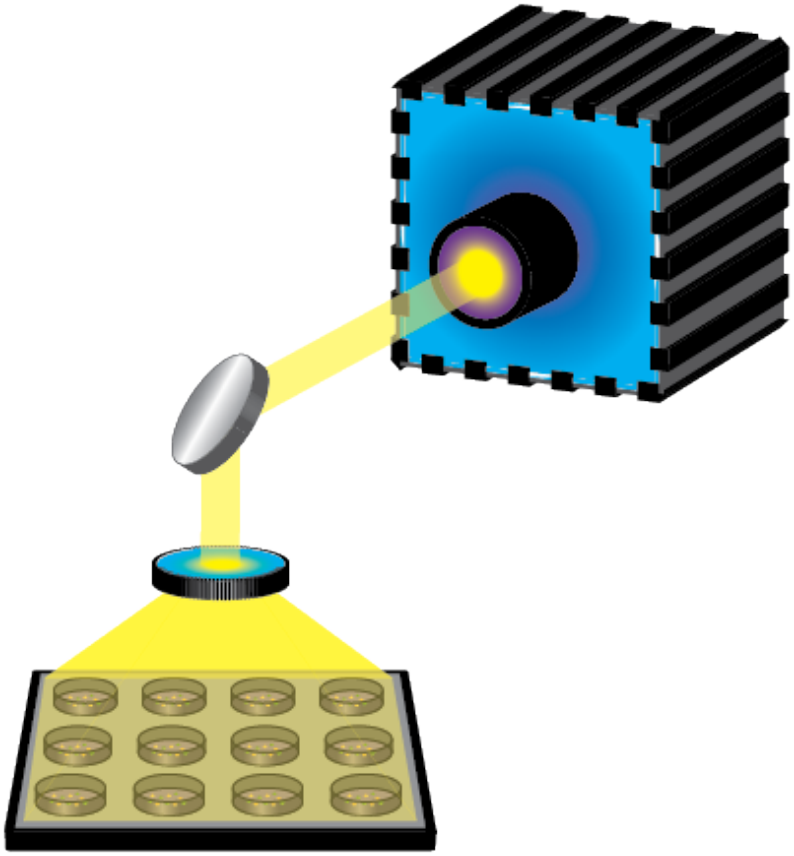

Figure 94: Schematic of exposure setup used to treat cells with light for photodynamic therapy.

A 100x/1.35 Iris objective (UPLANAPO) was utilized to collect the scattered light from the NP treated samples.

D.10 Data and Statistical Analysis

Nanoparticle histograms and average dimensions were obtained via measurement of at least 250 particles for each particle type using ImageJ software. Fluorescence, SOG, DLS, and cell viability data analysis was conducted using OriginLab 8.5. Results are reported as mean ± SD of three or more independent experiments. Cell viability data was analyzed using the t-test calculator (GraphPad Software, GraphPad Software, Inc.) and statistical significance was determined from PpIX treated cells to NP-PpIX complex treated cells unless otherwise noted. Data was considered statistically

D.11 REFERENCES

[1] FLATAU, P. J., STEPHENS, G. L., and DRAINE, B. T., "Light-scattering by rectangular solids in the discrete-dipole approximation - a new algorithm exploiting the block-toeplitz structure," *Journal of the Optical Society of America a-Optics Image Science and Vision*, vol. 7, no. 4, pp. 593–600, 1990.

[2] HAO, E., SCHATZ, G. C., and HUPP, J. T., "Synthesis and optical properties of anisotropic metal nanoparticles," *Journal of Fluorescence*, vol. 14, no. 4, pp. 331–341, 2004.

[3] JOHNSON, P. B. and CHRISTY, R. W., "Optical constants of noble metals," *Physical Review B*, vol. 6, no. 12, pp. 4370–4379, 1972.

[4] KELLY, K. L., LAZARIDES, A. A., and SCHATZ, G. C., "Computational electromagnetics of metal nanoparticles and their aggregates," *Computing in Science and Engineering*, vol. 3, no. 4, pp. 67–73, 2001.